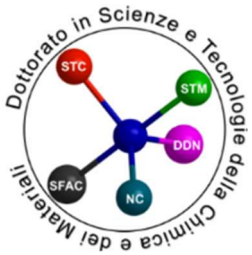

Università degli Studi di Genova

Doctorate in Science and Technology of Chemistry and Materials
XXXII Cycle

Ph.D. thesis in Materials Science

Development of iron based superconducting wires and tapes for high field applications

Supervisors:

Prof.ssa Marina Putti

Dott.ssa Valeria Braccini

Candidate:

Giulia Sylva

SUMMARY

EXTENDED ABSTRACT

Since the discovery of superconductivity by Heike Kamerling Onnes in 1911[a], one of the first envisaged applications for superconductors was the generation of magnetic fields. The possibility became a reality only after 1935, when type II superconductors were discovered. In the last few years, with the advent of large scientific projects for High Energy Physics (HEP) such as the Large Hadron Collider (LHC) at CERN and the ITER Project for nuclear fusion, international R&D efforts were launched on key enabling technologies through dedicated collaborative programmes, e.g. on high-field magnets and advanced cryogenics. Besides the scientific challenge, pushing the limits of superconducting materials and high-field magnet technologies will lead to affordable, industrial-scale products with benefits and opportunities that go beyond particle accelerators and nuclear fusion research. Superconducting conductors for large scale application must fulfil several precise requirements. They are round wires or tapes composed of thin superconducting filaments embedded in a metal matrix which provides protection against magnetic flux jump and thermal quench. They must have enough mechanical strength to resist conductor fabrication, coil winding, cabling, thermal stresses when they are cooled down to cryogenic temperature and electromagnetic stresses when they are under operation. Moreover, they must be capable of carrying a very high operating current (hundreds or thousands of amperes). In terms of engineering critical current density J_e (i.e. the critical current over the total cross section of the conductors which comprises the superconductor but also the metallic matrix, any possible barriers, stabilizer, buffer layers and all elements which compose the section of the conductors), the conductors must reach 10^4-10^5 A/cm^2 in applied magnetic fields ranging from 1 to 25 T. As can be seen from Fig. A many superconducting phases were discovered so far, but for about 40 years the only superconducting materials able to fulfil the requirements to be employed in the construction of magnets have been the Nb-based materials and in particular NbTi and Nb_3Sn.

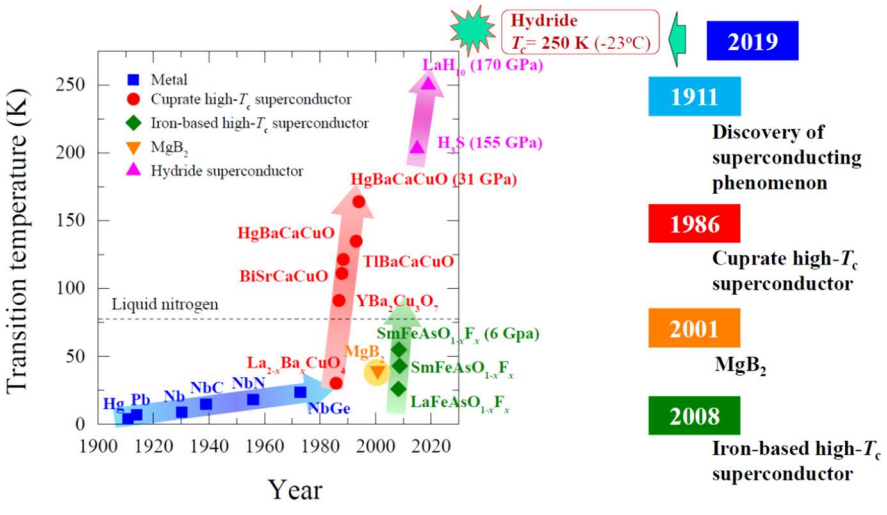

Fig. A: Critical temperature vs year of discovery of different superconductors families[b].

[a] Onnes H.K., The resistance of pure Mercury at Helium temperatures *Comm. Phys. Lab.* 12, (1911)
[b] Ma Y., Recent Progress of iron-based wire development for high field applications *presented at EUCAS 2019 Glasgow* (2019)

The Iron Based Superconductors (IBS) were discovered ten years ago by the group of Professor Hosono[c]. They have immediately shown a great potential for application in high magnetic field. They exhibit relatively high critical temperature T_c, and huge upper critical fields H_{c2}: these properties make them the perfect candidates for the generation of high magnetic fields. Among all the IBS families, the iron chalcogenides $FeSe_xTe_{1-x}$ family (also called 11 phase or FST in the following) has the simplest stoichiometry, and it is quite attractive because of its relatively ease of fabrication and the absence of toxic arsenic. FST thin films have been successfully grown on single crystalline substrates[d,e] and on technical metallic templates commercially available for the deposition of $REBa_2Cu_3O_{7-x}$ (REBCO, with RE = rare earth) using the technique developed for Coated Conductors (CC) of YBCO , which is based on the deposition of epitaxial superconducting thin films on biaxially textured metallic substrates. Nevertheless, these substrates present a relatively complex architecture, as can be seen in Fig. B, which causes a strong increment of the cost of production of the tapes. For these reasons, the route to the realization of long conductors of the 11 phase is still long, and requires the development of specific metallic substrates, to make this phase appealing for applications.

Another important aspect, that needs to be considered in view of high-field applications, beside the fabrication of a suitable cost-effective conductor, is the effect of irradiation. The introduction of defects by means of irradiation techniques offers the unique possibility to investigate changes to superconducting properties caused by additional defects; irradiation experiments also benchmark the achievable critical currents in a superconducting compound and indicate the necessity of improving pinning to enhance their application potential. Furthermore, irradiation experiments are also carried out to test the suitability of a conductor for operation in a harsh environment, such as fusion reactors or accelerators.

In this context my thesis is focused on the study of FST thin films, namely the development of FST CC and the proton irradiation of FST thin films deposited on CaF_2 single crystals. These two activities are strongly connected both because they are based on the fabrication of FST thin films with the Pulsed Laser Deposition (PLD) on different substrates, and because they have the common aim to study the possibility of use IBS conductors in a high field and harsh environment. The thesis is divided in two main sections:

1) Coated Conductors development: The first section describes the development of FST CC employing in-house manufactured metallic substrates and substrates produced at ENEA research centre of Frascati. This activity has been also carried out as a part of the collaboration between CERN and CNR SPIN Genova (ADDENDUM FCC-GOV-CC-0086 to the Memorandum of Understanding for the FCC Study), which has the aim to develop superconducting materials alternative to Nb_3Sn for high field applications within the FCC (Future Circular Collider) study. In the part of the project devoted to IBS, the main objective is to study the possibility of developing a conductor in the form of tape or wire in a scalable and cost-effective way.

[c] Kamihara Y. *et al* Iron-Based Layered Superconductor $La[O_{1-x}F_x]FeAs$ (x = 0.05−0.12) with T_c = 26 K, *J. Am. Chem. Soc.* **130** (2008)

[d] Bellingeri E. *et al* T_c=21K in epitaxial $FeSe_{0.5}Te_{0.5}$ thin films with biaxial compressive strain *Appl. Phys. Lett*. **96**,102512 (2010)

[e] Si W. *et al* High current superconductivity in $FeSe_{0.5}Te_{0.5}$ coated conductors at 30 tesla *Nat. Comm* **4**, (2013)

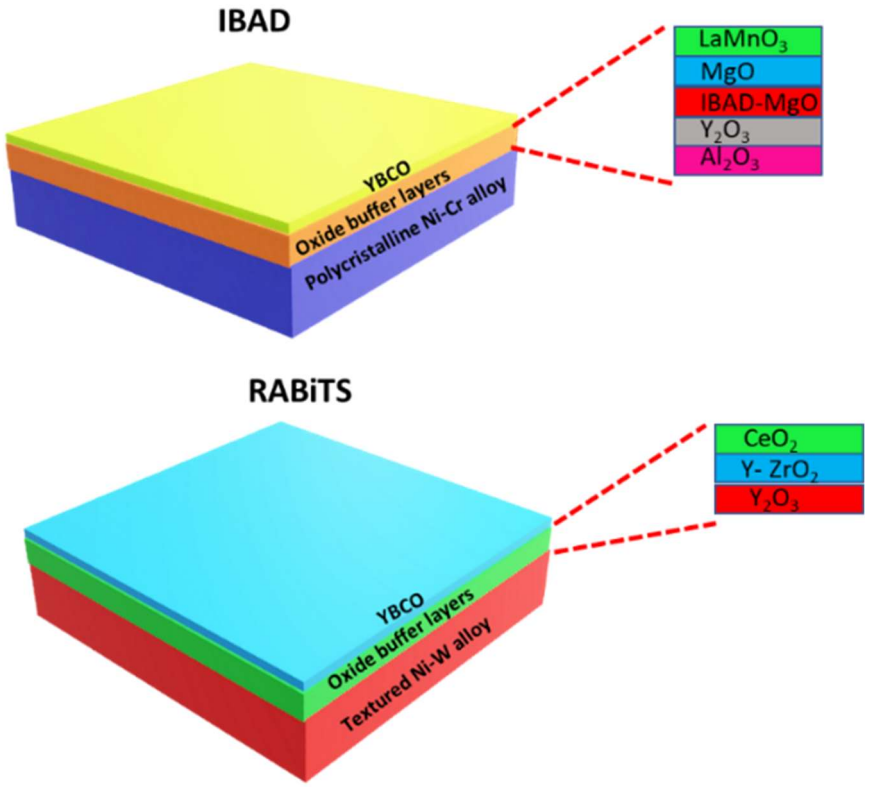

Fig. B: Two different types of commercially available substrates for CC: the Ion-Beam Assisted Deposition (IBAD) substrates, where an appropriate oxide is grown on a polycrystalline and randomly oriented metallic tape, and the Rolling Assisted Biaxially Textured Substrates (RABiTS), where the biaxially orientation is provided by the metallic tape.

2) Proton irradiation on FST thin films: The second part describes the proton irradiation experiment on FST thin films deposited on CaF_2. This activity was conducted within a collaboration between Politecnico di Torino and CNR SPIN. In order to clarify what are the effects of irradiation on the superconducting properties of the films and the role played by the substrates in this context, the effects of 3.5 MeV and of 0.5 MeV protons with different irradiation fluences and different proton implantation depths were investigated.

Regarding the aforementioned activities I was personally involved in the following experimental tasks: preparation of thin films on different substrates using PLD, development of technological substrates through mechanical deformation and heat treatments, standard photolithography for the patterning of the films, transport measurements in magnetic fields up to 9T and X-ray diffraction (XRD) characterization.

1) COATED CONDUCTORS DEVELOPMENT

The idea is to develop a simple template, in order to make IBS appealing competitors of REBCO CC. An essential requirement for large scale applications is the capability to carry current over a long length,

in other terms current needs to flow along polycrystalline materials through Grain Boundaries (GB). In IBS, as in the cuprates High Temperature Superconductors (HTS), the J_c strongly depends on the misorientation angle of grain boundaries (ϑ_{GB}). For this reason, the CC technology established for HTS, which provides a biaxial alignment of grains, is a promising route for improving the performance of IBS. Fortunately, the critical misorientation angle at which J_c starts to decrease exponentially is around 9° for IBS, much larger than the ~3° reported for YBCO. This is a great advantage for the fabrication of CC since requirements on the in-plane alignment of buffer layers are less demanding. Moreover, the deposition of 11 is done in Ultra High Vacuum (UHV) and not in oxygen atmosphere as in the case of REBCO, so the oxidation of substrate is avoided. In this context, my PhD thesis is moving forward trying to simplify the technical substrate, reducing the degree of orientation or removing buffer layers in order to make these CC easy to produce, cost-effective and consequently appealing for large scale applications. I have worked on the development of 11 CC with simpler and cost-effective RABiTS. The simplicity of the substrates could derive from both from the employment of commercial metallic alloy instead of the custom-made NiW5% but also from the modification of the architecture of the buffer layers. The buffer layers can also be deposited with simple and scalable method, be reduced in number or even completely removed. These possibilities singularly or combined contribute to the simplification and consequently to the cost reduction of 11 CC (see Fig. C).

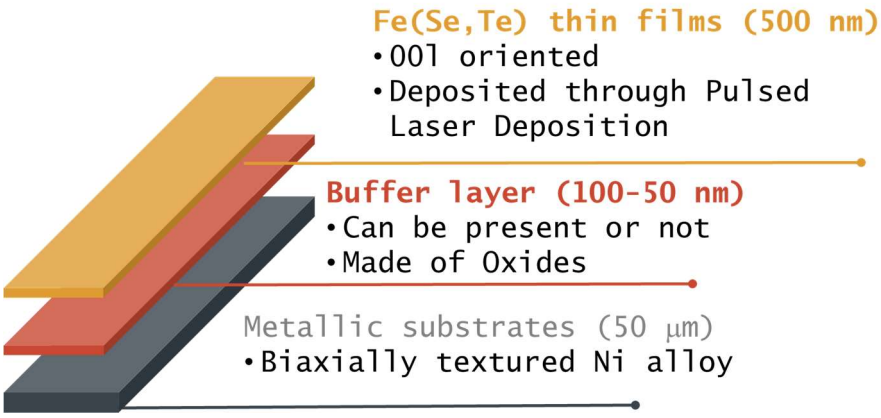

Fig. C: Proposed architecture for 11 CC

In the section of CC development the different CC architectures studied are presented, starting from the development of simpler metallic substrates made of a commercial alloy and without any buffer layers to more complicated substrates based on NiW5% metallic tapes with different nitrides and oxides buffer layers, together with a study of the properties of the FST thin films deposited on such different templates. The work started from the long-lasting experience of the research group of CNR Spin Genoa on the deposition of 11 thin films by PLD. However, the evolution from thin films on single crystals to thin films on metallic templates is not trivial and requires preliminary studies to prove the possibility to obtain high quality thin films even if the substrate is not optimal as is a single crystal. In particular, problems related to film thickness, thermal expansion of the substrate and crystalline match

between substrate and film were addressed starting from the optimization of the process on single crystal and then transferring the process to the templates. We proved the possibility to deposit 11 thin films with a thickness up to 500 nm, at low temperature (from 300°C down to 200°C). We were also able to improve the texturing of the films deposited at low temperature using a not-superconducting seed layer of the 11 phase following the idea presented in the paper[f]. These preliminary studies were used to obtain high quality 11 thin films on different substrates architecture. The substrates used during the thesis can be divided in two categories: the in-house manufactured substrates and the RABiTS prepared at ENEA.

In-house manufactured substrates:

Invar substrates: In this section the feasibility of producing 11 CC using a cost-effective Invar 36 substrate without any buffer layer is described. We obtained a metallic biaxially textured substrate with an in-plane and out-of-plane orientation suitable for the deposition of 11 thin films. The in-plane and out-of-plane orientation of the film can be improved using a non-superconducting 11 seed layer, reaching a misorientation angle (both in plane and out of plane) significantly lower than 9°, the critical angle at which J_c starts to decrease exponentially in 11 phase. Despite the good orientation of the films, they do not show a superconducting transition. Scanning Transmission Electron Microscope (STEM) analysis performed on a cross-sectional lamella prepared by Focus Ion Beam (FIB) revealed local oxidation of the substrate at the interface with the film and significant Nickel (Ni) diffusion from the substrate to the film. This Ni poisoning is most likely the cause of the suppression of superconductivity[g]. The discovery of the interdiffusion of Ni from the substrate inside the film made necessary the study of the feasibility of a chemical barrier with a suitable thickness. We started exploiting not-oxides materials as metals and nitrates which can be deposited in the same chamber of the FST films in UHV. We demonstrated the possibility to grow an epitaxial buffer layer of Fe, and we also demonstrate that AlN buffer layer 80 nm thick can act as a chemical barrier to block Ni diffusion. However, the insulation from Ni diffusion is not complete since the FST thin films do not show a complete superconducting transition.

Hastelloy substrates: In this section the possibility to obtain 11 CC employing the native passivation layer of Hastelloy as a chemical barrier against Ni diffusion is described. This substrate is based on a different concept: it does not need the deposition of a buffer layer but exploits instead the native chromium oxide passivating layer incremented in thickness with a thermal heat treatment in oxygen. Fig. E shows the different thickness of oxide layer in the not oxidised and in the oxidised Hastelloy substrate. The 11 thin films deposited on oxidised Hastelloy substrates shows a good J_c and a very steep H_{c2}. Despite the good superconducting properties, the film does not have an in-plane crystalline orientation since the oxide on the substrate is randomly oriented.

[f] Molatta S. *et al* Interface control by homoepitaxial growth in pulsed laser deposition iron chalcogenide thin films *Sci. Rep.* **5**, (2015)

[g] Sylva G. *et al* Analysis of Fe(Se,Te) films deposited on unbuffered Invar 36 *IEEE Trans. Appl. Supercond*. **29**, 1-5 (2019)

ENEA substrates:

This section describes the activity made in collaboration with ENEA regarding the development of 11 CC on NiW5% substrates from EVICO with different oxides buffer layers deposited at ENEA's laboratory. These substrates were developed for REBCO, but they could be successfully employed for FST CC.

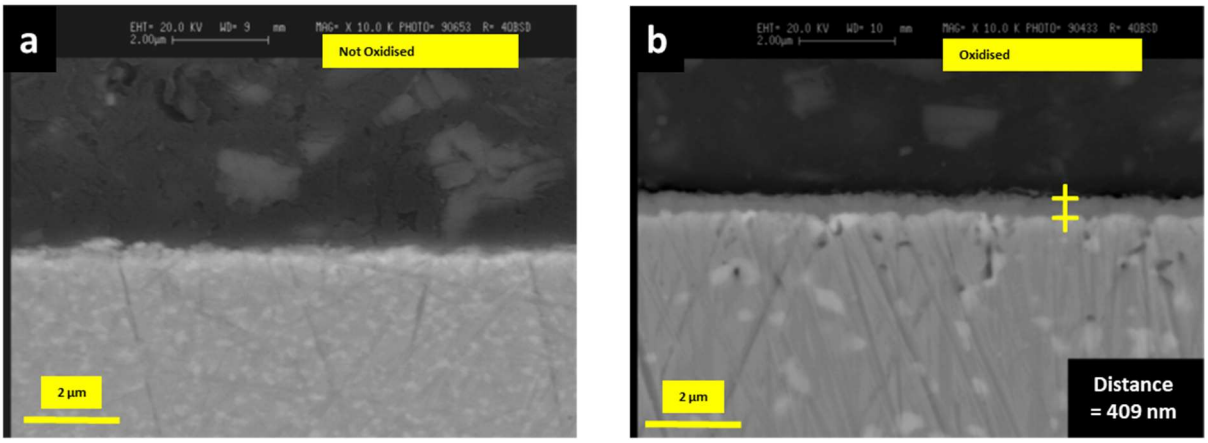

Fig. E: Cross section of Hastelloy substrate, performed with Scanning Electron Microscope (SEM), before (a) and after (b) oxidation process. The oxidised substrate shows an oxide layer of about 400 nm.

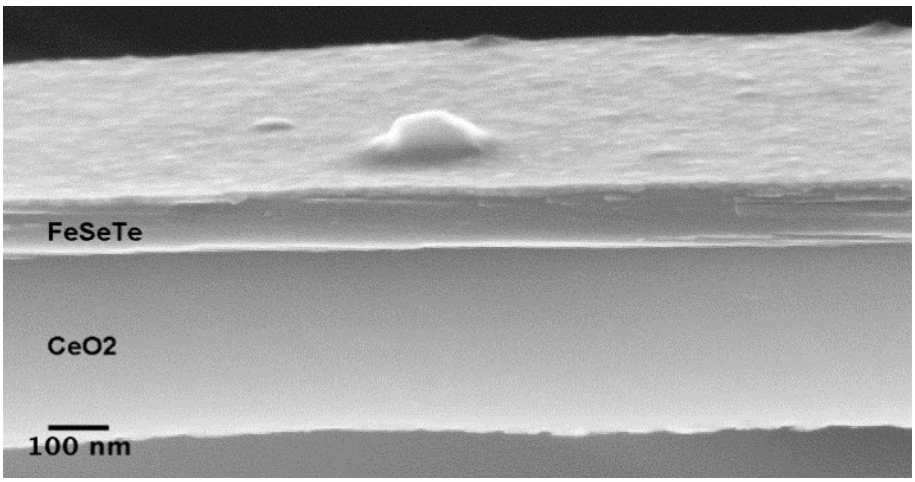

Fig. D:Cross section of the Fe(Se,Te) thin film deposited on NiW5% substrate with a buffer layer of CeO_2.

NiW5% with CeO_2 buffer layer: Starting from commercially available Ni – 5 at.% W tapes which show an out-of-plane orientation of about 7° and in-plane orientation around 5°, RABiTS templates were realized at ENEA for CC fabrication depositing CeO_2 thin films on the metallic tape. The oxide buffer layers, deposited via PLD, exhibit an out-of-plane and an in-plane orientation suitable for FST deposition and act as a chemical barrier against Ni diffusion. FST thin films deposited on such a simple template show a superconducting transition at 16 K, very high upper critical field values with a $\Delta T_{c,0}$ of only 3 K in 18 T. The transport critical current density reaches a value of 1.7×10^5 A/cm ^{2} at 4.2 K in

self field and is reduced of less than one order of magnitude up to 18 T, remaining isotropic with respect to the magnetic field direction[h]. Fig. D shows a cross section of the 11 CC, the first ever realized with one buffer layer.

Chemically grown buffer layers: It is possible to further simplify the production of CC using other methods to deposit the buffer layer. Chemical methods like Chemical Solution Deposition (CSD) and Metal Organic Deposition (MOD) are more scalable and cost effective than the pulsed laser deposition. In order to start a more systematic study about this kind of buffer layers, we started to work on CZO (CeO_2 doped Zr) and on LZO($La_2Zr_2O_7$), buffer layers deposited respectively on YSZ (Yttria-stabilized Zirconia) an on Strontium Titanate (STO) single crystal substrates and then the activity moved on using the same buffer layers but deposited on Ni-W. The best results were obtained using NiW 5% substrate with a buffer layer of about 50 nm of CZO, deposited by CSD, and with a buffer layer of LZO 50 nm thick deposited by MOD. The possibility to obtain epitaxial thin films both on Ni-W with CZO buffer layer and on Ni-W with LZO buffer layer was demonstrated. However, these films do not show a complete superconducting transition.

2) PROTON IRRADIATION OF 11 THIN FILMS

In view of future large-scale applications of IBS conductors in high magnetic fields, the study of the effects of irradiation on the superconducting properties of the materials becomes essential to eventually be able to evaluate the possible employment in harsh environments such as fusion reactors or particles accelerators. To study the effects of irradiation on a CC is, at first is necessary to start from thin film deposited on single crystals substrates. And even if many studies on the effects of irradiation on IBS single crystal have already been published, just a few numbers of experiment on irradiated thin film on single crystal substrates are reported in literature. The effects of 3.5 MeV proton and of 0.5 MeV proton irradiation on FST thin films grown on CaF_2 was explored. In particular, an experimental investigation with different irradiation fluences up to $7.30 \cdot 10^{16}$ cm^{-2} and different proton implantation depths was carried out, in order to clarify whether and to what extent the critical current is enhanced or suppressed, what are the effects of irradiation on the critical temperature, on the resistivity and on the critical magnetic fields, and finally what is the role played by the substrate in this context.

3.5 MeV proton irradiation: Fluence was varied in a wide range from 0.70×10^{16} to 7.30×10^{16} cm^{-2}. Moreover, in order to understand the role of the defected substrate where the protons implant in further modifying the film properties, we irradiated some samples with lower proton energies at comparable displacement per atom (*dpa*) values by the interposition of a thin Al foil of a suitable thickness. This allows us to control the implantation depth of protons into the substrate, and to check whether the film properties change in a different way when the substrate is mainly damaged close to or far from the substrate–film interface. Fig. F shows the proton distribution inside the sample, without and with aluminium foil. It turns out that when protons are implanted deep inside the substrate, J_c enhancements in FST can be obtained, even if they are not as large as in the case of other IBS. In such conditions, critical temperature, and critical fields are virtually unchanged for the employed fluences.

[h] Sylva G. *et al* Fe(Se,Te) Coated conductors deposited on simple rolling-assisted biaxially textured substrates templates *Supercond. Sci. and Technol*. **32**, 084006 (2019)

Conversely, when the implantation layer is close to the substrate–film interface, both T_c and J_c show a decrease together with an enhancement of resistivity, thus pointing to the crucial role of the substrate itself and its possible modifications in determining superconducting film properties.

This is confirmed with a structural analysis performed by XRD, which highlights the different effects of protons at different implantation depth. This should be carefully considered in every irradiation experiment on thin-film superconductors. Finally, what emerges from our irradiation experiment with MeV-energy protons up to very high values of *dpa* is that the family 11 is very robust against proton irradiation with respect to other superconductors, e.g. cuprates[i]. Moreover, it has been shown that the naturally weak anisotropy of the samples is just slightly altered by the exposure to such radiation[j,k].

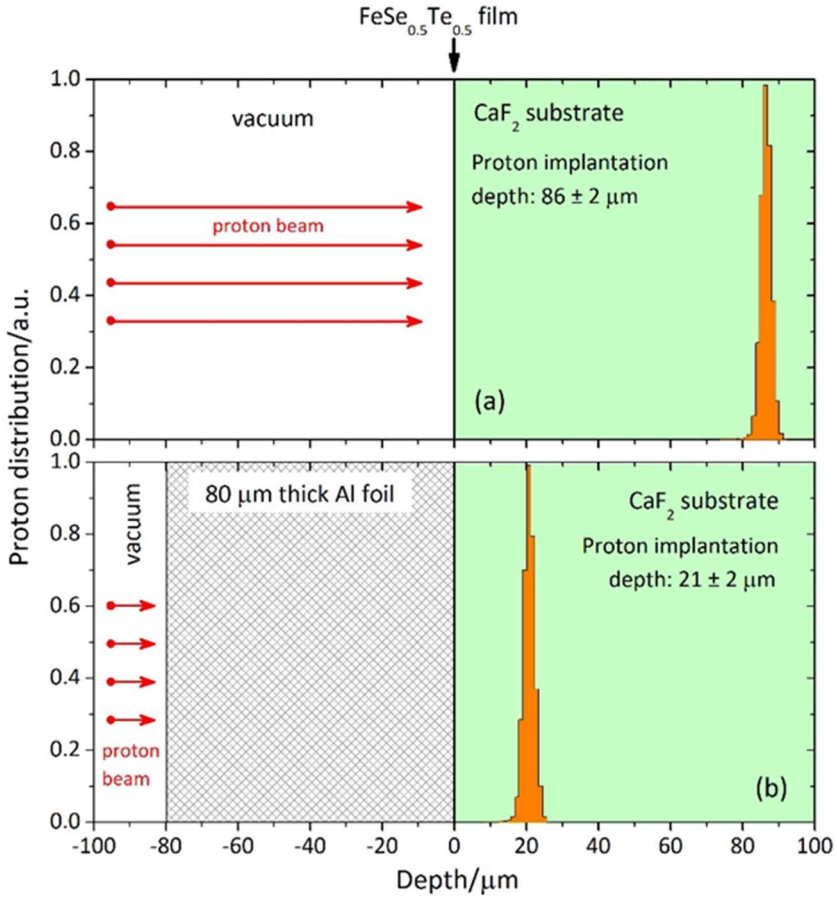

Fig. F: Spatial distribution of the implanted protons (orange histograms) in the CaF_2 substrate (green region) without (a) and with (b) the interposition of a 80µm-thick Al foil (gray crosshatch region), used to decelerate the protons. The zero depth corresponds to the sample surface. The sample consists of a 100 nm thick $FeSe_{0.5}Te_{0.5}$ film (not visible) and its CaF_2 substrate. The interposition of the Al foil results in a shift of the implantation peak closer to the film-substrate interface.

[i] Sylva G. *et al* Effects of high energy proton irradiation on the superconducting properties of Fe(Se,Te) thin films. *Supercond. Sci. and Technol*. **31**, 054001 (2018).
[j] Leo A. *et al* Critical current anisotropy in Fe(Se,Te) film irradiated by high energy protons *To be published* (2019)
[k] Leo A. *et al* Anisotropic Effect of Proton Irradiation on pinning properties of Fe(Se,Te) thin films *IEEE Trans. Appl. Supercond.* **29**, 1-5 (2019)

0.5 MeV proton irradiation: In order to further investigate the role of the implantation depth of the defects we conducted an experiment of irradiation reducing the energy of the protons source. The further reduced energy of the protons allows an implantation of the defects closer to the interface between film and substrates, varying from the previous 86 µm for direct irradiation with 3.5 MeV protons, and the 21 µm obtained protecting the sample with an aluminium foil during the irradiation with 3.5 MeV, to a depth which is one order of magnitude lower with 0.5 MeV protons (Fig. G). The Fluences varies from 0.12×10^{16} to 5.11×10^{16} cm^{-2}.

The fluences were calculated in order to obtain the same *dpa* previously explored with high energy protons. We observed a J_c that for low *dpa* decreases at low magnetic field but remains stable or even shows a slight increase with increasing field, and this effect is more remarkable for high fluence and high temperature. For high *dpa* the increase of J_c with the magnetic field is strongly evident: an increment of J_c of about 60% is reported at 8K and 5T. The growth of J_c with the magnetic field is an effect that was never be observed in irradiation with 3.5 MeV. The increment of J_c can only be ascribed to the presence of pinning centres inside the film which are generated by irradiation. Sub-MeV proton irradiation, probably, causes inside the film the formation of a pinning landscape of defects which is not present in the samples irradiated with 3.5 MeV. The irradiation with Sub-MeV protons confirms the important role of the substrate. This must be considered during the CC development, since the different architectures of the substrates influence the behaviour of the 11 phase exposed to irradiation.

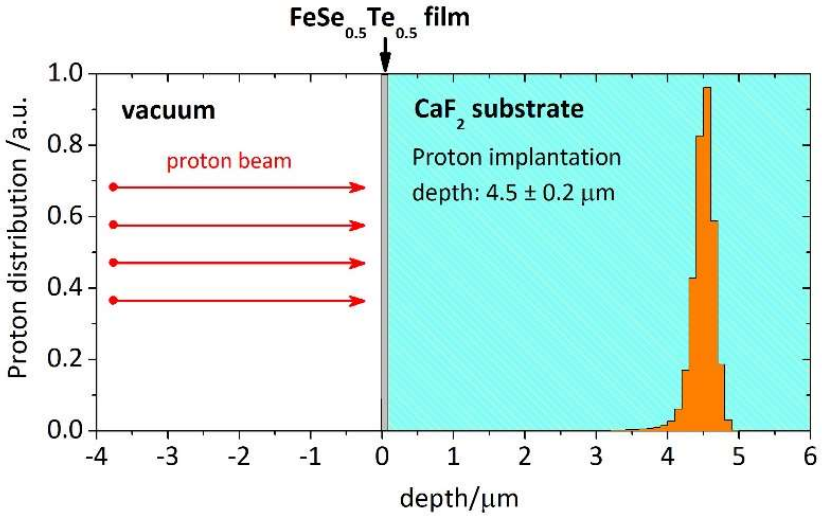

Fig. G: SRIM (Stopping and Range of Ions in Matter) simulation of the effects of 0.5 MeV proton on the sample. The grey band correspond to Fe(Se,Te) thin film while the light blue region correspond to the substrate. The implantation depth is further reduced to 4.5 µm

.

1 INTRODUCTION

During the last years the will of scientists and nations to overcome some important barriers in science and technology resulted in some challenging projects as high energy particle accelerators for the study of particle physics and systems for nuclear fusion. In this context High-Field Magnets and consequently superconducting materials became a key technology for these frontier projects. These ambitious projects are based to date on the Nb-based low temperature superconductors. NbTi and Nb_3Sn, discovered in 60s and commercialized since 80s , are now produced on large scale thanks to their ability to be fabricated in round multifilamentary wire with high filling factor and relatively high critical current density (J_c). However, Nb-based superconductors are now approaching their limits of applications, and recently arose the necessity to overcome their performance in terms of magnetic field and temperature of applications[1].

The Iron Based Superconductors (IBS) discovered ten years ago by the group of Professor Hosono[2], have shown immediately a great potential for application in high magnetic fields. They exhibit relatively high critical temperature T_c, and huge upper critical fields H_{c2}: these properties make them the perfect candidates for the generation of high magnetic fields. Among all the IBS families the iron chalcogenides $FeSe_xTe_{1-x}$ (11 phase or FST in the following) has a simple stoichiometry, and it is quite attractive because of its relatively ease of fabrication and the absence of toxic arsenic. During the past few years IBS wires were successfully produced with the Powder in Tube (PIT) method reaching the practical value for applications of J_c: 10^5 A/cm^2. However, biaxially textured thin films deposited on single crystal show superior J_c performance. Unfortunately, films on single crystal substrates cannot be used for large scale applications. Thanks to the Coated Conductors (CC) technique, developed in the '80s and the '90s for $REBa_2Cu_3O_{7-x}$ (REBCO, with RE =rare earth), is it possible to produce long superconducting tapes, exploiting the deposition of superconducting thin films on specific biaxially textured substrates, reproducing the performances obtained on single crystal substrates. FST thin films have been successfully grown on single crystalline substrates [3,4] and on technical metallic templates commercially available for the deposition of REBCO. These substrates present a quite complex architecture causing a strong increment of the cost of production of the tapes [5]. For these reasons, the route to the realization of long conductors of the 11 phase is still long, and requires the development of specific metallic substrates, to make this superconducting phase appealing for applications. In IBS the exponential decay of J_c across misoriented grain boundaries is less severe than for REBCO, in particular for FST thin films grown on bi-crystals a misorientation angle $\theta_c > 9°$ has been reported [6,7], significantly higher than $\theta_c < 4°$ observed in REBCO[8]. Moreover, FST thin films are deposited without the presence of oxygen in a temperature range between 230°C and 550°C [3], much below the deposition temperature required for REBCO. These features have a strong impact on the development of a suitable technology to produce conductors relaxing significantly the film texture constraint and the role of the buffer layer architecture typical of the substrates developed for REBCO. Hence, it is possible to think about the development of much simpler metallic templates, reducing essentially the complexity and the manufacturing cost of IBS-CC, which may make them more attractive on the cost-performance basis.

Another important aspect, beside the fabrication of a suitable cost-effective conductor that needs to be considered in view of high-field applications, is the robustness of the material in harsh environments such as those present in particle accelerators or nuclear fusion reactors where different irradiation sources are present (proton, neutron, pions, electron and photon).

In this context my thesis is focused on the possibility to develop a suitable FST CC for high field applications comprising both the study of a cost-effective method to produce the CC and the study of the effects of proton irradiation on the FST phase. The thesis is inserted in a collaboration between CNR Spin and CERN (ADDENDUM FCC-GOV-CC-0086 to the Memorandum of Understanding for the FCC Study), which is part of the Conductor Development Program of CERN. The program aims to develop wires meeting the requirements of the superconducting magnets for the Future Circolar Collider (FCC), with proven scalability to long-length industrial production, and with the potential for cost reduction. The program is centred on Nb_3Sn wires, but it also supports smaller activities seeking a breakthrough in the high-field performance or cost effectiveness of alternative superconducting materials: currently include studies of MgB_2, $Bi_2Sr_2CaCu_2O_{8+\delta}$ and IBS.

The thesis is divided three chapters:

- **Chapter 1 - IRON BASED SUPERCONDUCTORS FOR HIGH FIELD APPLICATIONS:** In this chapter the potentiality of IBS for the application at high magnetic field is presented. The description starts from a brief review of all the possible superconducting materials candidates for application in high magnetic field and moving forward describing IBS features and the results obtained in the production of IBS conductors with the CC technique.
- **Chapter 2 - DEVELOPMENT OF 11 COATED CONDUCTORS FOR HIGH FIELD APPLICATIONS:** The second chapter is devoted to the description of the results obtained with my experimental work in the development of FST CC. The presented work is divided in three main parts:
    - **A.** This section describes the preliminary studies performed on FST thin films deposited through Pulsed Laser Deposition (PLD) on single crystal substrates which are necessary to obtain high quality FST thin films on metallic substrates.
    - **B.** The second section describe the development of 11 CC with in-house manufactured metallic substrates. We started from the development of a suitable biaxially textured metallic tapes, on which we deposited 11 thin films without buffer layers and with different buffer layers.
    - **C.** The last section describes the deposition of 11 thin films on metallic substrates developed at ENEA research centre in Frascati (Rome). These substrates were developed for REBCO and are composed of a NiW tape from the supplier company EVICO and one oxide buffer layer.
- **Chapter 3 - EFFECTS OF IRRADIATION ON 11 THIN FILMS:** The last chapter of the thesis describes the study of the effects of proton irradiation on FST thin films deposited on CaF_2 single crystal substrates. The study started just a few years ago and due to the complexity of the study the work started from thin films deposited on single crystals which are the superconducting thin films with the best performance, and which are quite reproducible. This activity is performed in collaboration with Politecnico di Torino.

The thesis also comprises an Appendix which regard the development of (Ba,K)Fe_2As_2 (Ba-122 in the following) wires with the ex-situ PIT method. This activity, as the one on CC, is focused on the possibility to produce suitable wires for high field applications, using a simple and scalable method. I was involved in the development of the Ba-122 PIT wires during the last part of my thesis, and just many attempts were done. The results are reported for completeness to highlight the possibility to develop cost-effective and simple IBS conductor with different techniques.

2 IRON BASED SUPERCONDUCTORS FOR HIGH FIELD APPLICATIONS

2.1 SUPERCONDUCTING MATERIALS FOR APPLICATION AT HIGH FIELD

Since the discovery of superconductivity by Heike Kamerling Onnes in 1911 [9], one of the first envisaged application was the generation of magnetic fields. The possibility became a reality only after 1935, when type II superconductors were discovered. The first Nb-based magnet was built in 1954, but the first large scale magnets for fusion and particle acceleration was developed in 1970. From this first attempt a lot of efforts were done to obtain increasingly better performing superconducting magnets both for scientific and medical applications. A significant growth of the superconducting wires production, after all, was strictly in the 80s with the development of the Magnetic Resonance Imaging (MRI) and the Nuclear Magnetic Resonance (NMR). In last years with the advent of large scientific projects for High Energy Physics (HEP) as the Large Hadron Collider (LHC) at CERN and the ITER Project for nuclear fusion which is under construction, was launched international R&D efforts on key enabling technologies through dedicated collaborative programmes, e.g. on high-field magnets and advanced cryogenics. Besides the scientific challenge, pushing the limits of superconducting materials and high-field magnet technologies will lead to affordable, industrial-scale products with benefits and opportunities that go beyond particle accelerator and nuclear fusion research. These studies can be useful to develop compact, cryogen-free, MRI, High field magnets for NMR analysis of organic and inorganic matter and more compact particle-beam cancer therapy accelerators.

Superconducting conductors for large scale application must fulfil several requirements. They are round, or tape shaped wires composed of superconducting filaments embedded on a metal matrix which provide protection against magnetic flux jump and thermal quench. They must have sufficient mechanical strength to resist conductor fabrication, coil winding, cabling, thermal stresses when they are cooled down to cryogenic temperature and electromagnetic stresses when they are under operation. Moreover, they must be capable of carrying high operating current of hundreds or thousands of amperes. In terms of engineering critical current density J_e (ratio of the critical current I_c to the total cross section of the conductors which comprises superconductor but also metallic matrix, any possible barriers, stabilizer, buffer layers and all elements which composed the section of the conductors) the conductors must reach 10^4-10^5 A/cm^2 in applied magnetic fields ranging from 1 to 25 T. As can be seen from Figure 1 many superconducting phase were discovered so far, but for about 40 years the only superconducting materials able to fulfil the requirements to be employed in the construction of magnets were the Nb-based materials and in particular NbTi and Nb_3Sn. The NbTi, discovered in early 60s, is a metallic alloy, which became superconductor under 9 K in the cubic β-phase. When the NbTi is cold mechanical worked, it develops a Ti secondary phase, called α- phase which precipitates at the grain boundaries, acting as natural pinning centre. The fraction of Titanium in superconducting wires is around 45-50% which corresponds to a maximum of upper critical field (H_{c2}) of about 14.5 T and a critical temperature (T_c) around 9 K. Since NbTi is a metallic alloy and its properties are strongly linked to the composition of the alloy and not significant affected by the process of production. Moreover, it shows good mechanical properties and it is applicable in a range of magnetic field between 2-10 T at 4.2 K. Nowadays about 2000 tons of NbTi are produced and mostly employed for MRI and in the LHC project.

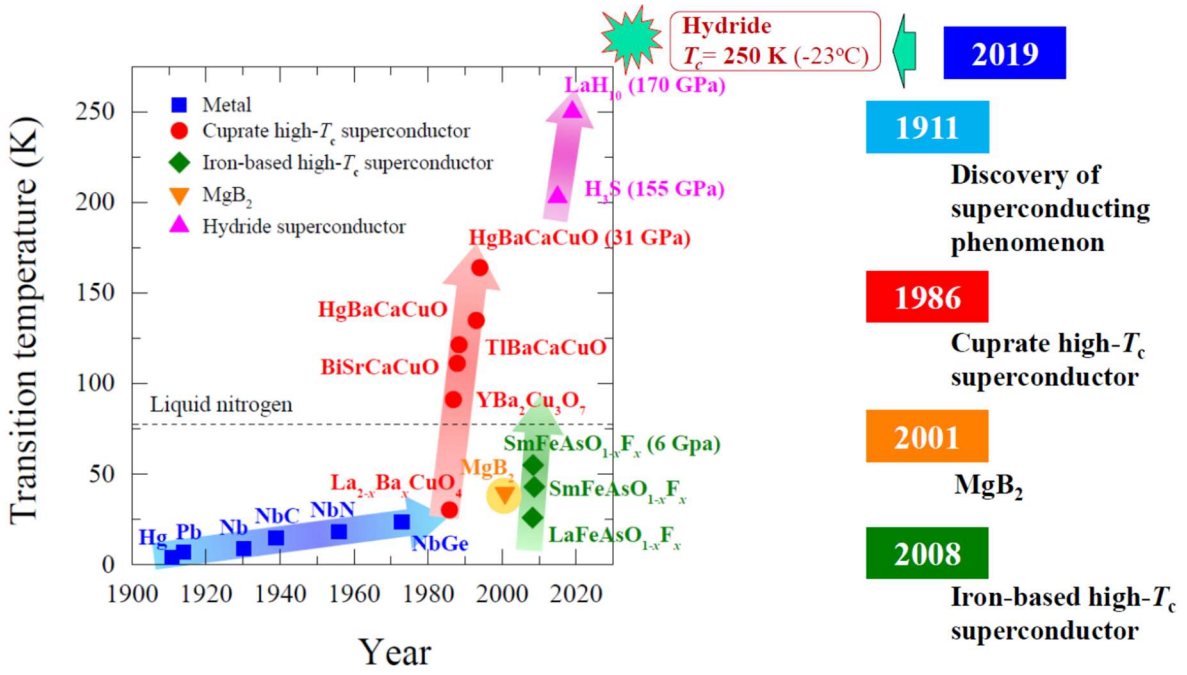

Figure 1: Critical temperature vs year of discovery of all superconductor's families[10].

The intermetallic compound Nb_3Sn, discovered in 50s, belongs to the A15 compound which is characterized by a structure A_3B. It shows a T_c around 18 K and a H_{c2} around 28 T with an atomic percentage of Sn around 23%. Because of its brittleness, Nb_3Sn did not have the same rapid development of NbTi but during the lasts year lots of efforts were done to optimize Nb_3Sn conductors for applications in high magnetic field. During 90s ITER was the primary customer of Nb_3Sn, ordering more than 20 tons of wire from companies all over the world. This program helped to establish a large-scale production of this materials.

Nowadays, the Nb-based superconductors are the most used conductors for the development of magnets both for medical and scientific purpose. However, recently emerges the necessity to overcome the limits of applications of Nb-based superconductors[1]. ITER projects is based on the possibility to develop suitable conductors for high field magnets using Low Temperature Superconductors (LST) as Nb_3Sn and NbTi which are at the moment the only superconducting materials that can be produced on a large scale and that can reach high magnetic field. In the case of ITER, Nb_3Sn magnets are enough to reach the required magnetic field to confine and control the plasma. The situation is strongly different for the new CERN Project for the Future Circular collider (FCC) whose purpose and long-term goal are to design a hadron collider (FCC-hh) with an energy of about 100 TeV in a new 80–100 km tunnel (see Figure 2). The energy (E) reach by a high-energy hadron collider is simply proportional to the dipole magnetic field (B) and to the bending radius (ρ): $E \propto B \times \rho$. Assuming a dipole field of 16 T, expected to be achievable with Nb_3Sn technology, the ring circumference must be about 100 km in order to reach the target value 100 TeV which is the required energy. This means that the higher is the magnetic field, the smaller can be the circumference of the tunnel and the simpler could be the construction of the accelerator. For these reasons the CERN launched the Conductor

Development Program which aims to develop wires meeting the requirements of the superconducting magnets for the FCC, with proven scalability to long-length industrial production, and with the potential for cost reduction. The program is centred on Nb_3Sn wires, but it also supports activities seeking a breakthrough in the high-field performance or cost effectiveness of alternative superconducting materials.

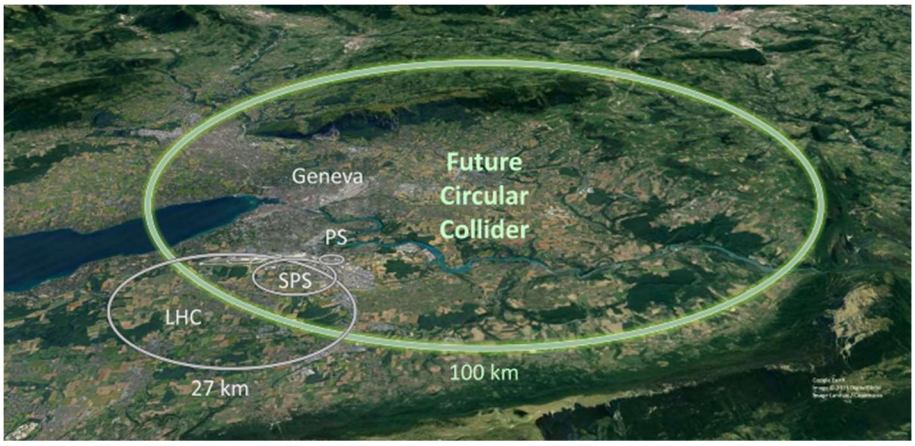

Figure 2: The Future Circolar collider tunnel compared to the existing LHC and previous accelerator. Image from https://home.cern/science/accelerators/future-circular-collider

2.2 UNCONVENTIONAL SUPERCONDUCTORS FOR APPLICATIONS AT HIGH-FIELD

The T_c and the H_{c2}, above which superconductivity disappears, were regarded as the main parameters for magnet applications of superconductors, and the continuous research for new materials with higher critical temperature and higher critical magnetic field is still ongoing. In 1986, a superconductor with high T_c was reported by Johannes Georg Bednorz and Alex Müller who discovered a T_c onset of 31 K in the Ba–La–Cu–O system with a layered perovskite structure [11]. The material is an oxide with non-cubic symmetry which behaves as a Mott insulator with antiferromagnetism before the carrier doping. In March 1987, M.K. Wu et al. reported superconductivity at 93 K in the Y–Ba–Cu–O compound system [12]. This material was the first to have a T_c higher than 77 K (boiling point of liquid N_2), and practical application of superconductivity has been greatly expected since then. High T_c cuprates superconductors have two common characteristics in their crystal structure: the structure contains a CuO_2 plane as a structural unit, and superconductivity appears when a carrier is doped in the insulating parent phase. Although various new superconductors have been reported within these frameworks, no update of T_c has been reported for cuprates since 1993. The initial enthusiasm about powerful high-field magnets, motors, generators and transmission lines working at liquid-nitrogen temperatures was based on the belief that the high values of T_c for $YBa_2Cu_3O_7$ (T_c =90 K) and $(Bi,Pb)_2Sr_2Ca_2Cu_3O_{8+x}$ (T_c up to 108 K) would assure high-field conductors similar to those for conventional superconductors. The reality turned out to be more complicated: even though cuprates conductors were developed the research and development has shown that applications at 77 K are much more challenging than those

at 4.2 K, regardless of the values of T_c and H_{c2}. In 2001 the Magnesium diboride (MgB_2), a new High-T_c intermetallic compound was discovered in 2001 [13]. MgB_2 demonstrates, since the first step of its development, to be a good candidate for large scale applications. MgB_2 shows high T_c (39 K), a simple hexagonal structure, high J_c. The main advantage of MgB_2 wires resides in the low cost of production, which is comparable to the one of NbTi, resulting from a relatively simple fabrication route and low cost of the components materials. A technical disadvantage of this system is the insufficient H_{c2}, which is comparable to that of low temperature superconductors.

The discovery of IBS as the second class of high-T_c materials, occurred in 2008 with the discovery of superconductivity at 26 K in fluorine-doped LaFeAsO by the group of the Professor Hideo Hosono [2]. The maximum T_c of 55 K in a compound of the same family was obtained by replacing La with other rare elements [14]. The discovery of IBS was accepted with surprise by the condensed matter community because of the antagonistic relation between superconductivity and magnetism induced by the presence of Iron. Extensive research into these materials started globally, and particularly in China. The paper [2] reporting T_c =26 K in $LaFeAsO_{1-x}F_x$ became the most cited report among all the original research papers published in 2008.

2.3 General aspects of Iron-based Superconductors

Four main IBS superconducting families with distinctive crystalline structure were discovered (Figure 3): the 1111 family with chemical composition LnFeAsO (Ln = Lantanides), the 122 family with chemical composition AFe_2As_2 (A= alkaline earth metal), the 111 family with chemical composition LiFeAs (or another alkali metal in the place of Li), and the 11 family with chemical composition FeCh where Ch is a chalcogen ion. These materials contain a common structural unit of the FePn (or FeCh) layer formed by the square net of Fe^{2+}, which is tetrahedrally coordinated by four pnictogen (Pn) and/or chalcogen (Ch) atoms.

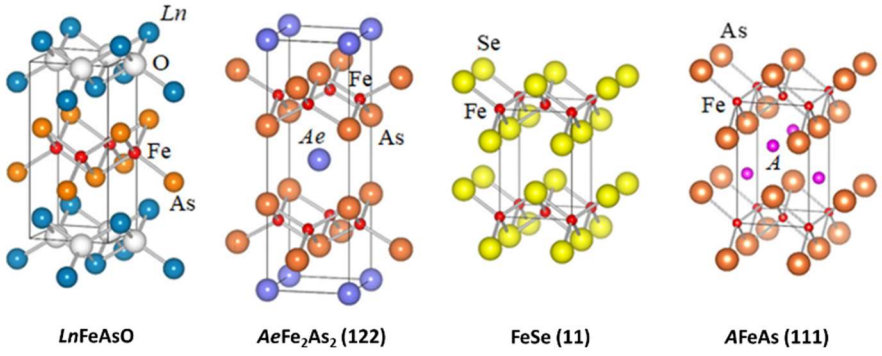

Figure 3: Crystal structure of the four main families of Iron Based Superconductors[15].

The geometry of the $FeAs_4$ tehtraedra plays a crucial role in determining magnetic and electronic properties of the system. Moreover, the As-Fe-As thetraedral bond angles plays an important role in optimizing T_c (Figure 4). Unlike cuprate superconductors, where the parent materials are Mott insulators, this layer shows conductivity without doping. An insulating blocking layer is formed by inserting a metallic element such as an alkali, alkaline earth, or rare earth metal between FePn (or

FeCh) layers. Similar to cuprates, this layered structure provides quasi-two- dimensional carrier transport properties.

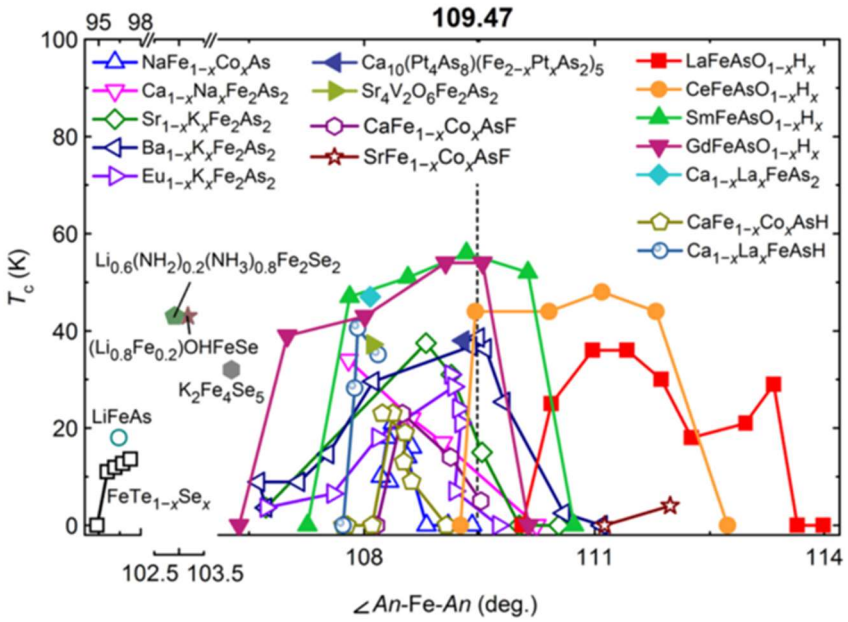

Figure 4: Correlation between T_c and the bond angle of anion–Fe–anion in various IBS. The dotted line denotes the bond angle for a regular tetrahedron [16].

The first intrinsic property that makes IBS interesting for applications is the T_c. Even if the higher T_c values still belong to cuprates, appealing values were also reported for IBS. T_c higher than 55K were obtained for the 1111 family, a T_c up to 38 K was obtained for the 122 family, a T_c up to 18 K was reported for the 111 family and up to 16 K for the 11 family and in particular for FST. H_{c2} is high, well over 50 T, which is higher than that of MgB_2 and conventional metallic superconductors such as Nb-Ti (15 T) and A15-type Nb_3Sn (29 T) as can be clearly seen in Figure 5. Thus, one of the application targets of IBS is expected to be high magnetic field magnets. The most important property for a practical application in magnets is the Irreversibility Field (H_{irr}) i.e. the maximum field at which critical current density J_c becomes zero. This value is also higher than that of MgB_2 in the same temperature range, further expecting future magnetic field application. The anisotropy factors $\gamma(=(m_c/m_{ab})^{1/2} = \xi_{ab}/\xi_c = H_{c2}^{//ab}/H_{c2}^{//c}$, where m and ξ are the effective mass and the coherence length, respectively) of the IBS are comparable to those of MgB_2 and smaller than those of cuprates (Table 1). Making such materials useful inevitably involves compromises between the good superconducting properties and the difficulties in fabrication of conductors for applications.

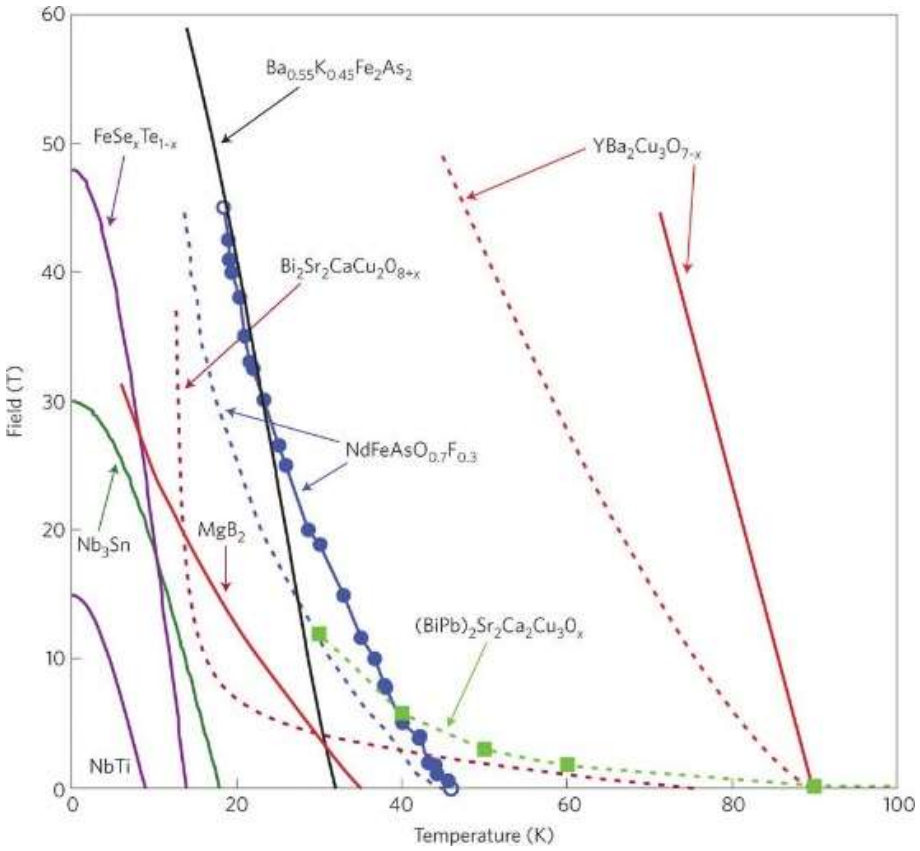

Figure 5: H(T) graphs of the most common superconducting compound. The solid line represents the upper critical field while the dashed line represents the Irreversibility fields[17].

	NdFeAs(O,F)	$Ba(FeCo)_2As_2$	Fe(Se,Te)	YBCO	BSCCO	MgB_2
T_c (50% R_n) (K)	47.4	22.0	15	93	85–90	39
$-\mu_0 dH_{c2}^{\perp ab}/dT$ (T K^{-1})	2.1	2.5	14	0.7–1	0.7–6	0.05
$-\mu_0 dH_{c2}^{\parallel ab}/dT$ (T K^{-1})	10	4.9	26	3-4	20–45	0.3
γ_H	5	2	2–3	4–14	50–60	3–5
$\mu_0 H_{c1}^{\parallel c}$ (mT)	15	40	4.5	20	3.7	100
ξ_{ab} (nm)	2.1	2.9	1.5	2.1–2.3	2.7–3.2	10
ξ_c (nm)	0.6	1.5	0.6	0.5–0.6	0.4–0.5	2
λ_{ab} (nm)	200	200	490	160	180	50–100
Ginzburg number, *Gi*	$4{\cdot}10^{-4}$	$2{\cdot}10^{-5}$	$1{\cdot}10^{-3}$	$>10^{-3}$	$10^{-3}-10^{-2}$	$<10^{-5}$

Table 1: Superconducting state properties of IBS compared to cuprates and MgB_2 [18].

2.4 Similarities between Iron Based Superconductors and Cuprates

IBS and cuprates have a lot of common characteristics and a direct comparison between this two is unavoidable: the knowledge about the cuprates about their properties and the technology to produce wires and tapes is moreover fundamental to understand IBS and to technological develop new conductors. Cuprates and IBS are both layered materials in which superconductivity occurs primarily

on atomic planes (the Cu–O planes in the cuprates and the Fe–As or Fe planes in IBS). In cuprates and in IBS the superconductivity competes with an antiferromagnetic state, since superconductivity in the cuprates occurs on doping a Mott antiferromagnetic insulator, whereas IBS become superconducting by doping a parent antiferromagnetic semi-metal. IBS and cuprates have small Cooper pairs with $\xi \approx 1$–2 nm, which derives from their high critical magnetic field and low carrier density at the Fermi energies compared to conventional superconductors. Another characteristic of these two families is the anisotropy factor γ, which is quite small for IBS ranging from ~1 to ~5 and which is very large from ~6-7 to $>10^4$ –10^5 for the cuprates (Table 1). The small coherence length ξ and the high anisotropy factor γ contributes to the enhancement of thermal fluctuations, which significantly reduces the useful T–H domain in which superconductors can carry currents even in the presence of pinning. Moreover, the small coherence length ξ and the complex chemical structure that characterize both IBS and cuprates cause the problem of the weak links at Grain Boundaries (GB), as a result of which the GB deteriorate the current-carrying capability of conductors.

2.5 The Grain Boundaries issue

An essential requirement for large scale applications is the capability to carry current over a long length, in other terms current needs to flow along polycrystalline materials through GB. The ability of Cooper pairs to cross the GB regions, which are normally non-superconducting and with a depressed order parameter, depends on the coherence length which is some tens of nanometres in the conventional superconductors but it can be very small in the case of IBS and cuprates. Discovered in 1988, the current-limiting grain boundaries in cuprates [8] were immediately recognized as a serious obstacle for their applications because, instead of flowing along the wire, the current breaks into disconnected loops circulating in the grains as shown in Figure 6 .

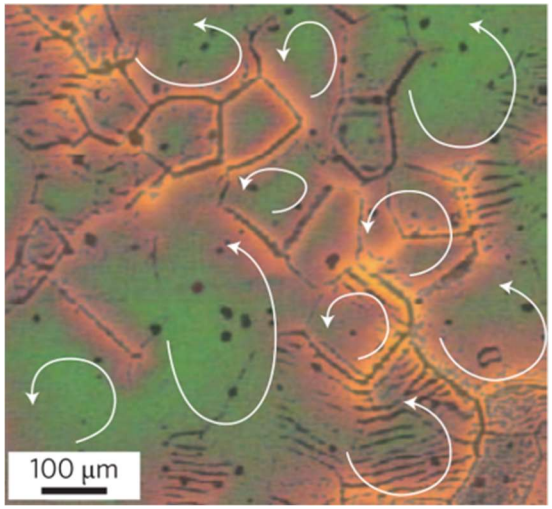

Figure 6: Magnetic granularity in a $YBa_2Cu_3O_{7-x}$ polycrystal revealed by magneto-optical imaging. Here the yellow contrast shows the preferential penetration of magnetic flux along the network of grain boundaries (black lines). As a result, instead of flowing along the conductor, current breaks into weakly connected current loops (white arrows) circulating in the grains [17].

For $YBa_2Cu_3O_{7-\delta}$ it was found that the current density through a grain boundary $J_{gb}(\theta) = J_0 \exp(-\theta/\theta_0)$ drops exponentially as the misorientation angle θ increases [8]. Very early studies on the critical current density of 1111 polycrystals have highlighted the strong granularity of these compounds, which limits the global J_c flow across the samples [19]. A study aiming to investigate the nature of weak link GB in IBS was made with $Ba(Fe_{1-x}Co_x)_2As_2$ thin films grown on bi-crystals with different misorientation angle between the grains. It was shown that the critical current density was strongly suppressed for θ<3° [20]. This J_c suppression is very similar to the one reported for $YBa_2Cu_3O_{7-\delta}$ [8], even though a close comparison suggests that in IBS the suppression is less severe than in cuprates. A similar experiment on $Ba(Fe_{1-x}Co_x)_2As_2$ thin films grown on bi-crystals was done by Katase et al. [21]. In this experiment a larger critical angle θ≈9° was reported. The experiment also pointed out that the GB in IBS are probably metallic and not insulators as in the case of cuprates. Other results show that the misorientation angle is not the only parameters that determines the weak link behaviour at grain boundaries, but also the orientation of field in respect to GB plays an important role. Three types of GB were found in 122 polycrystals, the clean GB, GB which contained only an amorphous layer of ≈10 nm width and GB which have a tri-layers composed of amorphous-crystalline-amorphous with a total width of about 30 nm. Many experiments regarding the effects of GB on the critical current density were also performed on thin films of the 11 phase $FeSe_{0.5}Te_{0.5}$. Si et al showed some results obtained on epitaxial $FeSe_{0.5}Te_{0.5}$ thin films deposited on $SrTiO_3$ bi-crystals: they identified a critical misorientation angle of about 9° below which J_c does not decrease significantly as a function of misorientation angle and survives to very high magnetic fields [22]. The critical angle observed in the $FeSe_{0.5}Te_{0.5}$ thin films is about twice as high as in cuprates, and above this angle the GB are weakly linked. Si et al also showed that the J_c across the grain boundary with a 24° misorientation angle are modulated by the magnetic field, as in a Josephson junction, this allow the applications of this phase for superconducting electronic applications. Sarnelli et al conducted an experiment on nano-strips produced with standard optical lithography and ion milling starting from a FST thin films deposited through Pulsed Laser Deposition on $SrTiO_3$ bi-crystal substrate at CNR-SPIN [6]. The experiment showed results that agree with the results of Si et al previously discussed [22]. Figure 7 shows a summary of the dependence of J_c from the misorientation of GB for different IBS phases grown as thin films on bi-crystals with a misalignment up to 45° compared to the $YBa_2Cu_3O_{7-\delta}$ behaviour. P-doped Ba-122 showed a high inter-grain J_c of 1 MA/cm^2 at θ_{GB} = 24°. Moreover, the critical current density across GB for Ba-122 is higher than for $YBa_2Cu_3O_{7-\delta}$ beyond θ_{GB} = 24°. For all IBS the critical angle is around 9°, indicating that an in-plane alignments of IBS grains less than 9° usually do not causes the suppression of current. The initial slope of J_c as function of the angle for IBS is very similar to the $YBa_2Cu_3O_{7-\delta}$, but the two behaviours become very different for θ_{GB} = 24°: above this angle J_c of $YBa_2Cu_3O_{7-\delta}$ continue to decrease with the increasing angle, instead for IBS the J_c stabilizes to a constant value.

In conclusion, cuprates and IBS show a lot of common features that makes them very attractive for their very good superconducting properties but that make them also very complex to be produced as conductors. However, the discussed critical aspect which characterized the IBS are not significantly marked as in the cuprates. The small ɣ, high crystallographic symmetry, and large critical GB angle for J_c indicate that the IBS are appropriate for fabrication of superconducting wires, tapes application because high and three-dimensional crystallographic orientation is not necessary rather than cuprates.

Moreover, a distinctive characteristic of IBS is the robustness of T_c to impurity (i.e.,doping), which allows to select various doping methods to induce high- T_c superconductivity[16].

The less critical GB in IBS allows the production of IBS wires with methods that are not efficient to control the texturing of the superconducting phase and consequently unsuitable for the production of YBCO conductors. Therefore, it is expected that IBS are applicable to wires, tapes, and coated conductors for high magnetic fields.

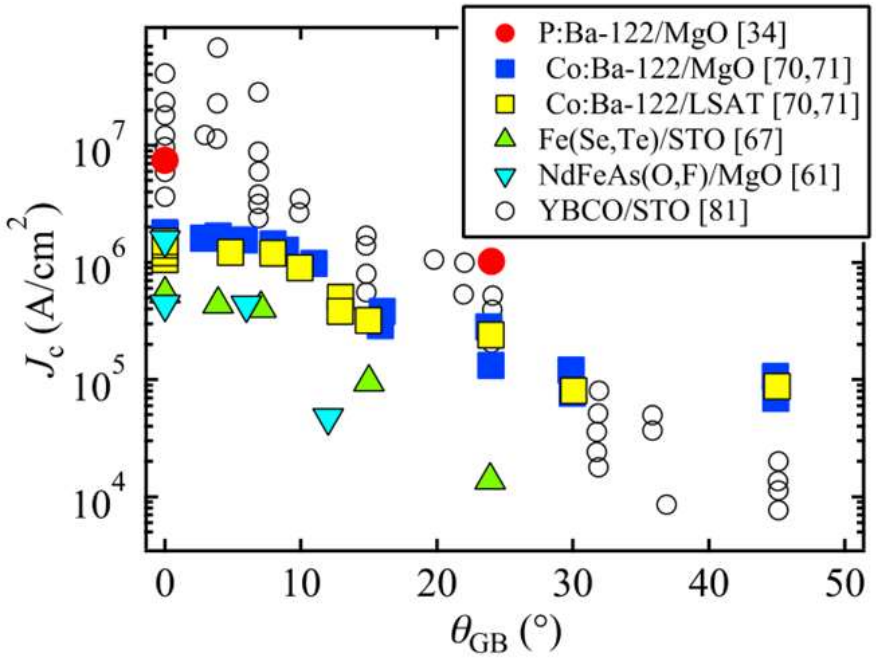

Figure 7: The dependence of inter-grain J_c to misorientation GB angle for various FBS bi-crystals, compared to YBCO [23].

2.6 IRON-BASED COATED CONDUCTORS

The problem of the GB was addressed for cuprates developing the CC technology. The CC technology consists in growing epitaxially the superconducting phase, i.e. the $YBa_2Cu_3O_{7-\delta}$, on textured buffer layers reducing the high-angle grain boundaries and consequently preventing the deterioration of J_c across GB. To produce a biaxially textured superconductor tape two different type of substrates have been developed (Figure 8): the Ion-Beam Assisted Deposition (IBAD) substrates, where an appropriate oxide is grown on a polycrystalline and randomly oriented metallic tape, and the Rolling Assisted Biaxially Textured Substrates (RABiTS), where the biaxially orientation is provide by the metallic tape. In the IBAD, by the action of the ion beam, the oxide grows on the metallic tape with a crystalline texturing, even if the tape is randomly oriented, and the template is suitable for the deposition of the superconducting film, which grows epitaxially on the oxide acquiring its texturing. IBAD substrates have a very complex structure: the metallic tape is usually made of untextured Hastelloy C-276, on this tape five oxide buffer layers are deposited which are necessary to reach the suitable biaxial orientation for the $YBa_2Cu_3O_{7-\delta}$.

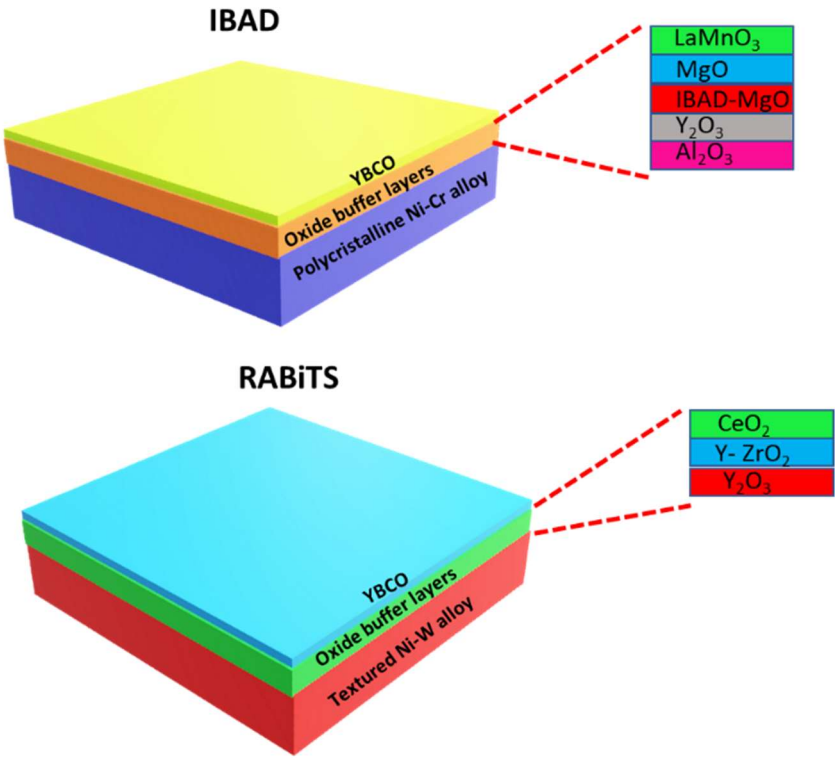

Figure 8: Architectures of the IBAD and RABiTS commercial substrates for CC.

In the RABiTS, the biaxial orientation is provided by the metallic tape, typically made of $Ni_{1-x}W_x$ alloys, rolled and heat treated in an appropriate way. $Ni_{1-x}W_x$ alloy, unlike Hastelloy, was developed and optimized to fulfil the requirements of CC technology. Lots of efforts were done to produce an alloy with a suitable lattice parameter for the deposition of the thin films, with a proper Stacking Fault Energy (SFE) to obtain a sharp cube textured structure [24], a suitable mechanical strength and a reduced magnetism in respect to Ni [25]. NiW5% alloy is, to date, the most common used alloy for RABiTS and is now produced by several laboratories and industries, even though is not easily available. On NiW5% three oxide buffer layers are deposited as epitaxial thin films in order to reach the best biaxial texturing for the deposition of the superconducting phase.

The IBAD and RABiTS substrates, usually called 'technological substrates', are commercially available, and their template has been strongly optimized for the deposition of $YBa_2Cu_3O_{7-\delta}$, which not only requires a strong biaxial texturing but also a substrate than can remain unaltered at 900°C in Oxygen atmosphere, condition used for the deposition of this superconducting phase.

Considering that IBS present, as cuprates, weak link grain boundaries, the CC technology seemed the best way to produce IBS technological tape. Several groups have published important results on IBS

deposited on technological substrates and even if other techniques are used to produce technological wires and tapes (see Appendix), CC have shown the best performances.

Interesting results were obtained depositing the Co- an P- doped Ba-122 phase [26–29] and NdFeAs(O,F)[30] on technological substrates. Figure 9 shows the J_c (H) at 4.2 K of different IBS thin films on technological substrates, compared to films deposited on single crystalline substrates. As can be seen the Ba-122 phase shows the highest J_c, both in case of the P and of Co doping. However, the J_c obtained was always lower than for the films on single crystals; for the Co-doped Ba-122 a cross over is reported at 7.5 T. For the P-doped and the Co-doped Ba-122 there is a slight difference between the J_c in self-field of the film deposited on technological substrate and on single crystal, this can be ascribed to the presence of pinning centre in the films deposited on single crystals, and to the fact that the deposition on single crystals was strongly optimized.

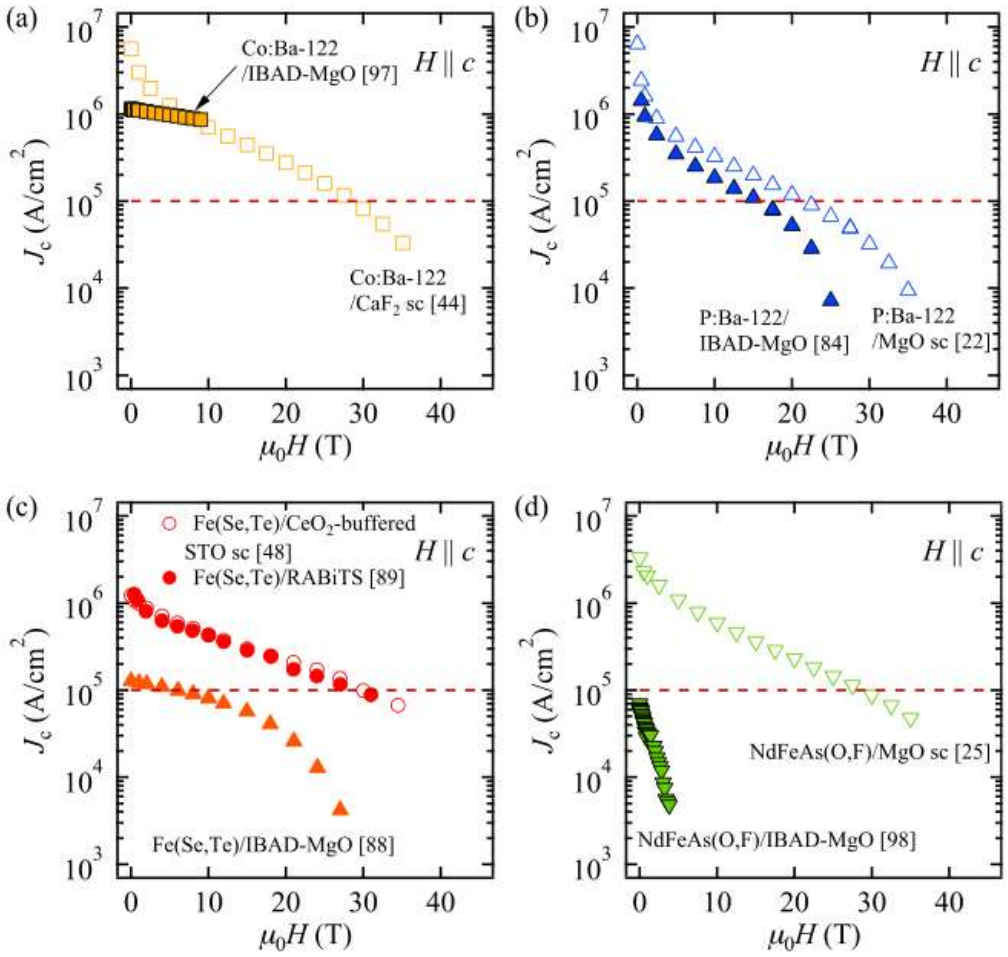

Figure 9: J_c -H properties of various FBS thin films on technical substrates [23].

Regarding the 11 phase, the J_c of FST deposited on CeO_2/Y_2O_3 buffered RABiTS is comparable to the optimized thin films on single crystals. The highest difference between the performance of thin films on single crystals and on technological substrates was reported for the NdFeAs(O,F) which can be ascribed to a strong F diffusion along GB. Good performances were also obtained fabricating FST thin films on technological IBAD substrates with a buffer layer of MgO deposited through the ion beam assisted technique (IBAD-MgO). FST and MgO have quite different lattice parameters: MgO (a= 4.21 Å)

and the FST phase (a=3.81 Å). The presence of a strong strain induced in the film by the substrate decreases the T_c down to about 11 K, which is quite low if compared to FST grown of single crystals which can reach up to 21 K [3]. Despite the large crystalline mismatch and the low T_c, FST thin films with very good texturing, the in-plane Full Width at Half Maximum (FWHM) is $\Delta\phi$=4.5° and out of plane is $\Delta\omega$=3.5°, were obtained on IBAD-MgO. FST on IBAD-MgO does not show the problem of weak link GB, and an isotropic J_c over 10^4 A/cm^2 at 4.2 K and 25 T was reported [31]. FST deposited on RABiTS substrates gave even better results (Figure 10). The CeO_2-buffered RABiTS template provided a strong enhancement of T_c which reached an onset of 20 K, thanks to the perfect match of the FST lattice parameter a, with the half of the diagonal of the CeO_2 cell (a_{CeO2}= 5.41 Å, half of the diagonal CeO_2 ≈ 3.82 Å). Despite the worst in plane orientation of the FST thin film $\Delta\phi$=6°, an isotropic J_c≈ 0.1 MA/cm^2 at 4.2 K and 30 T was observed [5].

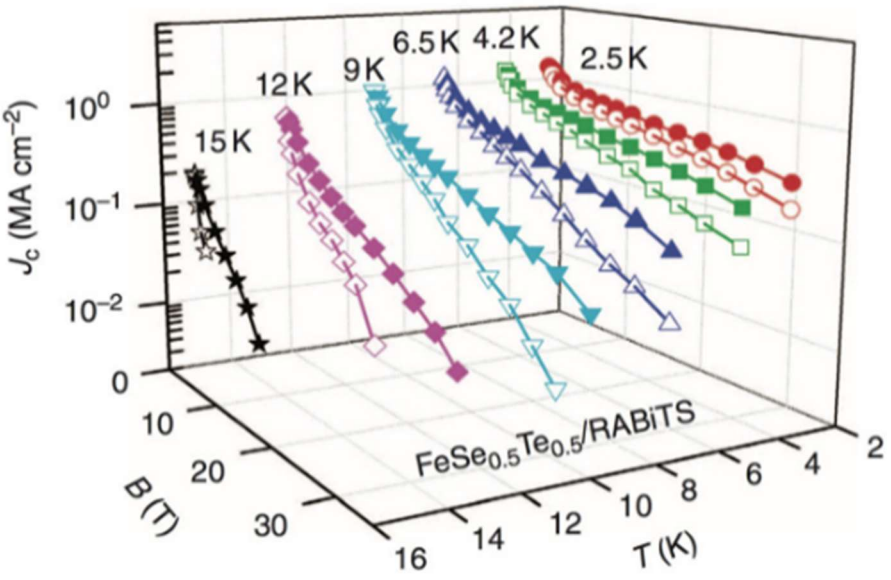

Figure 10: J_c as a function of applied magnetic field of 11 CC on RABiTS template measured at different temperatures, full symbols are for H//ab while empty symbols are for H//c [5].

Less well textured substrates and amorphous substrates were, also, already used for the deposition of IBS thin films. Sato et al [32] demonstrated that for $BaFe_2(As_{1-x}P_x)_2$ thin films grown with Pulsed Laser deposition, the worst alignment of the IBAD substrate causes an increment of the critical current density (Figure 11). In that sense not only, the GB are not detrimental for the transport properties of the film, but they are very efficient pinning centre.

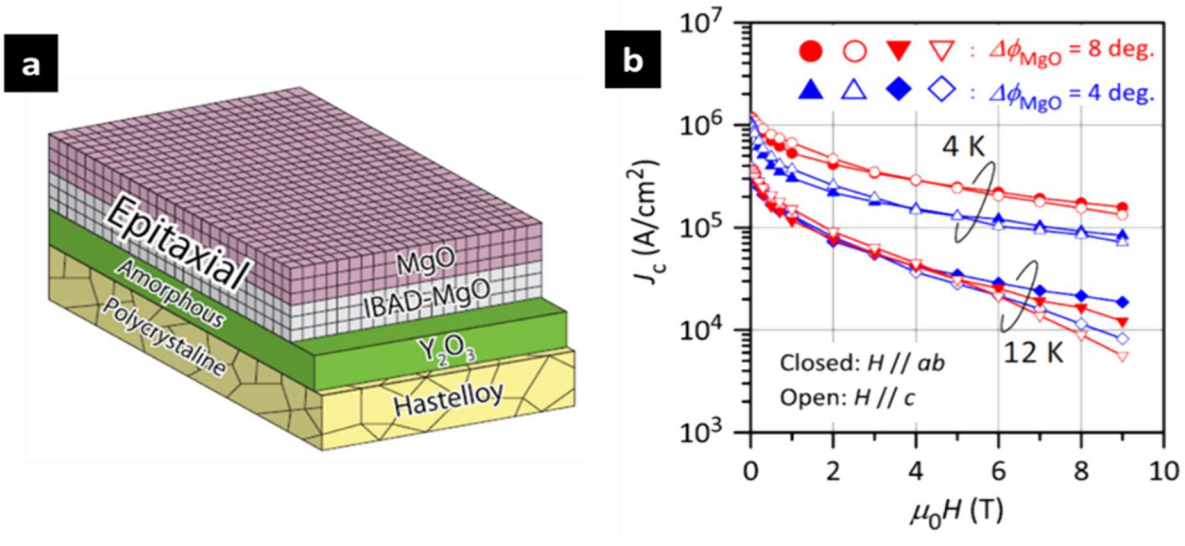

Figure 11: a) Less well textured IBAD substrate used in [32] for the deposition of $BaFe_2(As_{1-x}P_x)_2$ thin films. b) J_c of $BaFe_2(As_{1-x}P_x)_2$ thin films deposited on IBAD substrate with a misalignment angle of 4° and 8°.

Significant results were also obtained depositing FST thin films on a less well textured IBAD-MgO with an $LaMnO_3$ (LMO) buffer layers. An in-field J_c of 0.35 MA/cm^2 at 9T and 4.2 K was reported, even if the film shows a T_c of about 16.8 K and a quite large in-plane orientation $\Delta\phi$=7.8°[33].

Moreover, $FeSe_{0.1}Te_{0.9}$ thin films with a T_c of 10 K, and a J_c of 2.1×10^4 A/cm^2 in self-field, were thus obtained on a metallic substrate with only one Al_2O_3 amorphous buffer layer [34]. A T_c of about 7 K was also obtained by the same group depositing FST thin films on flexible Mica substrates without any buffer layer. Although the crystal structure and lattice parameter between FST and Mica is very different, interestingly, only FST (00l) peaks can be observed from the XRD patterns [35]. These results on amorphous or not suitable substrates seems to suggest a mechanism of self-orienting growth of the FST phase [34].

3 DEVELOPMENT OF 11 COATED CONDUCTORS FOR HIGH FIELD APPLICATIONS

In the previous chapter the great potentiality of IBS for high field applications was shown. Among all the IBS families the 11, is the simplest, and is quite attractive because of the absence of toxic arsenic. As already shown, FST thin films have been successfully grown on single crystalline substrates [6,21] and on technical commercially available metallic templates [5,31].

In this context, my PhD thesis is moving forward trying to simplify the technical substrate, reducing the degree of orientation or removing buffer layers in order to make these CC easy to produce, cost-effective and consequently appeal for large scale application.

I have worked on the development of 11 CC with simpler and cost-effective RABiTS. The simplicity of the substrates could derive from both from the employment of commercial metallic alloy instead of the custom- made NiW5% but also from the modification of the architecture of buffer layer. Buffer layers can also be deposited with simple and scalable method, can be reduced in number or even completely removed. These possibilities singularly or combined contribute to the simplification and consequently to the cost reduction of 11 CC.

The work started from the long-lasting experience of the research group of CNR Spin Genoa on the deposition of 11 thin films with PLD and from the idea that with a suitable biaxially textured metallic substrate could be possible produce a CC without any buffer layer because the deposition of FST thin films is performed in Ultra-High Vacuum at quite low temperature.

In this chapter the different CC architectures studied are presented, starting from the development of simpler metallic substrates made of a commercial alloy and without any buffer layer to more complicated substrates based on NiW5% metallic tapes with different nitrides and oxides buffer layers, together with a study of the properties of the FST thin films deposited on such different templates.

In detail, this chapter is divided in three main parts:

A)11 thin films deposition and characterization: The first part describes the deposition of FST thin films with the PLD. Starting from the optimized parameters for the deposition on single crystal substrates, we conducted two preliminary studies necessary to deposit high quality thin films on metallic substrates.

B)11 CC on in-house manufactured substrates: In the second section is presented the development of 11 CC on in-house manufactured substrates. We started from the development of Invar 36 substrate on which we deposited 11 thin film without any buffer layer and with nitrides and metallic buffer layers. The last part of this section is devoted to the description of the Hastelloy C-276 substrates in which we exploit the native passivating oxide layer as buffer layer.

C)11 CC on ENEA substrates: The last section of the chapter describes the activity made in collaboration with ENEA centre of Frascati regarding the development of 11 CC on NiW5% substrates from EVICO with different oxides buffer layers deposited at ENEA's laboratory.

A) 11 THIN FILM DEPOSITION AND CHARACTERIZATION

During the last years very important results were obtained depositing the FST phase with PLD on various single crystal substrates and a very detailed analysis on this type of thin films was performed [6,36,37 38]. Best results in terms of crystalline growth and superconducting properties were obtained using (001) CaF_2 substrate [4]. FST deposited on CaF_2 grows with an in-plane rotation of Φ= 45 ° with respect to the *a* axis due to the good matching with the half of the diagonal of CaF_2 crystalline cell. Moreover, the films show a T_c near 21 K [3] thanks to the strain induced in the film by the substrate and an isotropic J_c around 10^6 A/cm^2 at 4.2K and 0 T , slightly influenced by the increasing magnetic field [4]. An analysis of the film with Transmission Electron Microscope (TEM) revealed the presence of small regions where the crystalline lattice is disturbed. Such defects might originate from a different local stoichiometry between Se and Te since FeTe and FeSe phases show quite different c axis values, 6.285 Å and 5.486 Å, respectively. These anisotropic defects act as pinning centre, providing high J_c very stable in field and almost isotropic[4]. Optimized 11 thin films were deposited in an ultra-high vacuum PLD system equipped with a Nd:YAG laser at 1024 nm, using a $FeSe_{0.5}Te_{0.5}$ target, produced at the Chemistry Department of the University of Genova, directly synthesized with a two-step method[39]. The optimized laser parameters to obtain high quality epitaxial 11 thin films [4] were a 3 Hz repetition rate, a 2 J/cm^2 laser fluency (2 mm^2 spot size) and a 5 cm distance between target and sample. The deposition was carried out at a residual gas pressure of 10^{-8} mbar while the substrate was kept usually at temperature around 300°C. These growth conditions and the films grown in this condition on CaF_2 will be defined in the following 'standard'. The evolution from thin films on single crystals to thin films on metallic templates is not obvious and requires preliminary studies to prove the possibility to obtain high quality thin films even if the substrate is not optimal as is a single crystal. Particularly, problems related to film thickness, thermal expansion of the substrate and crystalline match between substrate and film were addressed starting from the optimization of the process on single crystal and then transferring the process to the templates. In this section two preliminary studies conducted on films deposited single crystals with the final aim to improve the properties of the film deposited on metallic substrates, will be discussed in detail. All the films deposited on single crystalline substrates and metallic template were characterized with a four-circle Siemens Kristalloflex 810 (Cu Kα radiation) and a PANanalytical Mod X'PERT PRO two-circle diffractometer (Cu Kα radiation), in order to identify their purity, crystal structure and orientation, both in- and out-of-plane. Electrical transport properties of the films as a function of temperature and magnetic field were measured in a Physical Properties Measuring System (PPMS) by Quantum Design up to 9T. In order to allow the measurement of critical current and of resistive transitions in magnetic field, the films were patterned through standard optical photolithography, and the etching was performed by water-cooled argon ion milling (argon ion energy 500 eV). After the milling process, the photoresist was removed with acetone at 50°C for a few tens of seconds and dried in nitrogen air. A Hall bar-shaped micro-bridges 0.25x1 mm^2 in size was realised. The films deposited on metallic substrates were protected the process of patterning with a layer of Au, deposited with sputtering, of about 60 nm of thickness. The deposition of nitrates buffer layers on Invar were made at CNR Spin Naples by Dr. Mikhail Lisintsky with sputtering. Electron back-scatterd diffraction (EBSD) characterization, pole figure measurements and the characterization related to chemical buffer layers and the development of substrates based on NiW5% were performed at ENEA centre of Frascati by Dr. Angelo Vannozzi and Dr. Giuseppe Celentano.

A.1 STUDY OF THE DEPOSITION OF HIGH-THICKNESS 11 THIN FILMS ON CaF_2 (001) SINGLE CRYSTAL

For the CC technology a thin film with a thickness of at least 500 nm is required. Usually on RABiTS, films of thickness of about 1µm are grown. It is not obvious that high thickness films maintain good superconducting properties: the increased thickness can lead to a reduction of the strain in the film, causing a reduction of T_c as reported for other substrates[3], but it can also worsen the film texturing and at last a possible delamination of the film from the substrates has to be envisaged. For these reasons, starting from a standard film of 200 nm, films of higher thickness were deposited on (001) CaF_2 single crystals following the 'standard' conditions previously discussed. Figure 12 shows the X-ray diffraction (XRD) analysis and the resistance as function of temperature (R(T)) measurements of thin films with a thickness up to 500 nm. As can be seen all the films show an epitaxial growth on the substrates with an out-of-plane orientation between 0.8° and 0.6°. The best results in terms of in-plane and out-of-plane orientation are reached for films of thickness between 300 and 400 nm, but increasing the thickness T_c decreases of up to about 4 K: the highest T_c belongs to the thinner films thanks to the effect of strain induced in the film by the substrate [36]. These results confirm the possibility to obtain a good growth and a good T_c in thick films but also that even if the film is thick it does not delaminate from the substrate.

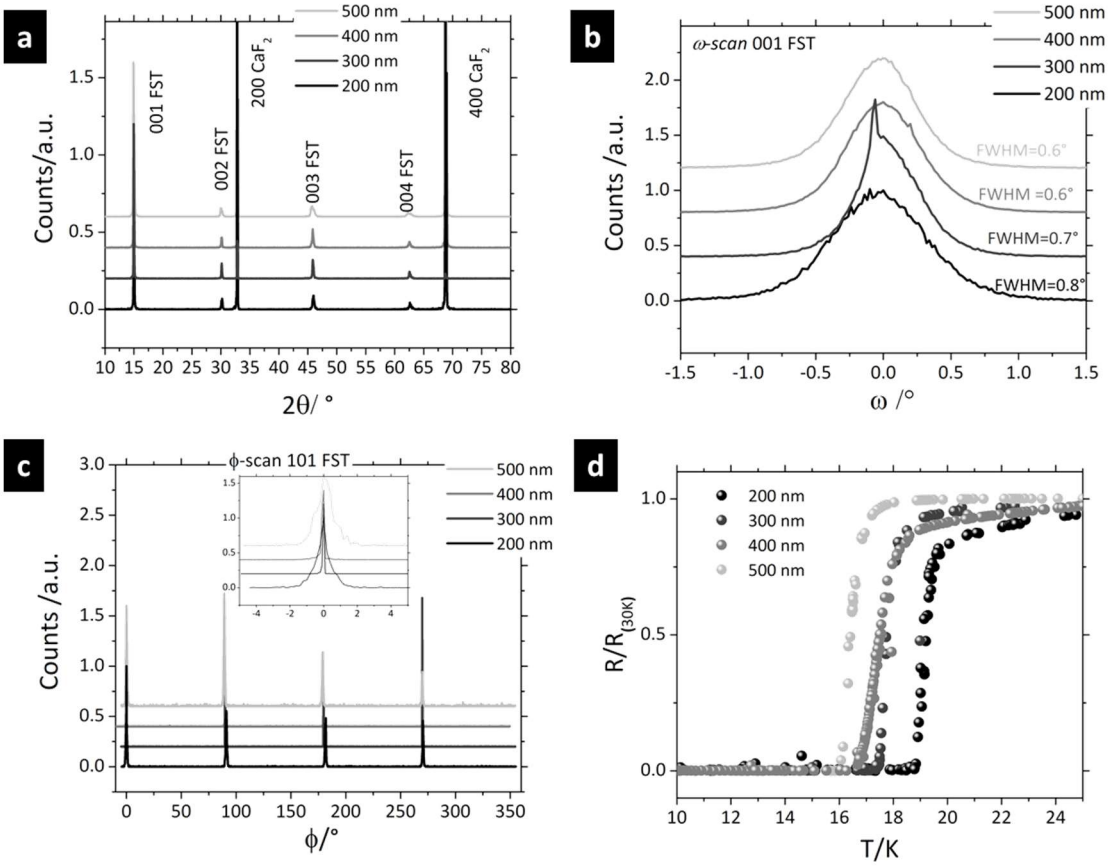

Figure 12: XRD and R(T), normalized at 30 K, measurements of FST thin films with different thickness up to 500 nm, deposited on CaF_2 substrates.

A.2 STUDY OF THE DEPOSITION OF 11 THIN FILMS AT LOW TEMPERATURE

The quite low 'standard' temperature of deposition of FST thin films (around 300°C) is not a problem when a single crystal is used as substrate but could be a problem if the substrates is a metal which could be, by its very nature, subjected to large thermal expansion. The problem of thermal expansion arose when we start to consider metals as a candidate to become a substrate for CC without any buffer layer. To overcome the problem, we started to study the possibility to deposit 11 phase at low temperature. The first attempt of this study was done on single crystal CaF_2 substrate. In Figure 13 the XRD analysis and the resistance measurements of 11 thin films grown on CaF_2 from 317°C down to 200°C are shown. All the films, down to 200°C, show all the (00l) peaks, an out of plane orientation and a superconducting transition. However, the out of plane orientation and the T_c were significantly worsened with the reduction of the deposition temperature declining from ≈317°C to ≈200°C.

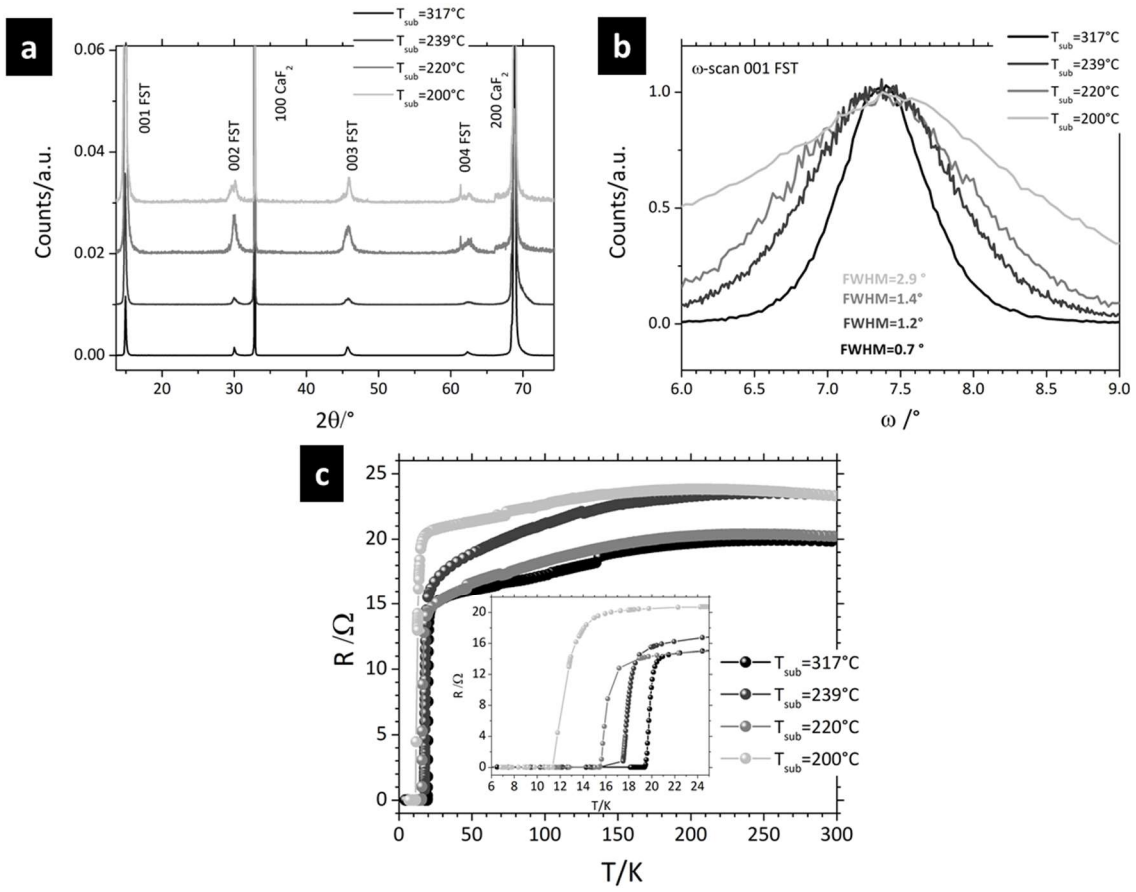

Figure 13: a) θ-2θ scan b) Rocking curve of the 001 of FST c) R(T) of 11 thin films deposited on CaF_2 single crystals at temperature between 313°C and 200°C

In order to improve the quality of the films grown at low temperature, we followed the idea in the paper by S. Molatta et al[40], we deposited a seed layer of FST using high deposition temperature (400°C) and high frequency of laser (10 Hz). We verified that these conditions of growth ensure that the seed

layer is not superconductor. On the seed layer we deposited films at 220°C using two different procedures: deposition of the seed layer followed by cooling of the substrate and then deposition of the film, or deposition of the seed layer immediately followed by the deposition of the film during the cooling. In this last case it is possible to assume that an intermediate layer between the seed layer and the superconducting thin film is formed during the cooling of the substrate.

In Figure 14 we report the XRD analysis and the resistivity measurements of a film on CaF_2 deposited at 220°C (black) compared with a film with seed layer (grey) and a film with seed layer and intermediate layer (light grey). The presence of the seed layer leads to an improvement of the out of plane orientation of about 0.8°, and an improvement in T_c of about 4 K. The largest improvement in T_c is observed in the film with the intermediate layer. Probably the continuous growth of the film causes a good adjustment of the film structure on the seed layer. Indeed, from θ-2θ scans, we see that all peaks of the 11 phase are doubled, meaning that seed layer and film have slightly different lattice parameters.

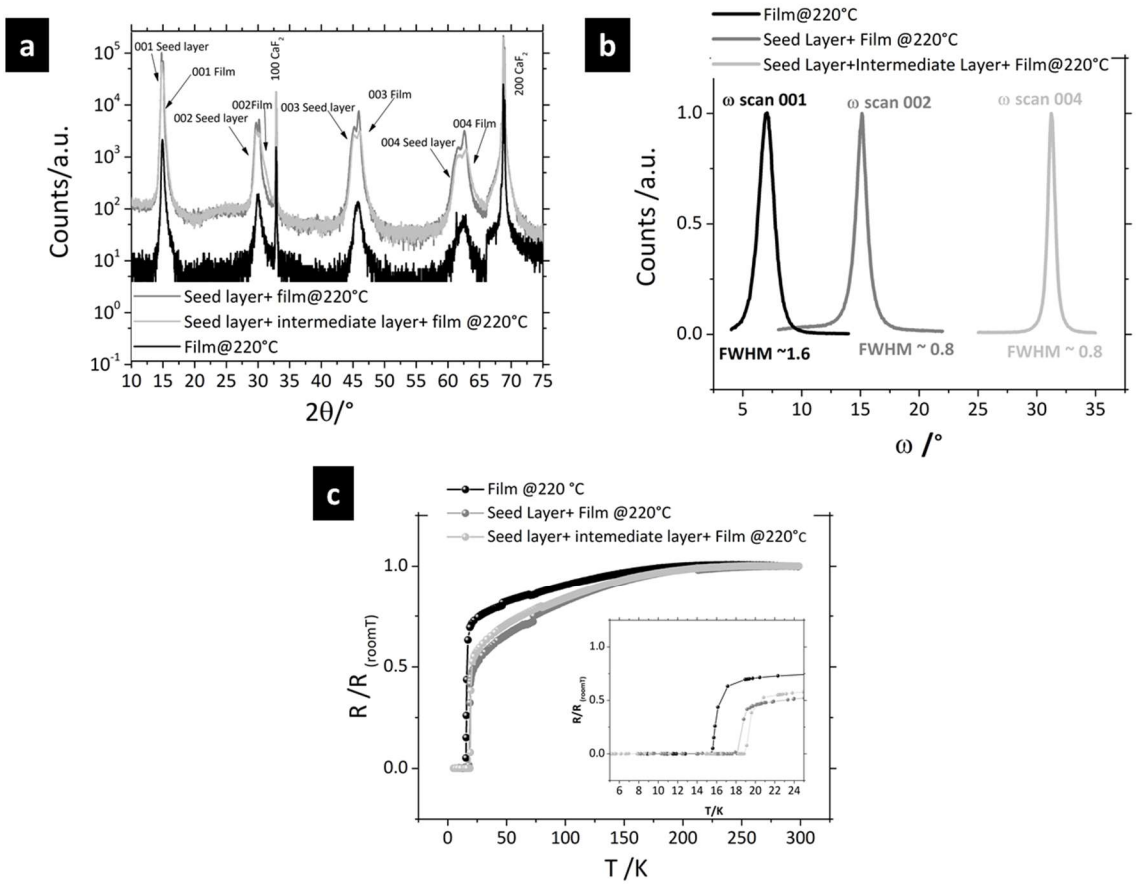

Figure 14: XRD measurements and R(T) performed on a FST single layer thin film deposited at 220°C on CaF_2 (black), one FST film with a seed layer deposited on CaF_2 (grey) and on a FST thin films deposited with buffer layer and an intermediate layer on CaF_2 (light grey).

B) IN-HOUSE MANUFACTURED SUBSTRATES

B.1 INVAR 36 SUBSTRATES

B.1.1 Invar substrates development

Invar 36 is a commercial Ni/Fe alloy, well known for its very low thermal expansion coefficient. The thermal expansion coefficient of Invar 36 is about one order of magnitude lower than the thermal expansion coefficient of a steel for all temperatures, it is minimum around room temperature and it starts to increase in the range of temperature between 200°C and 300 °C (see Table 2).

Thermal Expansion Data on 36 Per Cent Nickel-Iron Alloy

Temperature Range		Mean Coefficient of Linear Expansion	
°F	°C	per°F	per°C
-400 to 0	-240 to -18	1.20×10^{-6}	2.16×10^{-6}
-200 to 0	-129 to -18	1.10×10^{-6}	1.98×10^{-6}
0 to 200	- 18 to 93	0.70×10^{-6}	1.26×10^{-6}
200 to 400	93 to 204	1.50×10^{-6}	2.70×10^{-6}
400 to 600	204 to 316	6.40×10^{-6}	11.52×10^{-6}

Table 2: Linear thermal expansion coefficient of Invar 36 alloy [41].

Invar 36 has a face centred cubic structure, space group Fm-3m, with a lattice parameter of about 0.359 nm. This is quite close to the in-plane lattice parameter of tetragonal 11 (0.379 nm), so an epitaxial relation (001)[100] 11|| (001)[100] Invar 36 can be expected. Moreover, since both the Invar 36 alloy and 11 phase are mainly composed of Fe, chemical compatibility seems to be possible. Glowacki et al. have demonstrated the possibility of obtaining a biaxially textured Invar tape that can be suitable as a substrate for YBCO CC [42]. Starting from commercially available Invar 36 rod, a suitable process to obtain cube texturing with a combination of cold drawing, cold rolling and recrystallization heat treatment was developed. Starting from a 10 mm rod, drawing (10% cross section reduction) followed by flat rolling was applied (10% thickness reduction steps at a line speed v of 0.7 – 2 m/s). With this procedure, tapes with a thickness of 50 – 120 µm were obtained, with a maximum thickness reduction of 99.5%. After deformation, all tapes were subjected to a recrystallization heat treatment, which was performed in a furnace at 1000 °C for 1 to 2 hours. Due to the high sensitivity of Ni/Fe alloys to oxidation, before heat treatment the tube was evacuated, and the heat treatment was performed in flowing Ar/H_2. All the tapes were characterized by XRD before and after heat treatment with a four-circle diffractometer (Cu Kα radiation). The 70 µm thick Invar 36 tape showed the best results in terms of biaxial texturing. Figure 15 shows the XRD θ–2θ scan of the as-received Invar 36 rod (black), the 70 µm tape produced by mechanical deformation before (dark grey) and after (light grey) the heat treatment. The as-received rod shows three crystalline peaks characteristic of the alloy. After mechanical deformation the tape shows the (220) and (200) peaks, while after the heat treatment the tape shows only the (200) reflection, meaning that a preferential orientation (001) was obtained. The

ω scan, shown in Figure 16 a, highlights an out-of-plane orientation along the (200) direction with a FWHM of 6° in the Rolling Direction (RD) and of 9° in the Transverse Direction (TD). Figure 16 b reports the φ scan along the (220) direction of the Invar tape, which shows an in-plane orientation with a FWHM of about 10°.

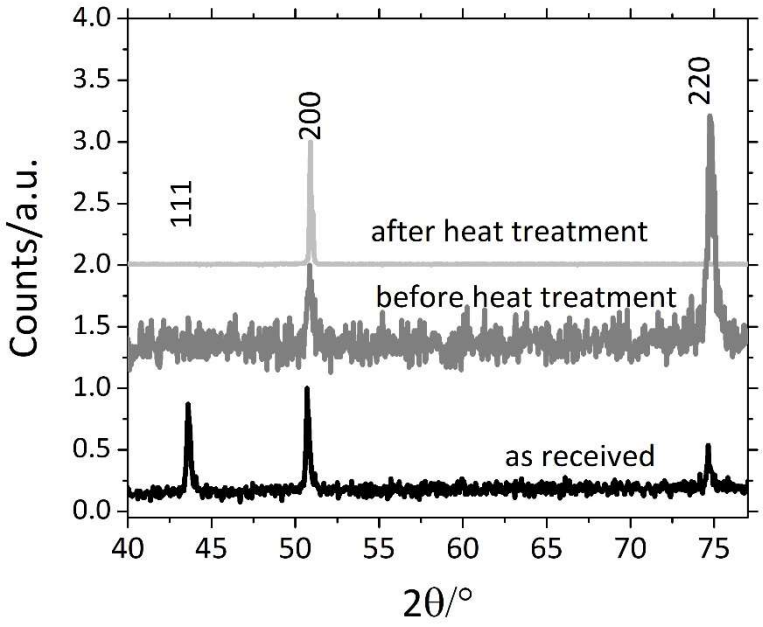

Figure 15: XRD θ–2θ analysis of Invar 36 starting from the as received rod (10 mm diameter) in black and going through all the steps of the substrate preparation. In dark grey, the tape before heat treatment, which shows only a (200) peak; and in light grey, the cube textured tape after heat treatment.

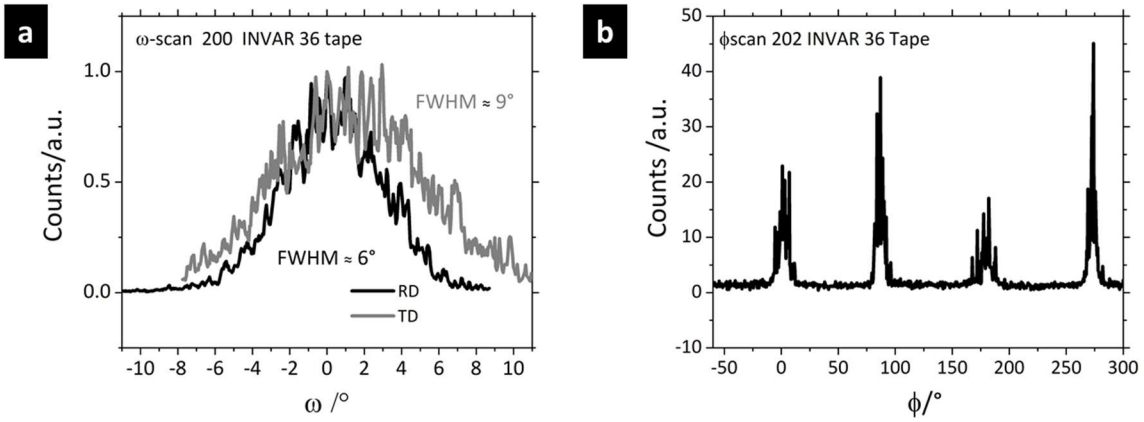

Figure 16: a) ω scan of a 70 µm thick Invar 36 tape in the rolling direction (black curve) and the transverse direction (grey curve). b) ϕ scan along the (202) direction of a 70 µm thick Invar 36 tape.

The microstructure of the Invar 36 substrate has been analysed by means of EBSD analysis at ENEA Frascati. Figure 17 shows the EBSD map (a) and the corresponding pole figures (b), with points coloured

according to the local misorientation angle with respect to the ideal {001}<100> orientation, as shown in the legend of Figure 17(c). In addition, grain boundaries above 2° and 10° are shown in Figure 17 a (thin lines = above 2°, and thick lines = above 10°). Kikuchi patterns were well indexed using the Ni Fm-3m cubic phase. The Invar 36 substrate shows a rather sharp {001}<100> texture, with 92.2% of points oriented within 12°. A minor contribution due to cubic twins is visible in the pole figures as scattered poles well indexed as {221}<122>. Although there is room for improvement, the microstructure of the Invar 36 substrate already looks suitable for the development of 11 based CC. In fact, the microstructure of the Invar 36 substrate is well connected with a threshold angle of 7° (above which the micro-structure becomes unconnected and no percolative path can be found[42]), which is below the critical misorientation angle for 11 (around 9°).

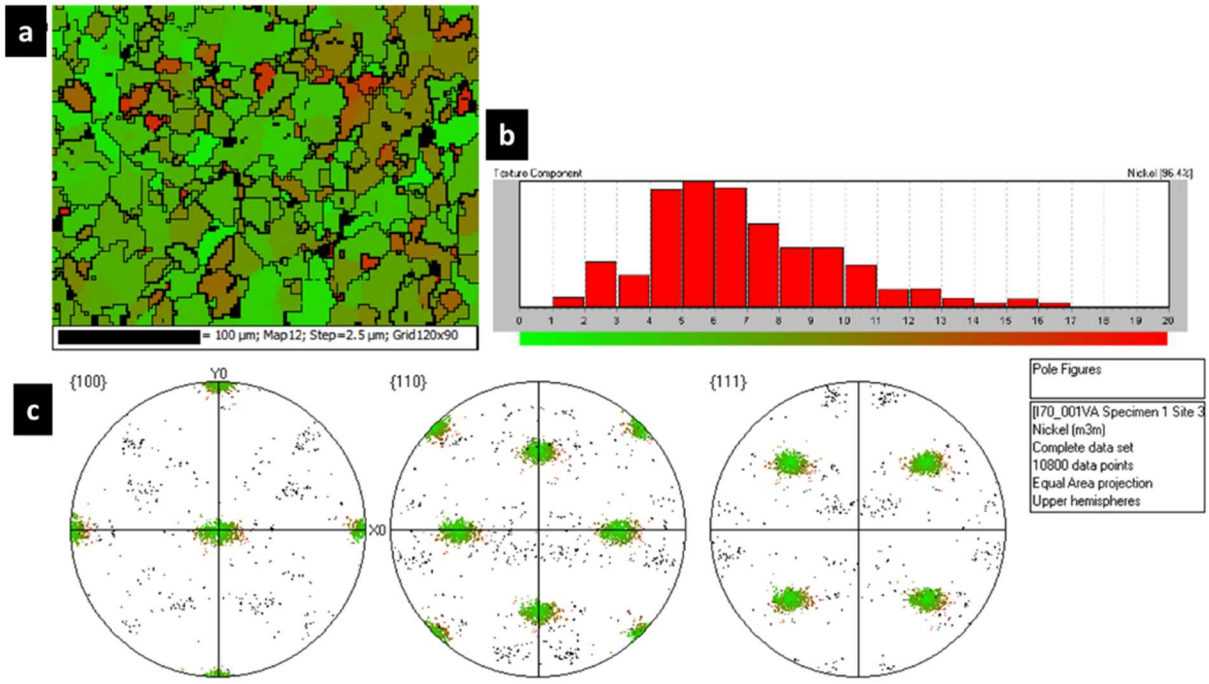

Figure 17: (a) EBSD map and (b) pole figures of the Invar 36 substrate. Kikuchi patterns were indexed using the Ni m3m cubic phase. The rolling direction is aligned vertically. Points are displayed depending on their misorientation with respect to the ideal {001}<100> orientation. The legend (c) shows the distribution of the acquired points with 1° class width as a function of the misorientation angle from 0° (green) to 20° (red). Points unindexed or above 20° are black. GB above 2° (thin line) and 10° (thick line) are included in the map.

With the aim to produce smooth substrates the mechanical polishing was employed, and the surface roughness of the samples was investigated by Atomic Force Microscopy (AFM) and Scanning Electron Microscope (SEM). Left panel of Figure 18 shows a typical optical image at 20X of the surface of a 70 µm thick tape after heat treatment and after a short chemical etching with Marble's reagent, where the grains are evident. On the right is shown the surface of the same sample as it appears at SEM tilted by 72° to better evaluate the surface roughness.

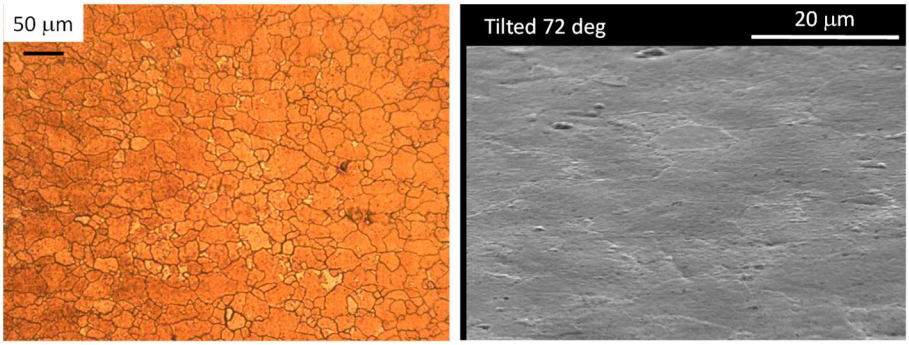

Figure 18: Optical image at 20 X of the surface of a 70 µm thick tape after heat treatment (left), and SEM image of the same tape tilted of 72° (right)

Mechanical polishing was employed with VibroMet™ using alumina nano-powders (30 nm) suspension in ethanol performed before or after the heat treatment, and the surface was analysed by AFM (Figure 19). Over areas of about 20 μm^2 the morphological roughness (root mean square, rms) is about 30 nm in all cases, even if one can observe more topographical irregularities (of a few hundred nm lateral size) when the surface is not polished, or it is polished before heat treatment. The surface turned out smoother when the polishing is performed after the heat treatment, which is confirmed by the smaller value of peak-to-peak height. Profilometer measurements confirmed an average roughness of about 30 nm.

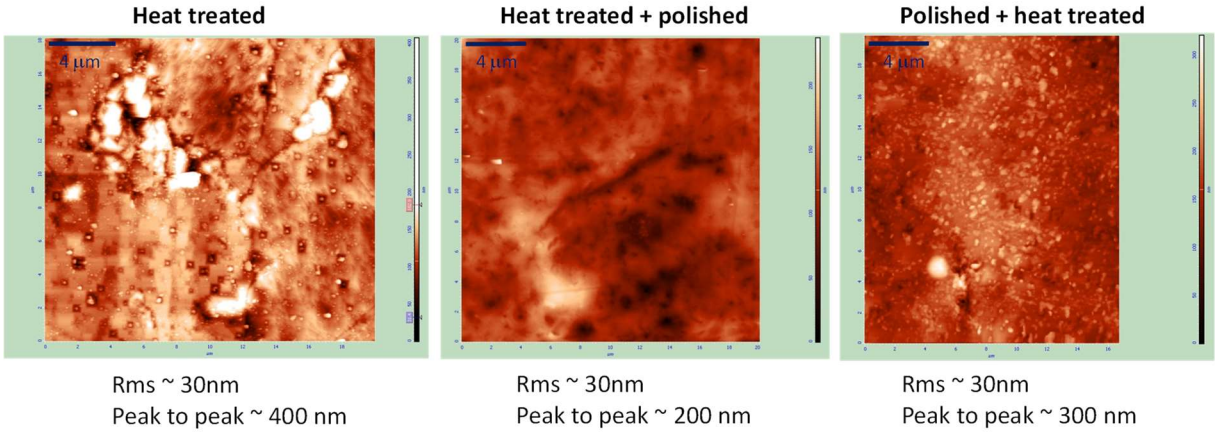

Figure 19: AFM images of the surface of a 70 µm thick tape after heat treatment compared with tapes which underwent mechanical polishing after and before the heat treatment.

B.1.2 11 thin films deposition on Invar substrates

As first step, 11 thin films were deposited on the Invar 36 tape without any buffer layer. To fix correctly the metallic substrate on the support for the PLD deposition we developed a mask that can be fixed to the support with screw (Figure 20). The best results in terms of growth were obtained when depositing the film at 300 °C without seed layer or at 200 °C with a seed layer. In Figure 21 the θ–2θ scan of the 11 film grown at 300 °C (black) is compared with a film deposited at 200 °C on a seed layer (grey). Both samples show c-axis oriented growth which was confirmed by ω scans along the (100) direction of the 11 phase performed in the rolling and transverse directions (Figure 21c, d). Both films show an out-of-plane orientation comparable to that of the substrate, and the seed layer causes a significant

improvement in the out-of-plane orientation of the film: the misalignment angle is reduced by about 1° in both directions (Figure 21 c, d).

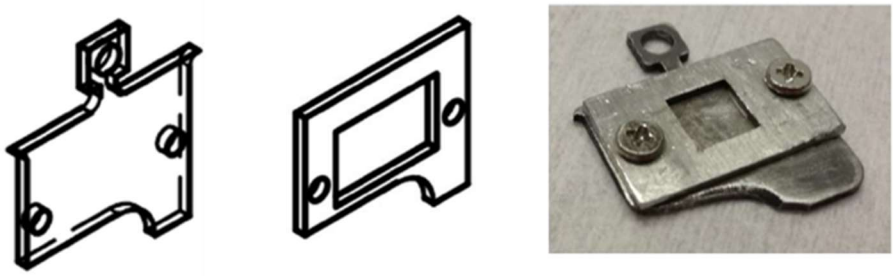

Figure 20: Sample support for PLD deposition, modified for the deposition on metallic substrates.

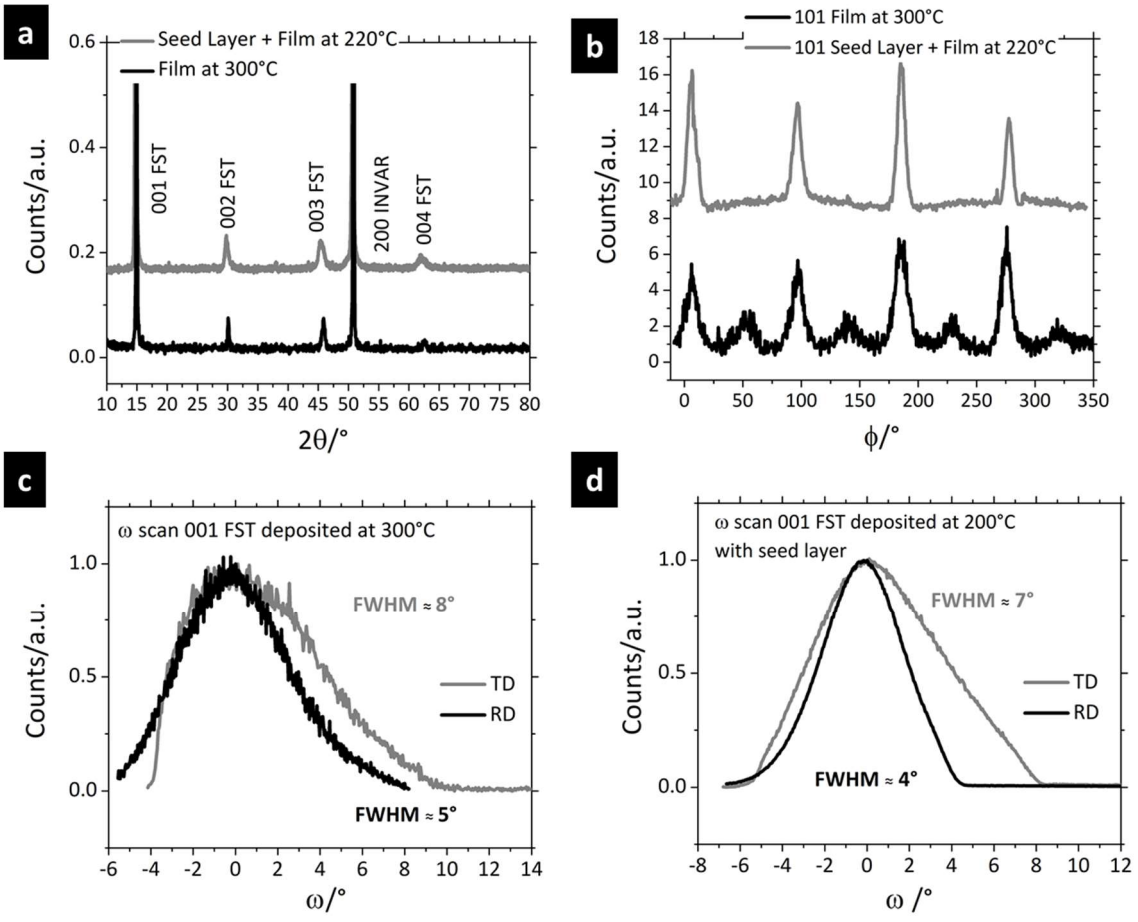

Figure 21: a) XRD θ–2θ scan of 11 thin film on Invar 36 substrate; b) φ scan of the (010) direction of 11 thin films on Invar 36 . c) ω scan along the (100) direction of the 11 thin film deposited at 300°C on Invar 36 measured along the RD and the TD of the tape; d) ω scan along the (100) direction of the 11 thin film deposited at 220°C with seed layer on Invar 36 measured along the RD and the TD of the tape;

The presence of the seed layer improves the in-plane orientation of the film Figure 21 b. Moreover, the film without a seed layer shows a double in-plane orientation, corresponding to two different growth directions of the film: (001)[100] and (001)[110] (Figure 21 b). Conversely the seed layer provides a single in-plane orientation (001)[001], and a reduction in the FWHM of about 2°. Resistivity measurements performed on the film without seed layer and on the film with seed layer revealed that the films are not superconducting (see Figure 22), despite the good degree of alignment demonstrated by XRD analysis.

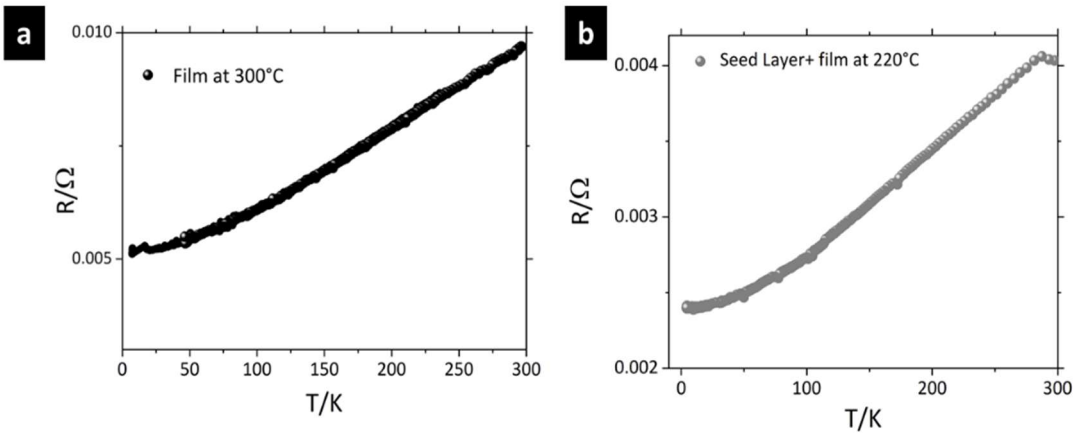

Figure 22: Resistivity measurements of thin films deposited on Invar 36 substrates without seed layer (a) and with seed layer (b).

B.1.3 Chemical incompatibility: The Ni diffusion

To investigate the causes of the lack of superconductivity, a cross-sectional lamella was prepared by focused ion beam (FIB) and analysed by SEM at CERN. The scanning transmission electron microscope (STEM) micrograph in Figure 23 shows the cross-section of the sample. The 11 films have a total thickness of ~450 nm, and it appears that the seed layer and film can be resolved from each other, with an interface ~210 nm above the substrate.

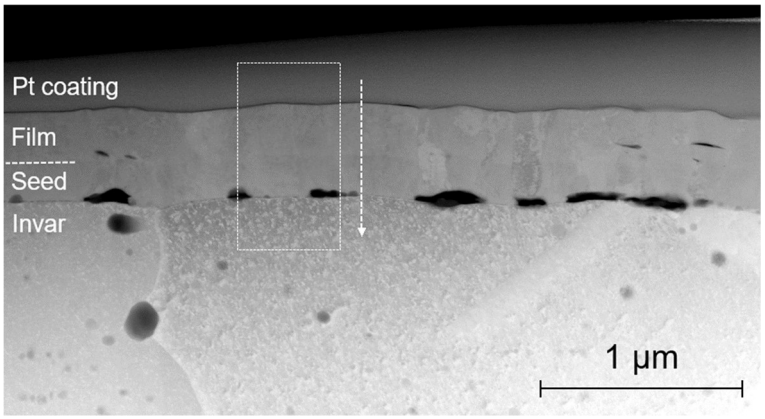

Figure 23: An annotated STEM micrograph (outer high-angle annular dark-field imaging detector) of the coated conductor cross-section showing the substrate, FST films (total thickness ~450 nm) and protective layer. The overlays show the approximate location of the Transmission electron diffraction (TEDS) map (Figure 24) and line scan (Figure 25).

Some microstructural features are continuous across that interface, supporting the observation (by XRD) of epitaxial growth. A significant amount of porosity is evident, but largely concentrated at the interfaces, with larger voids at the substrate surface and smaller ones above the seed layer. TEDS mapping (Figure 24) confirmed the expected distribution of key elements: C and Pt in the protective coating, Se and Te primarily in the films, Ni primarily in the invar substrate, and Fe in both the films and the substrate.

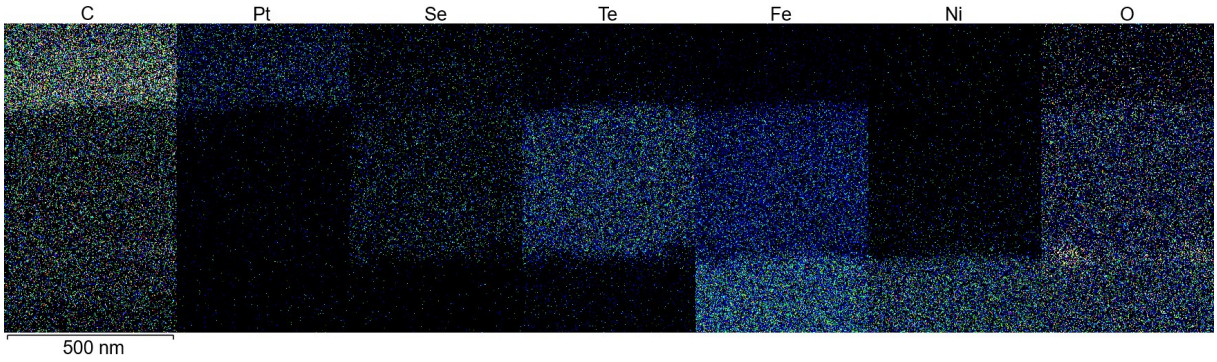

Figure 24: A TEDS map showing the distribution of C (quantified from K series lines), Pt (L), Se (K), Te (L), Fe (K), Ni (K) and O (K). The region corresponds approximately to the dotted box in Figure 23.

O was detected throughout (see Figure 26). For a more detailed analysis, a line scan was performed (Figure 25). The overall distribution is as described above, but it is interesting to note the small peak in oxygen concentration at the film surface and the substrate interface. TEDS map also tentatively suggest that the oxygen concentration peaks at the voids. It is therefore possible that defects are associated with localized surface oxidation. Interpretation of the absolute concentrations is hampered by the inclusion of C and Pt, which are largely artefacts of sample preparation. To clarify the composition of the film, the concentrations in this region were re-normalized to include only the elements present by design, Fe, Ni, Te and Se. The resulting line scan in Figure 26 shows a sharp change of composition at the substrate interface, and a reasonably uniform concentration of Fe, Te and Se throughout the film. However, in the vicinity of the substrate, some Ni is present, and the Fe concentration decreases. Averaging over a larger area, the average composition of the film and seed layer is 49.9 at% Fe, 22 at% Se, 25.6 at% Te and 2.5 at% Ni, close to the intended $FeSe_{0.5}Te_{0.5}$ composition. To verify the compositional uniformity of the film, the data are replotted relative to the average film concentration in Figure 26, after smoothing. Ni clearly shows a diffusional profile through the film, with traces reaching the film surface, but with a change in gradient between the seed layer and the film. In contrast, the Fe concentration is very uniform across the film (note the different scale); within the seed layer, the Fe concentration (and perhaps also Te) decreases to balance the high Ni concentration. The apparent diffusion of nickel into the seed layer and film is the most likely cause of the suppression of superconductivity. A similar phenomenon was also reported for a 11 wire produced by a Powder In Tube (PIT) method using a Ni sheath: in that case the iron of the 11 phase diffused into the Ni sheath, forming particles of a Fe 2at% Ni solid solution and suppressing superconductivity [43]. It should be noted that local defects associated with voids and/or surface oxides may also contribute to this behaviour, for example by locally disrupting the texture. Further investigation is needed to confirm this but given the good macroscopic texture in the film (which grows epitaxially on the seed layer) and the larger defects at the substrate, it is believed this is a secondary effect. STEM analysis underlines the

fundamental role of a buffer layer. Although the deposition temperature of the film is quite low compared to the temperature used for the heat treatment of 11 PIT wire or YBCO deposition, and even if the 11 is deposited in ultra-high vacuum, Ni diffusion and partial oxidation of the substrate appear unavoidable, probably due to the local heating induced by the plasma.

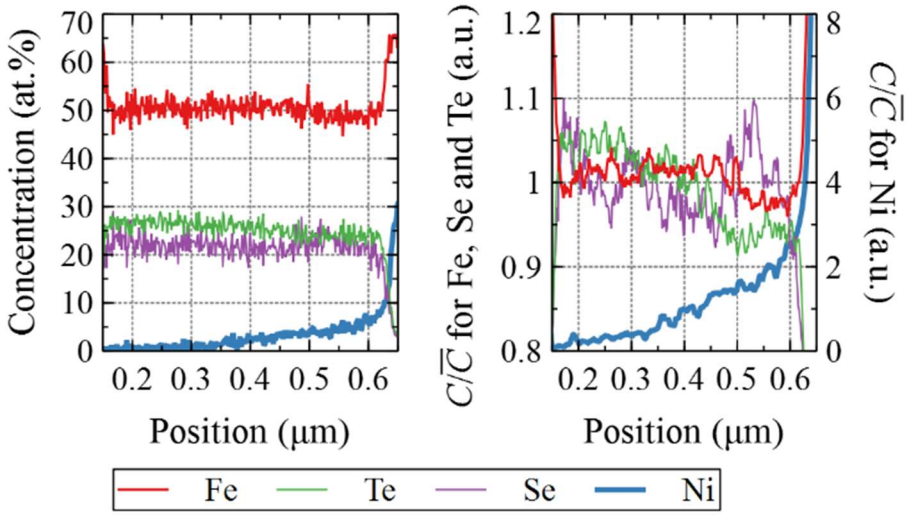

Figure 25: A TEDS line scan showing the composition of all quantified elements as a function of position, from protective coating to substrate. The region corresponds approximately to the line in Figure 24. A TEDS line scan showing the composition of all quantified elements as a function of position, from protective coating to substrate. The region corresponds approximately to the line in Figure 23.

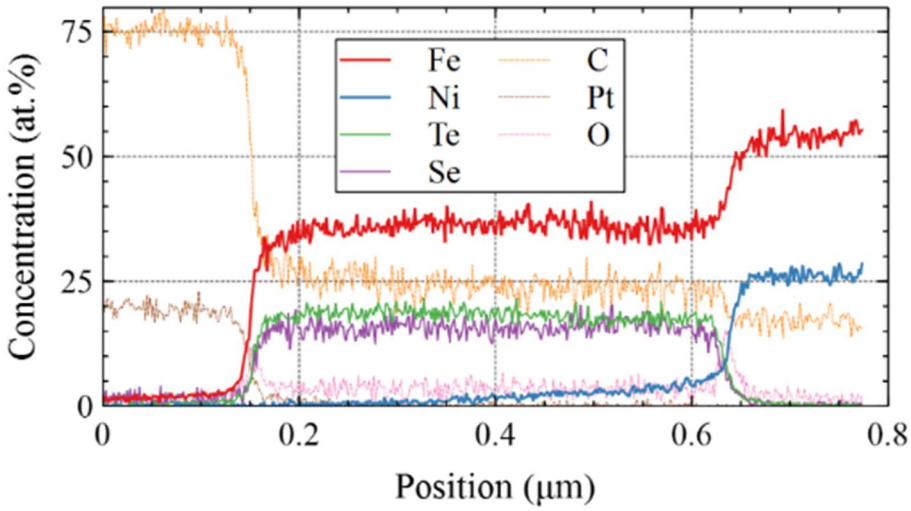

Figure 26: Renormalization of the line scan composition data in Figure 25 to include only the elements present in the FST film, which extends over a position range of approximately 0.16–0.61 μm.

The discovery of the interdiffusion of Nickel from the substrate inside the film made necessary the study of the feasibility of a chemical barrier with a suitable thickness. We started exploiting non-oxides materials as Metals and Nitrates which can be deposited in the same chamber of the FST films in UHV. In the next section the more significative attempts, which were made with Fe, and AlN buffer layers are presented.

B.1.4 Fe-buffered Invar substrate

A possible chemical barrier to Nickel diffusion could be a thin film of Iron, which is chemically compatible with the FST phase, deposited with PLD before the deposition of the superconducting thin film. Following the same procedure descripted in the paper of Iida et al [44] to optimize the deposition of Fe buffer layer an MgO (100) single crystal substrate was used. Single crystalline MgO (100) substrates were heated to 1000 °C inside the PLD, held at this temperature for 30 min, and subsequently cooled to room temperature for cleaning. After the Fe deposition at room temperature, the Fe-covered MgO was heated to 750 °C, held at this temperature for 20 min, and subsequently cooled. The XRD analysis of the Fe buffer layer on MgO is shown in Figure 27.

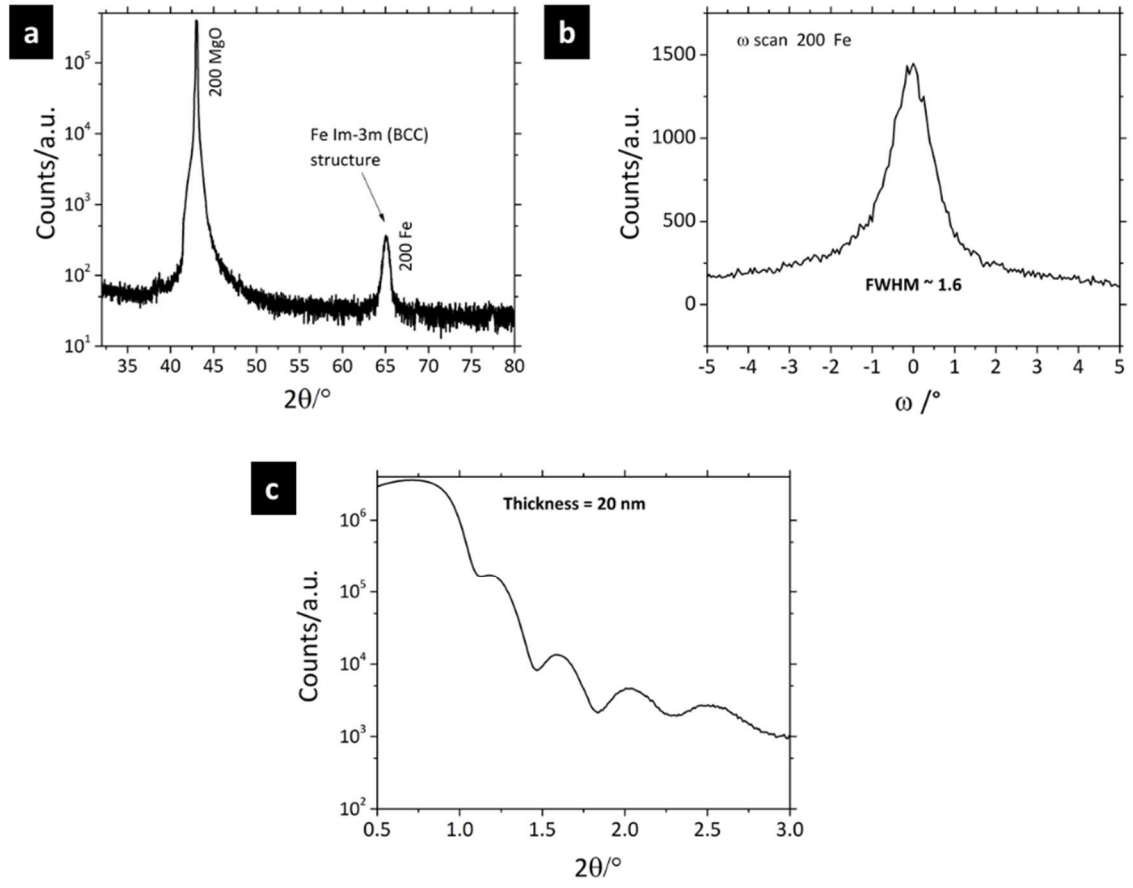

Figure 27: XRD analysis of the Fe buffer layer deposited on MgO (001) single crystal substrate. a) θ-2θscan; b) Rocking curve of the peak 200 of Fe;c)Reflectance measurement from which is possible to obtain information about the thickness of the film from the relation : D=λ/2Δθ where D is the thickness of the film, λ is the wavelength of the XRD radiation, in our case the Kα of Cu, and Δθ is the mean of the difference between the position in angle of two maximum or minimum.

From the θ-2θ scan (Figure 27a) emerges that the Fe thin film is grown on the MgO substrate with a body centered cubic structure (Im-3m): this result is in in contrast with the result shown in the paper[44], where the Fe thin films shows a structure Pbcm. However, the film, which is about 20 nm thick (Figure 27c), grows *c*-oriented on the substrate and shows an out-of-plane orientation of about 1.6° (Figure 27b).

The possibility to deposit the superconducting phase on Iron was also verified using MgO substrate. In Figure 28 we report XRD analysis and R(T) measurements performed on a FST thin film 120 nm thick, deposited on Fe buffered MgO, with the 'standard' condition previously described. As can be seen the FST thin film is grown with highly marked out of plane orientation, and it has superconducting transition with T_c onset at about 18 K.

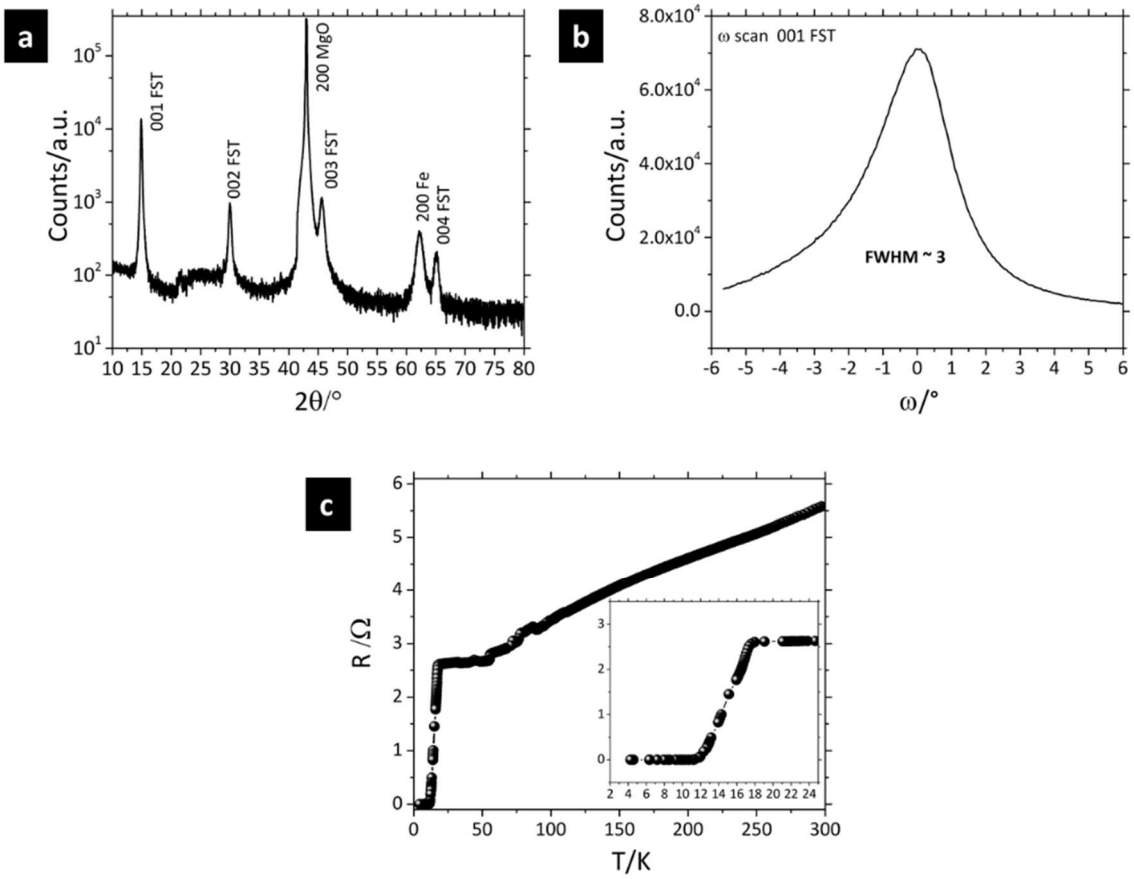

Figure 28: XRD analysis and R(T) of FST thin film deposited on Fe-buffered MgO (001) substrate: a)θ-2θ scan; b)Rocking curve of the 001 peak of the FST; c) Resistance of the FST thin film.

The same procedure used on MgO was done using Invar substrate (see Figure 29): as can be seen from θ-2θ analysis (Figure 29a) the peak of the Fe cannot be seen, either because Fe does not grow on Invar or because it grows with a structure similar to Invar, and in this case the peaks in the XRD scan could be overlapped. However, the FST thin films grew c-oriented showing an out of plane orientation FWHM 8°(Figure 29b). Unfortunately, the FST film does not show superconducting transition, either because the Fe buffer layer cannot stop the Nickel diffusion or because the presence of extra Iron could over doped the FST causing the lack if the superconductivity

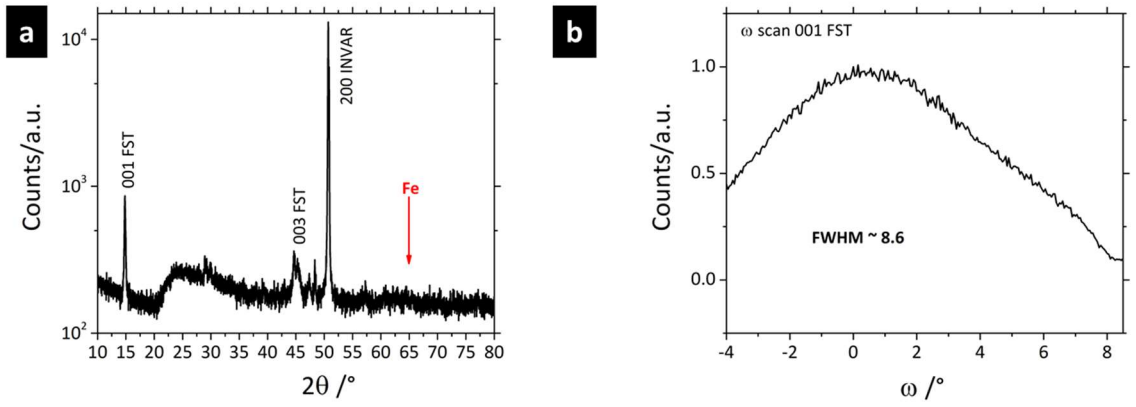

Figure 29: XRD analysis of a FST thin film 120 nm thick deposited on Fe-buffered Invar substrate: a)θ-2θ scan; b)Rocking curve of the 001 peak of the FST.

B.1.5 Nitride buffer layer on Invar substrates

A chemical barrier to block Ni diffusion can also be provided by nitrides, which have the advantage to be deposited in a vacuum system. The first attempts were made with an AlN buffer layer 80 nm thick, which is deposited by sputtering on Invar 36 at CNR-SPIN Naples. FST thin films were deposited, without and with FST seed layer on the AlN buffered Invar substrate. In Figure 30 we report the analysis of two FST thin films, 200 nm thick, deposited on Invar 36 with an AlN buffer layer of 80 nm.

The superconducting phase grows c-oriented on the substrate in both cases (see Figure 30a), while the out-of-plane orientation shows a FWHM in the RD in the ω-scan of 8° without and 7° with the seed layer (Figure 30b). Regarding R(T), the film without seed layer was not superconductor, while with the seed the resistance of the film showed an onset of superconducting transition at about 10 K, and it was near to zero at 4.2 K (see Figure 30c and d). The results are promising, and an optimization of this template will be done. Moreover, these results strongly confirm that a chemical barrier to Ni diffusion is necessary to guarantee the superconductivity.

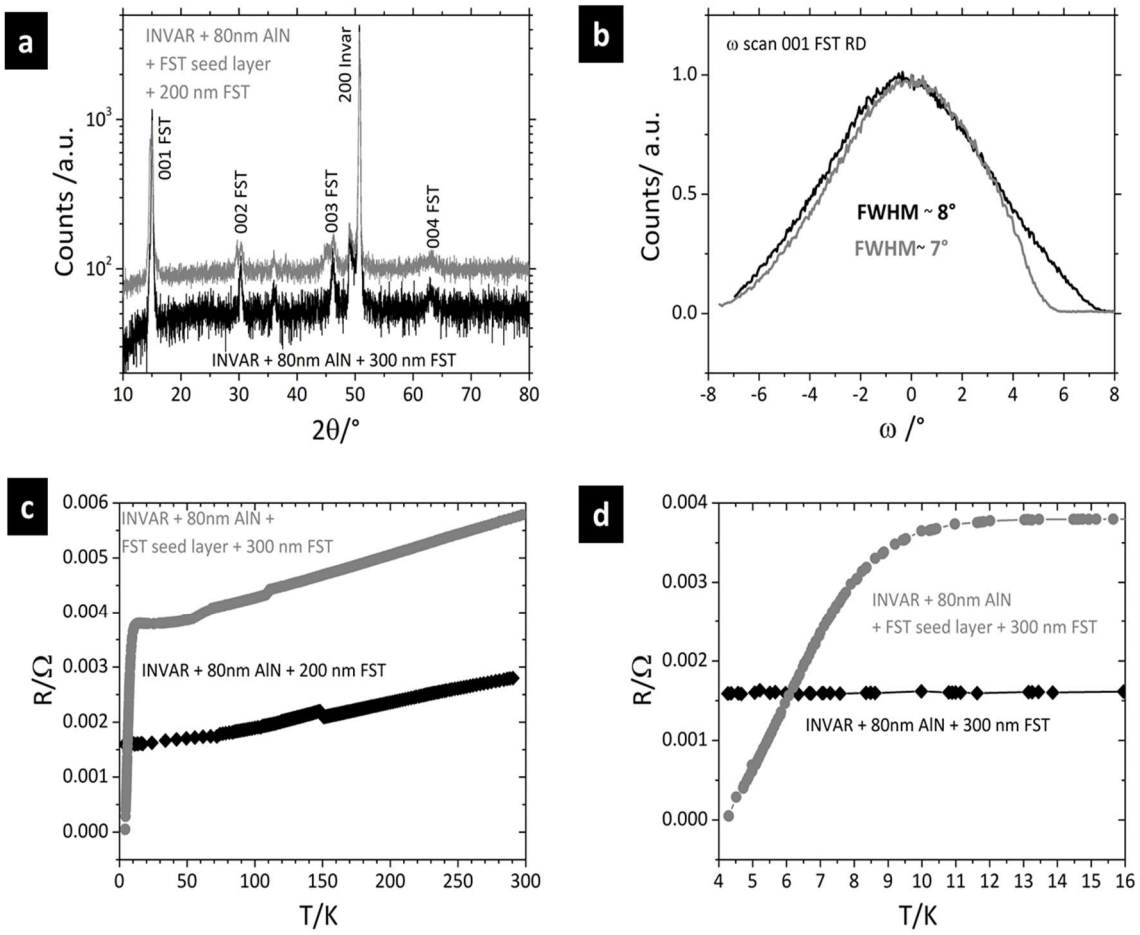

Figure 30: 200 nm 11 thin films deposited on Invar substrate on 80 nm AlN buffer layer without (black line) and with (grey line) FST seed layer. a) XRD θ–2θ scan; b) ω scan along the (001) direction of the 11 thin film measured along the Rolling Direction of the tape; c) Resistivity vs temperature; d) enlargement of the transition near Tc.

B.2 HASTELLOY C276 SUBSTRATES

B.2.1 Hastelloy substrates development

The work performed on Hastelloy C276 alloy as a substrate, is based on the idea to use as a chemical barrier the native passivating Chromium oxide layer of the alloy instead of a buffer layer. This new concept is very interesting because, it could be a real opportunity to avoid the deposition of a buffer layer, operation that inevitably complicates the production of the CC.

HASTELLOY® C276 is a solid-solution strengthened, nickel-molybdenum-chromium alloy with a small amount of tungsten, which exhibits excellent corrosion resistance in harsh environments. C276 is known as the most universally corrosion resistant material available today. It is used in a variety of environments and for a variety of applications. Table 3 reports the chemical composition of the alloy.

The Hastelloy C276 is usually used as substrates for CC, in the IBAD template, where the metallic tape is not textured and the texture which is necessary for the epitaxial growth of the film is provided by

the IBAD deposition of oxides buffer layer. Conversely our idea is to texture the Hastelloy tape through a combination of mechanical deformation and heat treatment, as done for Invar, and then increase the natural layer of passivating oxide with a heat treatment in oxygen atmosphere. The increased oxide layer can act as a chemical barrier avoiding Nickel diffusion, ensuring good properties to the superconducting thin films. This could be a further simplification of the CC template, the possibility to exploit a natural oxide barrier opens a lot of possibilities, even if the problem of the texturing of the oxide layer must be considered. Hastelloy C276 shows an FCC crystalline structure with a lattice parameters of 3.620 Å and a density of 8.89 g/cm^3 at room temperature [45], the understanding of the deformation behaviour of Hastelloy C276 is quite complex and the information are scarce. Opposed to Invar, the Hastelloy C276 possesses a low SFE, which does not allow the development of the cubic texture after the heat treatment. It is well known that alloys with low SFE subjected to cold rolling develops an alloy texturing which is mainly composed of Brass orientation component $\{110\}\langle 112\rangle$, and a minor Goss orientation $\{110\}\langle 100\rangle$. Mehta et al. [46] in the study of the evolution of crystallographic texture and anisotropy during cold rolling of C276, shows that also a strong component of deformation by twinning is common in this alloy. After recrystallization process, the preferential orientation induced by the cold rolling could be the preferential for the grain nucleation or for a fast growth of the grain ensuring the texturing of the final tape.

Nickel:	57 Balance
Cobalt:	2.5 max.
Chromium:	16
Molybdenum:	16
Iron:	5
Tungsten:	4
Manganese:	1 max.
Vanadium:	0.35 max.
Silicon:	0.08 max.
Carbon:	0.01 max.
Copper:	0.5 max.

Table 3: Nominal composition in weight % of Hastelloy C276 from the data sheet of the Haynes International which holds the trademark of the Hastelloy.

Moreover, the information about the controlled oxidation of Hastelloy are limited, Hasim et al studied the oxidation of Hastelloy C22 and of Inconel showing that alloys have a good tendency to develop a uniform chromium oxide coating but a smaller amounts of spinel oxides were also observed for samples heat treated at higher temperature [47]. On the basis of our previous study performed on Invar 36 and on the basis of some information finds in the cited literature, starting from an Hastelloy C276 wire of 1 mm of diameter we obtain a tape 115 µm thick with cold rolling and reductions of 10% in thickness every step. As can be seen from Figure 31, cold rolling induces in the tape a slight (220) orientation along the c-axis of the sample. After cold deformation we thermally treated the Hastelloy tape to recrystallize it at 900°C in ultra-high vacuum (10^{-6} mbar). After the recrystallization heat treatment, the Hastelloy shows an incremented *c*-axis orientation along the (220) direction as shown in the XRD measurement in Figure 31.

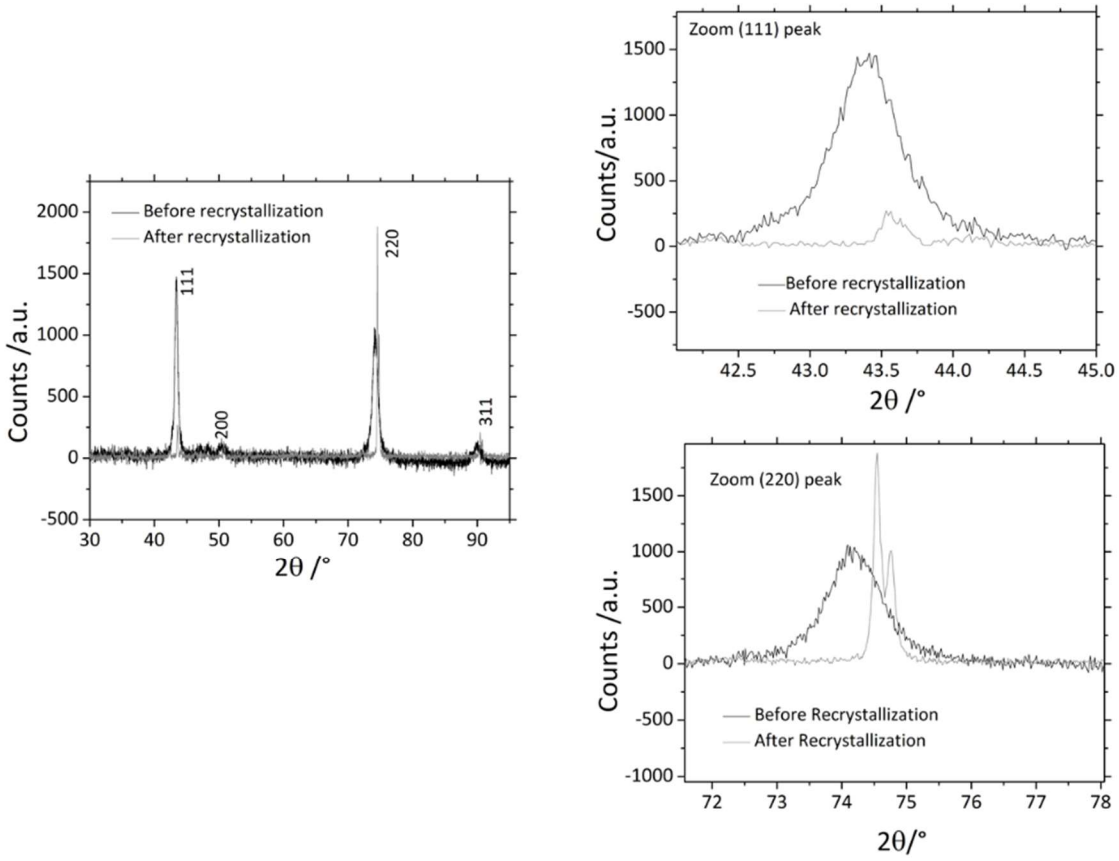

Figure 31: Complete θ-2θ scan of Hastelloy C276 cold rolled tape before and after recrystallization heat treatment and zooms of the peaks (111) and (220)

Nevertheless, the tape does not show neither out of plane and in-plane orientation, therefore it is not biaxial textured as can be seen from the pole figure in Figure 32. The obtained recrystallized tape was heat treated again in oxygen atmosphere. Figure 33 shows the XRD measurements performed on the oxidised Hastelloy substrates compared to the not oxidised tape. As can be seen many peaks of the chromium oxides are present also in the 'not oxidised' sample because of the natural passivating layer and for the oxides sample also crystalline peaks that could belong to a spinel oxide $NiCr_2O_4$ is present, this confirms that the process of oxidation causes the growth of complex oxides which have a randomly

oriented crystalline structure. A cross section analysis of the Hastelloy substrates was performed through SEM, to investigate the thickness of the oxide layer. From Figure 34, it is possible to notice that the not oxidised sample does not show a visible oxide layer (which could be ~10 nm thick) while the oxidised sample shows an oxide layer of about 400 nm.

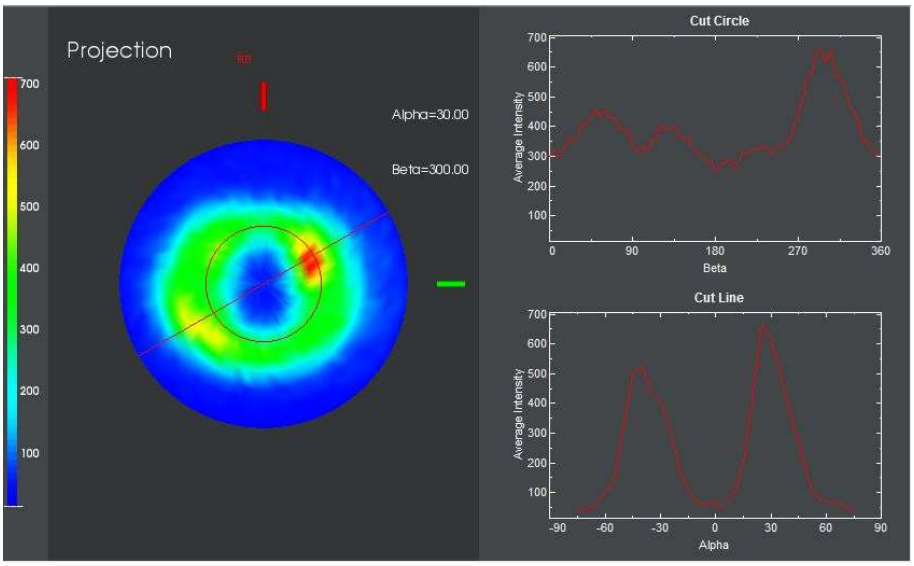

Figure 32: Polar figure of Hastelloy recrystallized tape made at ENEA Frascati.

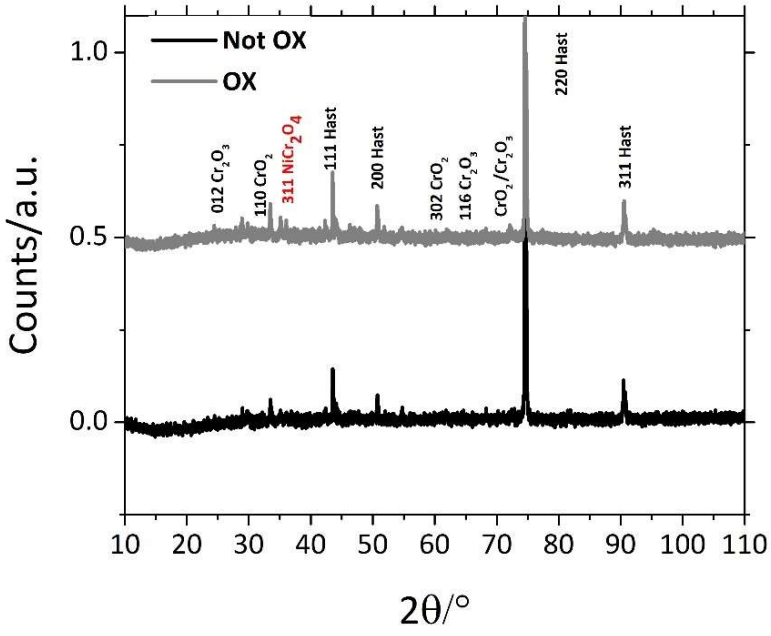

Figure 33: X-ray scans of the Hastelloy C276 substrates before and after oxidation process.

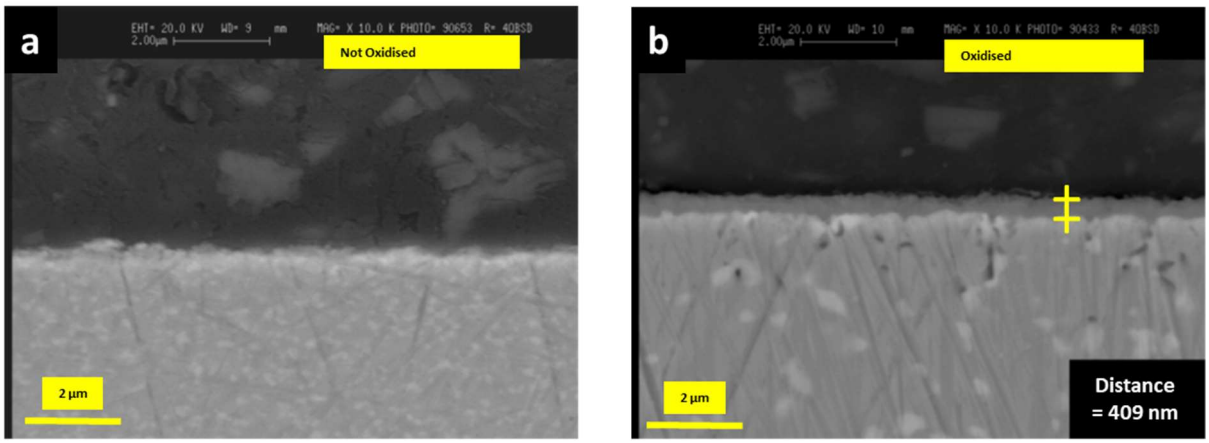

Figure 34: Cross section of Hastelloy substrates not oxidised (a) and oxidised (b).

B.2.2 11 thin films deposition on Hastelloy C276 substrates

The films on Hastelloy substrates were deposited using the same conditions and parameters already mentioned for thin films on Invar 36 using seed layer [48]. Figure 35 shows the θ-2θ performed on two identical films deposited respectively the not oxidised substrate and on the oxidised substrate. As can be seen in both cases the films show an orientation along the c-axis.

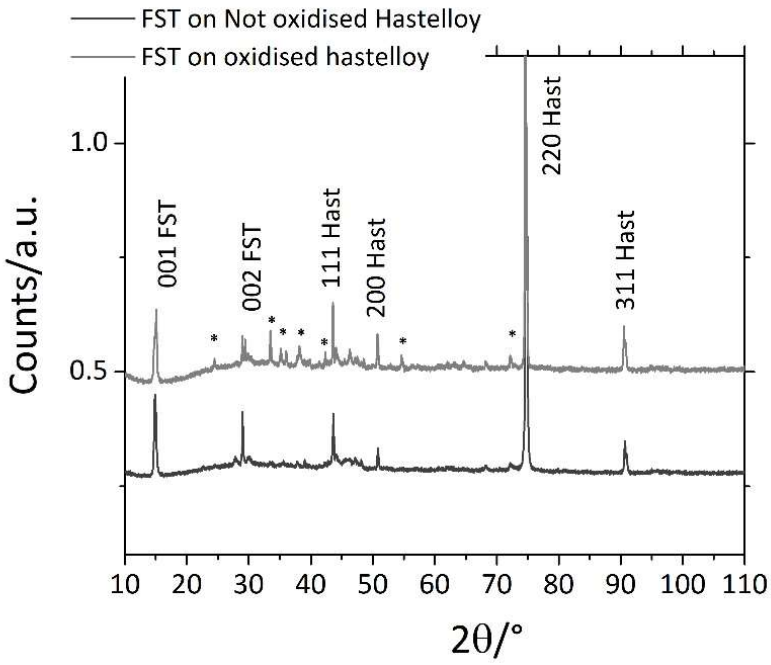

Figure 35: θ-2θ scan of three FST thin films deposited on Hastelloy substrates with and without passivation oxide. Stars indicate the crystalline peaks of oxides.

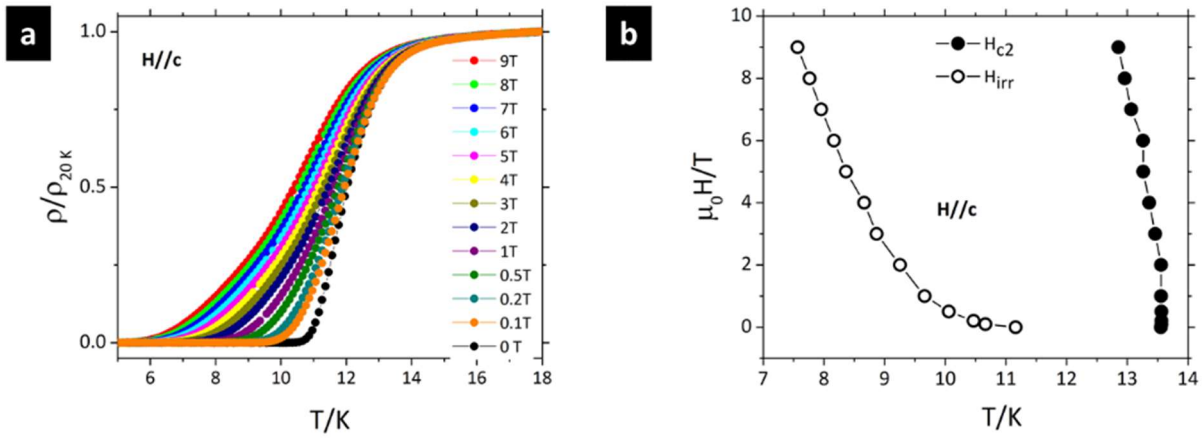

Figure 36: a) Resistivity measurements in applied magnetic field for the FST thin films of Hastelloy substrates with 400 nm of passivating oxide. b) Upper critical field and irreversibility field of FST thin films of Hastelloy substrates with 400 nm of passivating oxide.

From R(T) measurements emerge that only the films deposited on the oxidised samples show a superconducting transition, these results seem to confirm that the oxide layer, 400 nm thick, provides a complete insulation from Nickel diffusion. In detail the film deposited on the oxidised Hastelloy shows an onset of the resistive transition at about 13.5 K and the transition is complete at 11 K (Figure 36 a).The superconducting transition is complete also in applied magnetic field up to 9 T. The resistive measurements in field allow to estimate the upper critical field and the irreversibility field using the criterion of 10% and 90% of the resistivity value in the normal state above transition. As can be seen from Figure 36 b, the upper critical field is very steeper with a ΔT_c of only 0.7 K in 9 T, steeper than the optimized FST thin films grown on CaF_2 single crystals. As can be seen from Figure 37 the sample shows a J_c of about 1.2 10^4 A/cm^2 in self field at 5K (the critical current I_c was estimated using the standard 1μV/cm criterion). The J_c strongly decrease in applied magnetic field, decreasing of one order of magnitude in 1 T. This behaviour suggests a problem related to the passage of the current across the GB. From a comparison between the J_c data reported in fig with J_c data of FST thin films deposited from our group on STO bi-crystal substrates [6], we can conclude that the films deposited on Hastelloy has a significant misalignment between grains. The J_c values at zero field seems to suggest a misalignment higher than 20° (see data in [6]), and the strong decrease of the J_c in field confirms that the misalignment governs the trend of the J_c. The final confirmation of the complete misalignment of the films comes from the polar figure performed at ENEA Frascati and reported in Figure 38. This result is quite important because seems to confirm that a certain degree of in-plane orientation is necessary to obtain good J_c performance of the 11 CC.

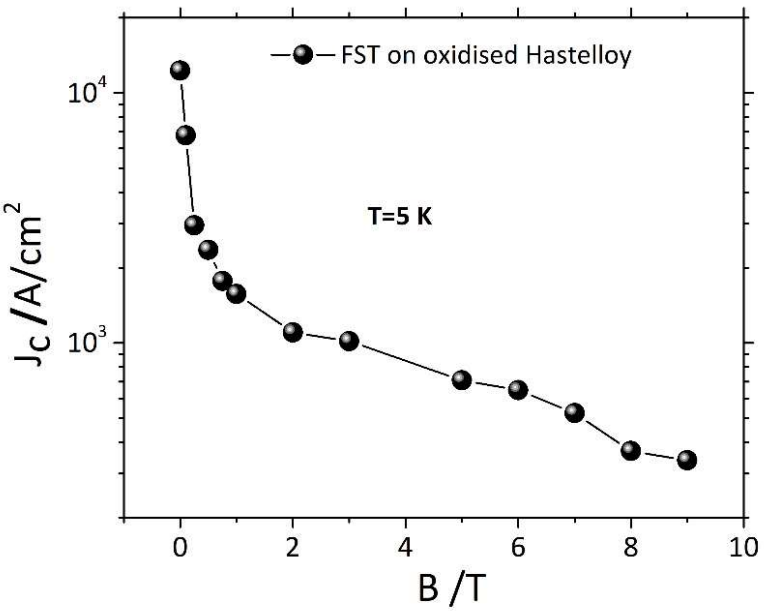

Figure 37: Critical current density at 5 K of the FST thin film deposited on the oxidised Hastelloy substrate.

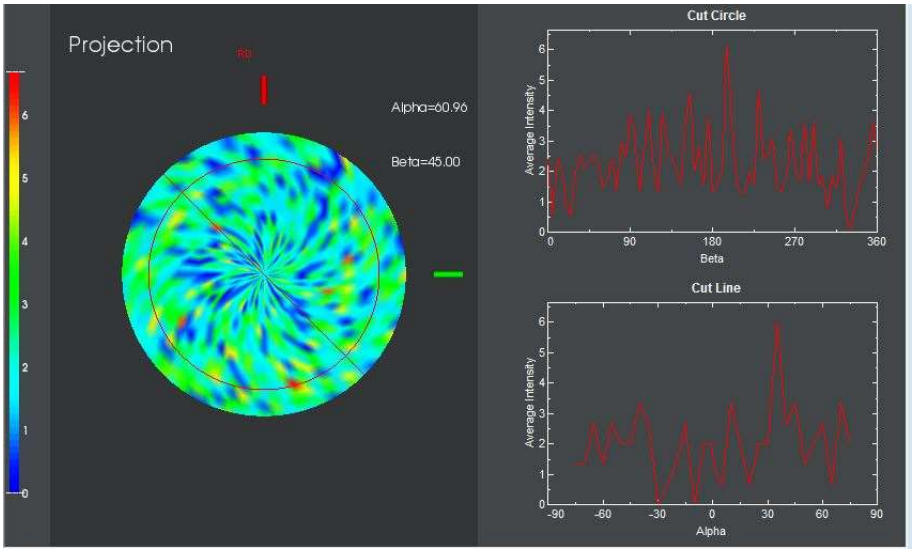

Figure 38: Polar figure of the FST thin film deposited on the most oxidised Hastelloy substrate.

The work on Hastelloy substrate is at the very beginning. For sure the texturing of the substrate must be improved through different cold working procedure and starting from bigger rod to increment the level of deformation. The controlled growth of the passivating oxides must be improved as well, in order to obtain the right thickness for the best film growth, and to study the possibility to obtain an oriented oxide. Even if this work is preliminary, the results obtained seems to be very promising because they confirm the possibility to use commercials metallic alloy as substrate for FST CC without

any buffer layer by exploiting the native passivating oxide. Moreover, the good growth of the film on the oxide which is completely randomly oriented confirms some results find in literature that suggest a sort of self-organized orientation mechanism of the FST phase as thin films[34,35]. For sure this mechanism is not enough to guarantee a J_c relevant for engineering applications and so a better texturing of the substrate is required.

C) ENEA SUBSTRATES

C.1 CeO_2 BUFFERED Ni-W SUBSTRATES

C.1.1 The RABiTS substrate

For the development of 11-CC commercially available cube textured Ni – 5 at.% W (Ni-W) tapes from Evico were used as substrates [49]. On top of Ni-W a CeO_2 film was deposited as a buffer layer, through PLD technique using the 266 nm emission of a Nd:YAG solid state laser at ENEA-Frascati. The datils about the preparation of the buffer layer can be found in [50].

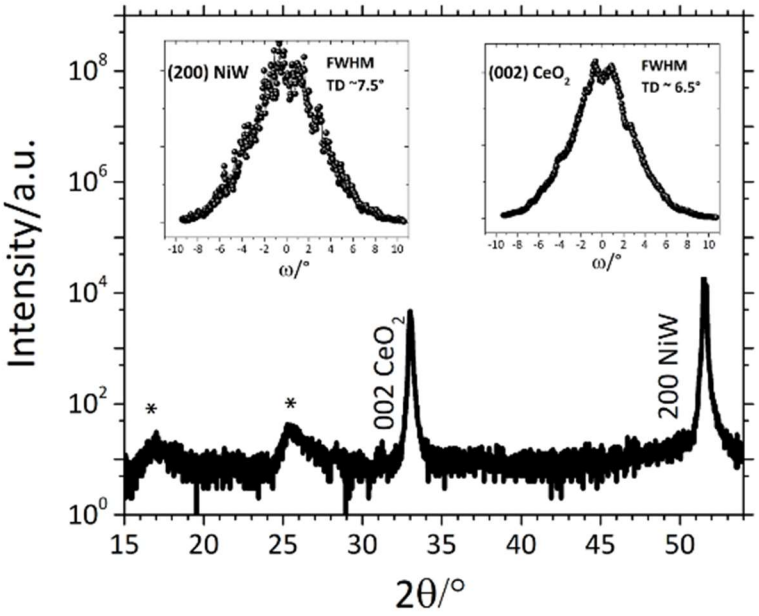

Figure 39: θ-2θ scan of CeO_2/Ni-W buffer layer structure. In the insets, the (002) CeO_2 and (002) Ni-W rocking curves in the Transverse Directions (TD) with respect to the deformation. Stars mark θ/2 features due to the CeO_2 film and the substrate caused by the secondary monochromator.

In Figure 39 the XRD analysis for a CeO_2 buffer layer grown on Ni-W is reported. The intense (002) CeO_2 peak, the only reflection related to the film, indicates that the buffer layer develops a single orientation with the (001) direction perpendicular to the substrate. Even if a major part of the deposition process occurs in oxygen atmosphere, peaks related to the substrate oxidation are not detectable. In the insets,

we report the ω-scans in the TD with respect to the deformation process which is the less favourable direction through the (002) Ni-W and CeO_2 peaks. The FWHM are 7.5° and 6.5° respectively for the Ni-W and the CeO_2 confirming, as previously reported, that CeO_2 films are prone to improve the out-of-plane substrate texture [51]. The CeO_2 film texture analysed by pole figures in Figure 40 reveals the in-plane epitaxial relationship: [100] Ni-W// [110] CeO_2. The FWHM value of the φ-scan across the (111) CeO_2 poles lie between 5.0° and 6.2°, similarly to those measured across the (111) Ni-W poles of the substrate which are between 5.2° and 6.7° as it will be reported later.

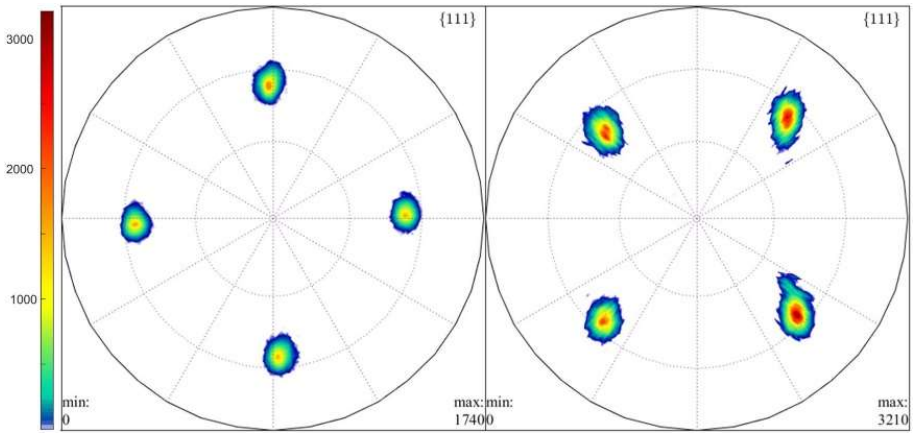

Figure 40: Pole figure along (111) direction of CeO2 (left) and of Ni-W (right)

Figure 41 shows SEM images of a CeO_2/Ni-W buffer layer surface after the annealing process in a temperature range relevant for 11 film deposition (> 300 °C). The structural and morphological properties of the CeO_2 film are unchanged after the annealing: in particular, the surface is uniform, smooth and dense. Above all, the CeO_2 film assures a good coverage of the grooves among the substrate grain boundaries. This result shows that CeO_2 film on Ni-W is a robust template suitable for the 11 film deposition.

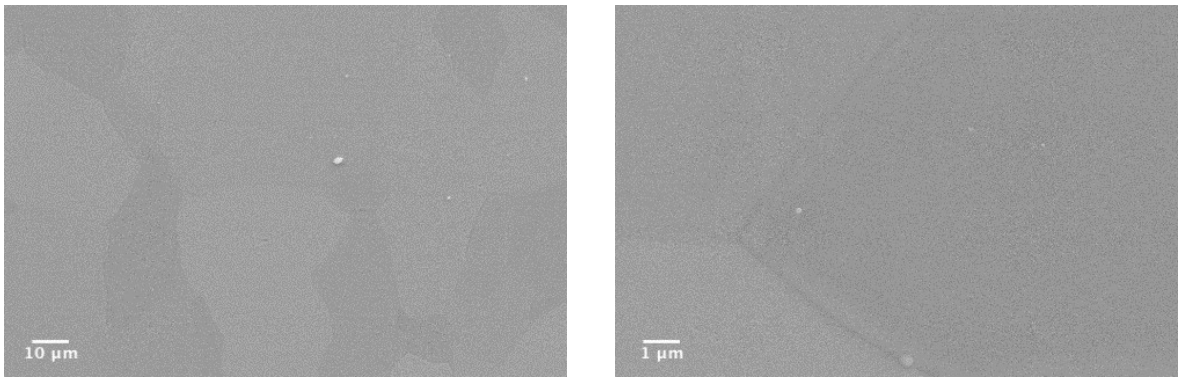

Figure 41: SEM images of the CeO_2 film grown on Ni-W after the annealing process in FST deposition relevant conditions at two different enlargements.

C.1.2 11 thin films deposition on CeO_2 buffered Ni-W substrates

Figure 42 reports a θ-2θ scan of the FST thin film deposited on the CeO_2/Ni-W template. Besides the (00l) peaks corresponding to the 11 phase, the peaks coming from the template are clearly visible, but no other peaks are present relative to other orientations or phases, indicating an optimum *c*-axis alignment of the growth and a high purity of the phase. The ω-scan on the (002) peak, reported in the inset of Figure 42, shows a FWHM value Δω of about 6.6° measured in the Transverse Direction, which is compatible with the value measured in the CeO_2 buffer layer (see inset of Figure 39) and confirms a good out-of-plane texture.

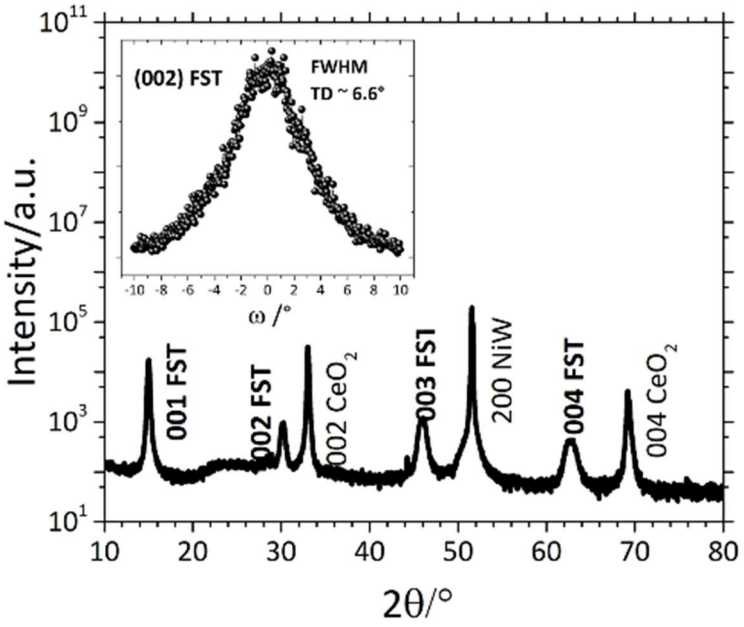

Figure 42: θ-2θ scan of the coated conductor with highlighted the (00l) peaks of template and FST film. The inset shows, the rocking curve of the (002) peak of the 11 thin film in the Transverse Direction.

In order to establish the in-plane epitaxy of the growth, we performed *φ* scans of the (101) reflections of the 11 film. In Figure 43a), we show the polar figures of a FST thin film along the (101) and the (111) direction, while Figure 43b) reports the *φ* scans of the (101) peak from the thin film compared with those of the (111) peak of the CeO_2 and the Ni-W substrate. The lattice of the 11 thin film is therefore aligned cube-on-cube with the Ni-W substrate and rotated by 45° in the *ab* plane compared that of the CeO_2 buffer layer. 11 thin films grown on CaF_2 single crystals and on RABiTS templates show the same behaviour [5,36]. In fact, the diagonal of the lattice parameter of CeO_2 (and CaF_2) is about 3.82 Å (~ 5.41/√2), which matches exactly with the *a* lattice parameter of FST. The average in-plane FWHM $\Delta\varphi_{FST}$ is about 4.9°, comparable with $\Delta\varphi_{CeO2}$ which is about 4.7°. Therefore, we can conclude that the 11 thin films grown on CeO_2/Ni-W templates possess a good biaxial texturing determined by the texturing of the CeO_2 buffer layer. Such results are consistent with the data reported in literature on IBAD templates [31] and RABiTS with CeO_2/YSZ/Y_2O_3 buffer layer [52].

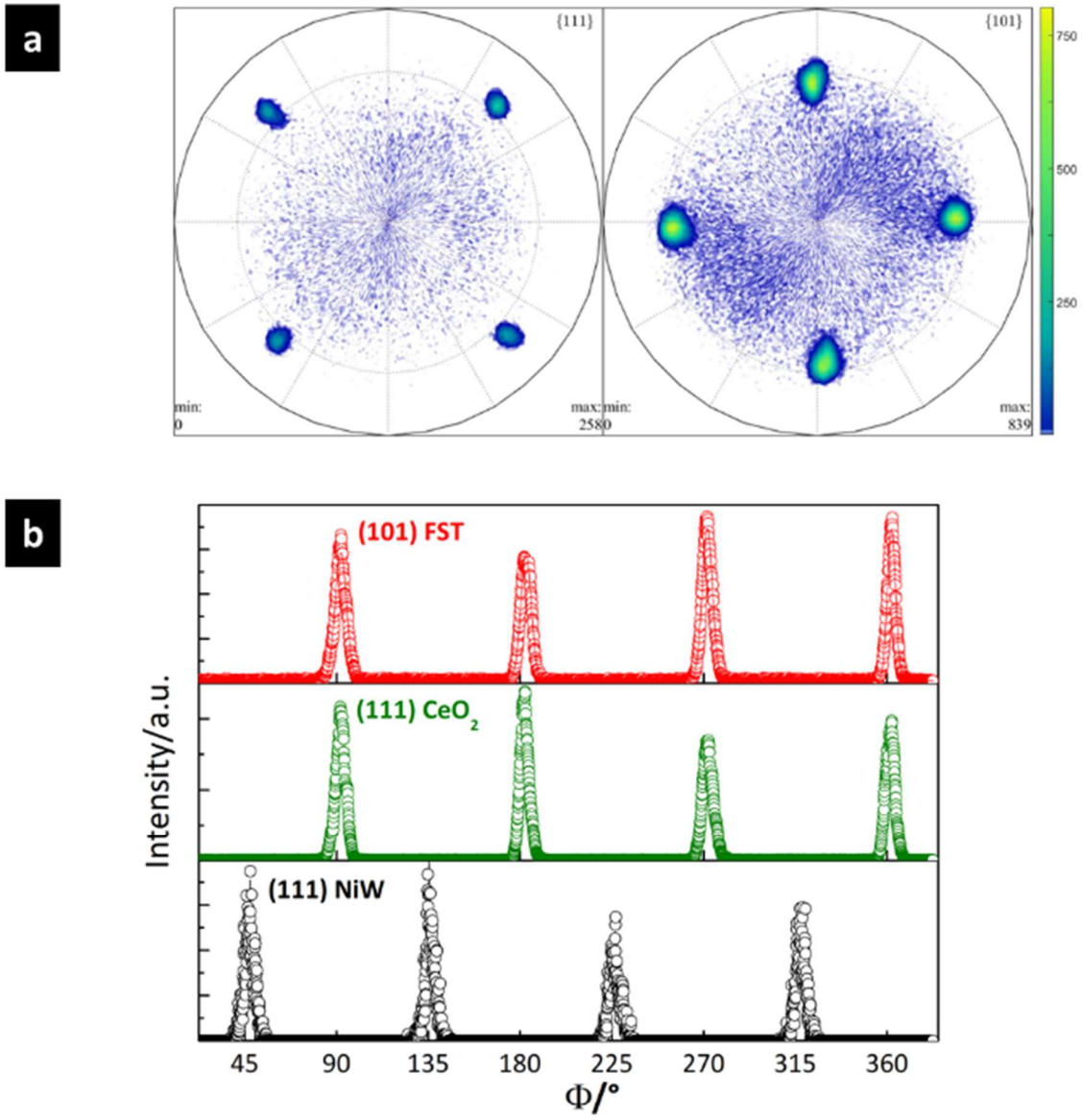

Figure 43: a) Polar figures of 11 thin film made along the (111) direction (left) and along the (101) direction (right); b) from top to bottom: ϕ scans of the (101) peak of the FST with FWHM = 4.9°, of the (111) peaks of CeO_2 with FWHM = 4.7° and of the (111) peak of Ni-W with FWHM = 5.3°.

Figure 44 reports the surface of a patterned FST thin film grown on CeO_2-buffered Ni-W substrate. The surface is uniform and shows an irregular hill-and-valley morphology. Average and rms roughness on 1 μm^2 area are 0.7 nm and 0.9 nm, respectively, slightly larger than what observed for CeO_2 films (0.4 and 0.5 nm, for average and rms roughness, respectively). In order to evaluate correctly the thickness of the 11 film, the cross section of the fractured sample was analysed with SEM: as shown in Figure 45, the thickness of the film is about 100 nm. Both the CeO_2 and 11 films appear compact and continuous

along the whole thickness suggesting very high-density layers. No interdiffusion process are detectable at the FST/CeO_2 interface. The FST film shows some longitudinal features that suggest a layered growth mechanism. The microstructure of the 11 film was investigated by means of EBSD technique.

Figure 46 shows the EBSD map (a) and the corresponding pole figures (b) of a FST film grown on CeO_2/Ni-W template. In both EBSD map and pole figures, points are displayed according to the local misorientation angle with respect to the ideal {001}<010> orientation, Kikuchi patterns were well fitted using the P4/mmm tetragonal phase and no hexagonal component was detected. As can be seen, the 11 film shows a sharp {001}<010> texture, with a fraction of oriented points of 98.9% within 10°.

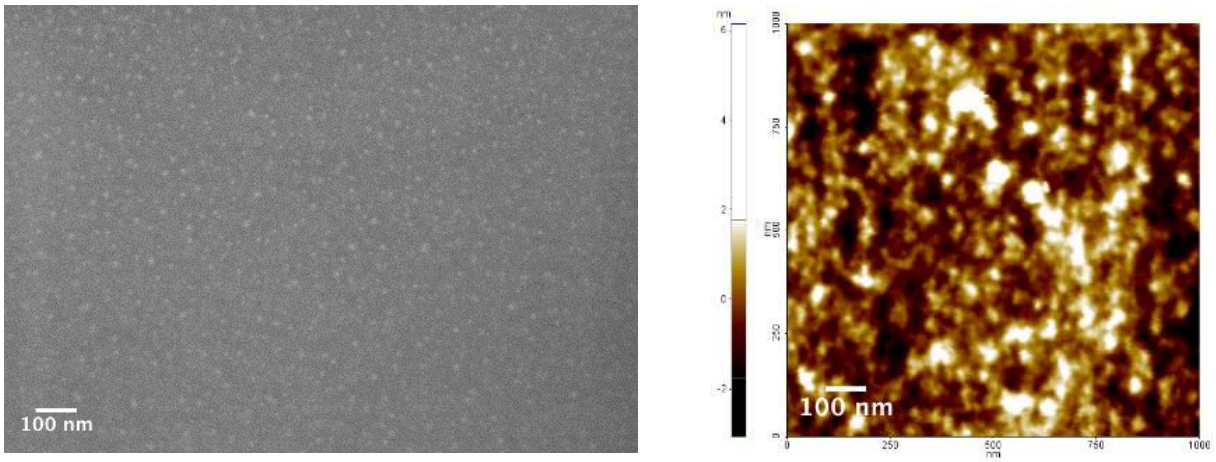

Figure 44: SEM and AFM images of a patterned 11 film grown on CeO_2-buffered Ni-W substrate

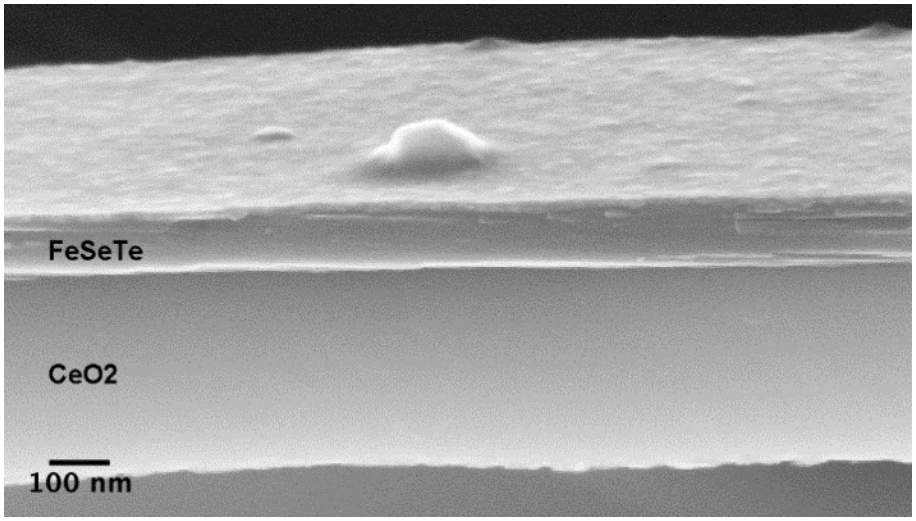

Figure 45: Cross section of the CC analysed with SEM.

The film reproduces the microstructure of the underlying Ni-W substrate, as typically observed in RABiTS-based coated conductors [52]. In fact, the film shows a relative misorientation below 2° in regions of 35 ± 15 µm, which is the typical grain size of Ni-W RABiT substrate [22,36,52]. As can be seen, most grain boundaries are below 10°. The microstructure is well connected, with the presence of several low-angle grain boundary percolation paths. The critical angle for the existence of a percolative path across the sampled area is 4.5°. This is in line with the value obtained in the case of YBCO films grown on a similar template [53].

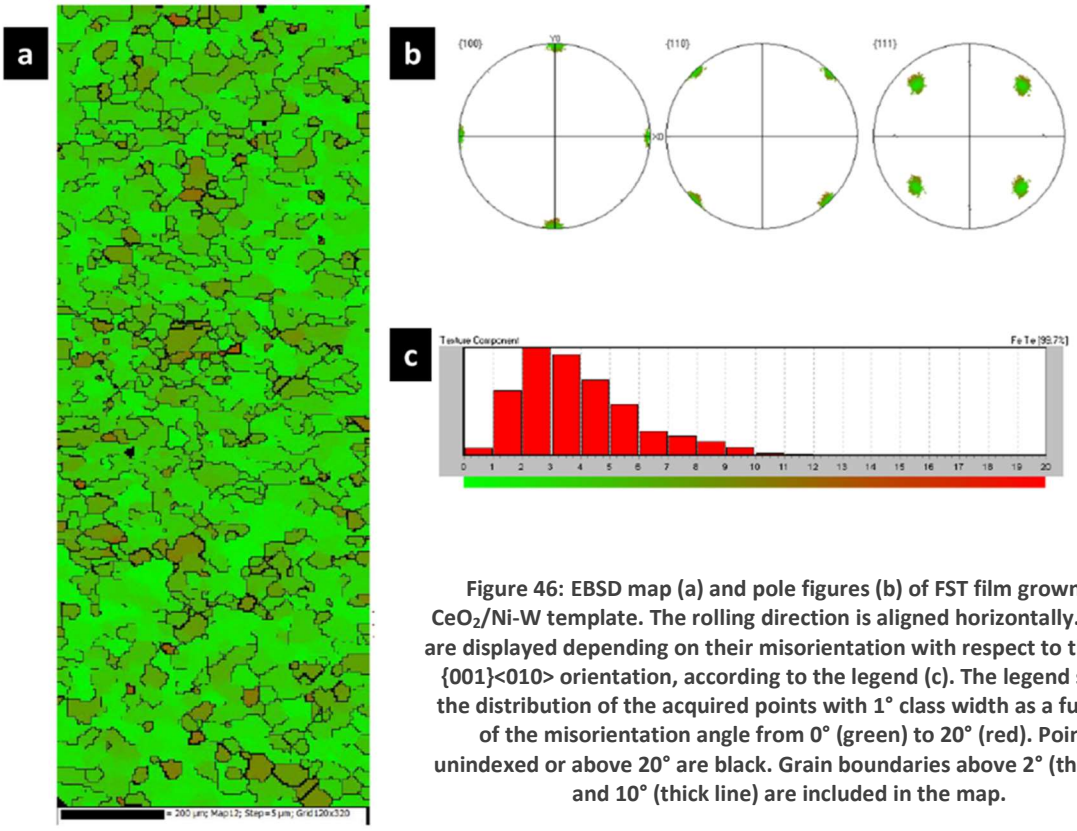

Figure 46: EBSD map (a) and pole figures (b) of FST film grown on CeO_2/Ni-W template. The rolling direction is aligned horizontally. Points are displayed depending on their misorientation with respect to the ideal {001}<010> orientation, according to the legend (c). The legend shows the distribution of the acquired points with 1° class width as a function of the misorientation angle from 0° (green) to 20° (red). Points unindexed or above 20° are black. Grain boundaries above 2° (thin line) and 10° (thick line) are included in the map.

The underlying CeO_2 buffer layer shows the same microstructure observed in the FST thin film. Figure 47 reports the EBSD map (a) and the corresponding pole figures (b) of the CeO_2 film analysed outside the patterned strip used for transport measurements. As can be seen, the CeO_2 film shows a strong {001}<110> texture, with a fraction of oriented points of 99.2% within 10°. From EBSD microstructural investigation, it is possible to conclude that an epitaxial relationship (001)[010] FST // (001)[110] CeO_2 // (001)[100] Ni-W has been obtained. In Figure 48 the temperature dependence of the normalized resistivity of the 11-CC up to 18 T in the two directions is reported, perpendicular and parallel to the film plane. $T_{c,0}$ is about 16 K with an onset above 18 K, comparable with thin films on single crystals or on technological templates [15].

All the plotted ρ(*T*) curves show low normal state resistivity values and an anomalous bump before the transition with a sharp increase in ρ followed by a steep reduction and then eventually reaching the

zero-resistance state. The maximum of the bump, T_m, shifts towards lower temperatures coherently with T_c as the applied magnetic field is increased. However, the presence of such a bump was not observed in un-patterned films grown on the same template studied in the present work. The normal state temperature dependence of the resistivity exhibited by iron chalcogenides is, in general, not trivial. Semiconductor behaviour up to room temperature has been reported in both bulk and films, while a gradual crossover to metallic behaviour is usually observed for temperature approaching the superconducting transition [54,55].

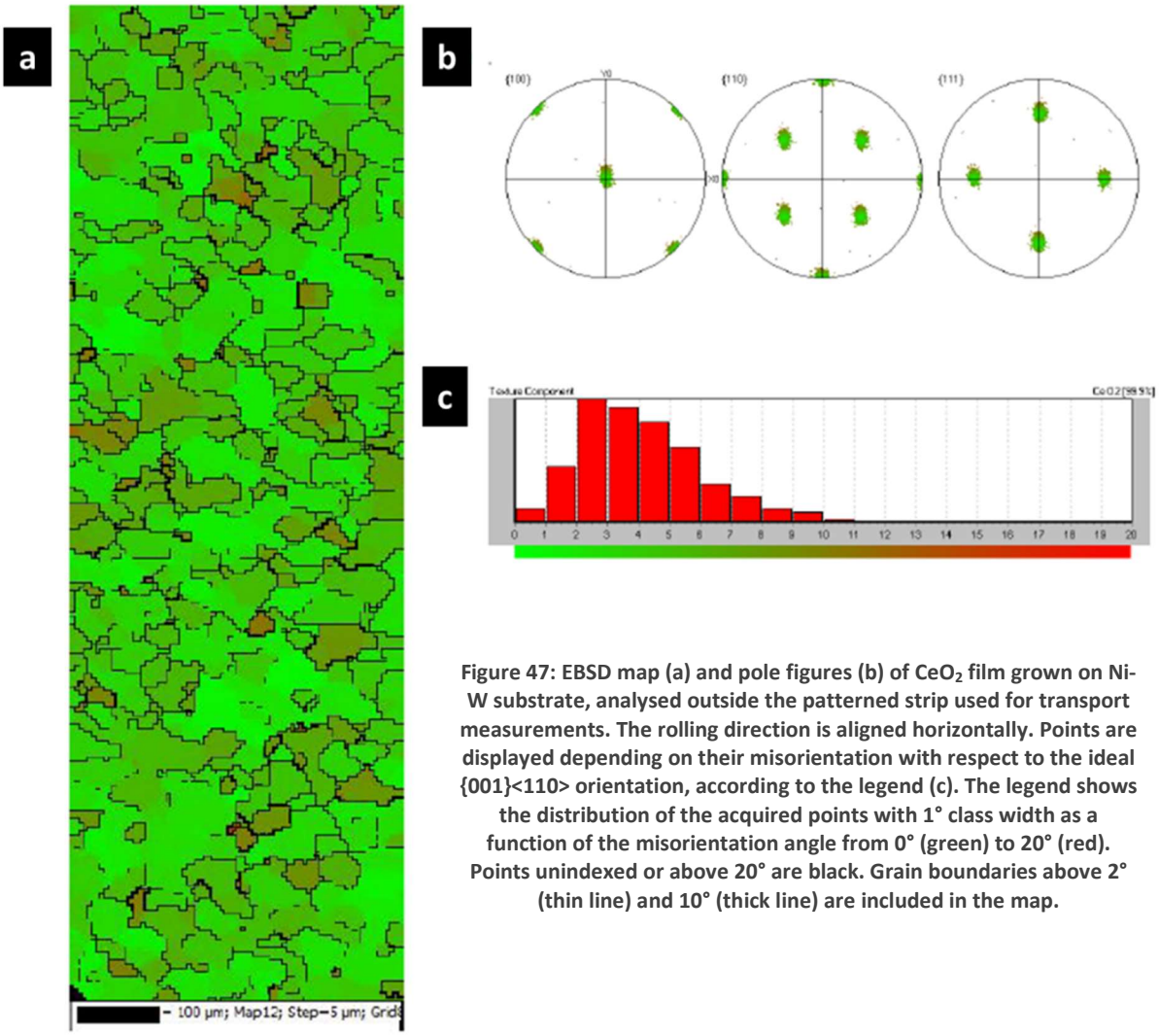

Figure 47: EBSD map (a) and pole figures (b) of CeO_2 film grown on Ni-W substrate, analysed outside the patterned strip used for transport measurements. The rolling direction is aligned horizontally. Points are displayed depending on their misorientation with respect to the ideal {001}<110> orientation, according to the legend (c). The legend shows the distribution of the acquired points with 1° class width as a function of the misorientation angle from 0° (green) to 20° (red). Points unindexed or above 20° are black. Grain boundaries above 2° (thin line) and 10° (thick line) are included in the map.

These features give rise to highly non-linear ρ(T) curves sometimes exhibiting local maxima. A similar bump in the resistivity has been observed in Ba-122/Fe bilayers grown on IBAD tapes with thin Y_2O_3 buffer layers and was ascribed to the effect of current shunt provided by the metallic template in presence of a conductive buffer layer [27]. On the other hand, comparable behaviours of resistive transitions have been often reported for different superconducting films and ascribed to a phenomenon related to the current redistribution occurring in presence of sample inhomogeneity, i.e. regions characterized by slightly different T_c and multiple paths for the bias current [56]. Therefore, the

present anomalous bump can be explained invoking the occurrence of a metallic path, likely to be ascribed to a technological issue arisen during the film patterning process, in parallel with the superconducting path with some degree of film inhomogeneity.

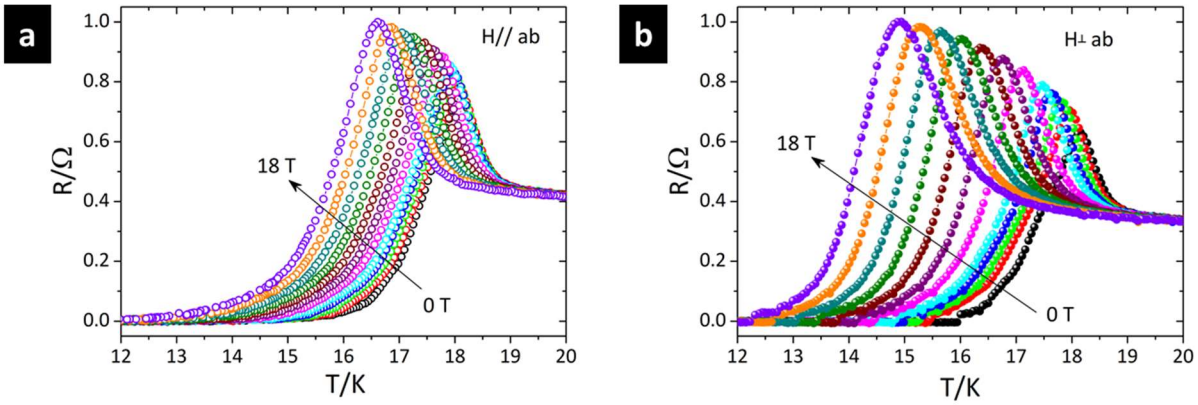

Figure 48: Resistance as a function of the temperature for the FST thin film measured perpendicular and parallel to the magnetic field from 0 to 18 T (namely at 0, 1, 2, 3, 4, 6, 8, 10, 12, 14, 16, 18 T), in a) the magnetic field is parallel to ab plane of the sample, in b)the magnetic field is perpendicular to the ab plane of the sample

In particular, the resistive transition behaviour is thus reproduced by eq. (1a) of Ref. [56], assuming R1 of ref. [56] = metallic path resistance of the present case. The irreversibility field and the upper critical field values, H_{irr} and H_{c2}, are usually evaluated from the R(T, H) curves using, respectively, the 10% and 90% of the superconductive transition criterion. This method is more difficult to be applied to the measurements presented in this work since the reported anomalous behaviour, though accounted for by the presence of multiple paths for the bias current, makes any evaluation of the normal state resistivity value quite speculative. The alternative criterion is thus adopted, considering the 10% of the peak resistance at T_m and $T_m(H)$ dependences as the H_{irr} and the H_{c2} curves, respectively. In the first case, the values will be close to those evaluated with the standard 10% criterion. In the upper critical field case, a qualitative picture of the $H_{c2}(T)$ dependence can be obtained, even though quantitatively underestimated. Figure 49 shows H vs T diagram, with the upper critical field H_{c2} and the irreversibility field H_{irr} calculated as reported above in both the field directions. H_{c2} vs T is very steep near T_c, with a downward curvature and slopes of about 63 T/K and 7 T/K in the parallel and perpendicular directions, respectively. Such values are quite high, even not as high as those observed in thin films deposited on single crystals which can reach up to 500 T/K and 30 T/K in the two directions. The extremely high values reported on our strained film deposited on $LaAlO_3$ and CaF_2 were explained in terms of an extreme Pauli-limited $H_{c2}(T)$, indicative of the Fulde–Ferrell–Larkin–Ovchinnikov (FFLO) state [57] .

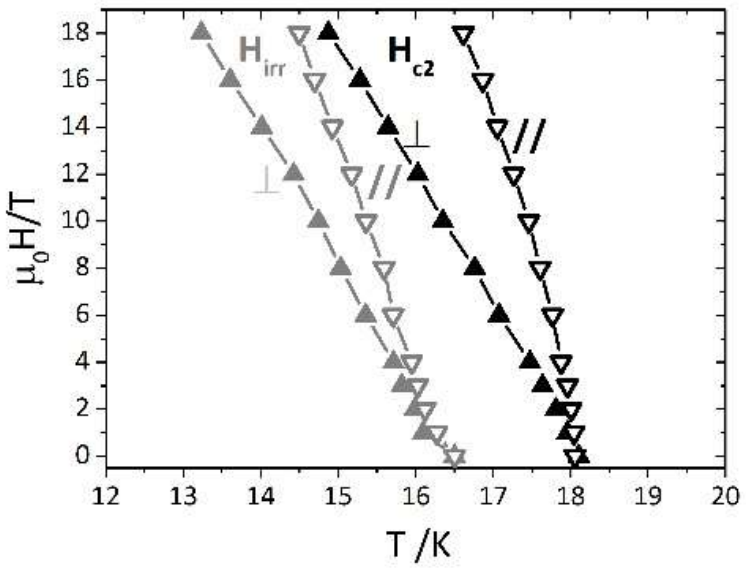

Figure 49: H-T diagram of the 11 thin film. H_{c2} and H_{irr} are calculated from the $T_m(H)$ and the 10% of the peak resistance at T_m dependences, respectively.

The slopes near T_c are significantly higher than those reported on IBAD-LMO-buffered metal tapes [33]. To estimate H_{c2} values at zero temperature, the Werthamer-Helfand-Hohenberg relationship is applied:

$$H_{c2}(0) = -0.693 T_c \left(\mathrm{d}H_{c2}/\mathrm{d}T\right)\big|T_c$$

and obtained 790 T and 90 T for H // ab and H // c respectively. The anisotropy is not high: H_{c2}//ab / H_{c2}//c is about 2.3 at 17 K while H_{irr}//ab / H_{irr}//c is about 1.8 at 15 K, both higher though than the values reported in thin films grown on single crystals (where H_{c2} anisotropy can be as low as 1.2 [36]) and on IBAD-LMO-buffered metal tapes [33].

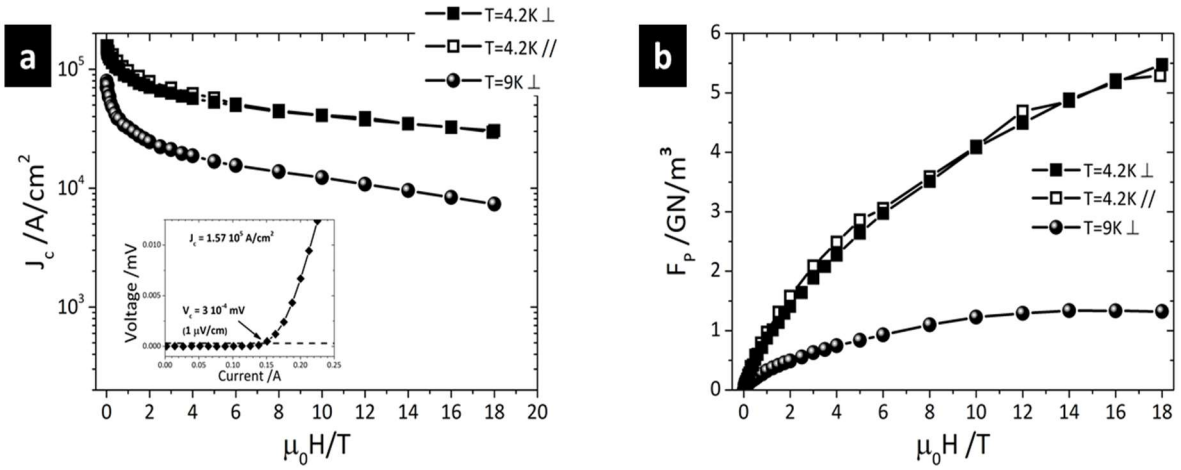

Figure 50: a) Transport J_c vs H at 4.2 K (both perpendicular and parallel to the magnetic field) and 9 K measured on the strip. In the inset, the I-V curve at 0 T, 4.2 K with indication of the criterion for the J_c calculation. b) Pinning force densities, calculated from the critical current density values, as a function of the applied field.

In Figure 50 a the critical current density of the CC as a function of the magnetic field measured up to 18 T at 4.2 K and 9 K is shown. Self-field J_c value at 4.2 K is above 1.7 10^5 A/cm$_2$ and above 3.0 · 10^4 A/cm^2 in fields up to 18 T, while the self-field J_c value at 9.0 K is above 7.0 10^4 A/cm^2. The J_c curves measured at 4.2 K with H parallel and perpendicular to the tape surface overlap in the whole magnetic field range up to 18 T, indicating an isotropic behaviour in these regimes. In

Figure 50 b), the pinning force density calculated as $F_p = J_c \cdot B$ are reported: at 4.2 K it is still far from its maximum at 18 T, while a plateau starting from 14 T at 9 K is observed. The relatively low J_c values with respect to the previously reported FST coated conductor architectures [5,36] can be explained by the presence of some inhomogeneity in the 11 film. However, this effect can be mitigated through the optimization of growth conditions and texturing of both buffer layer and FST.

C.2 CHEMICALLY GROWN BUFFER LAYERS

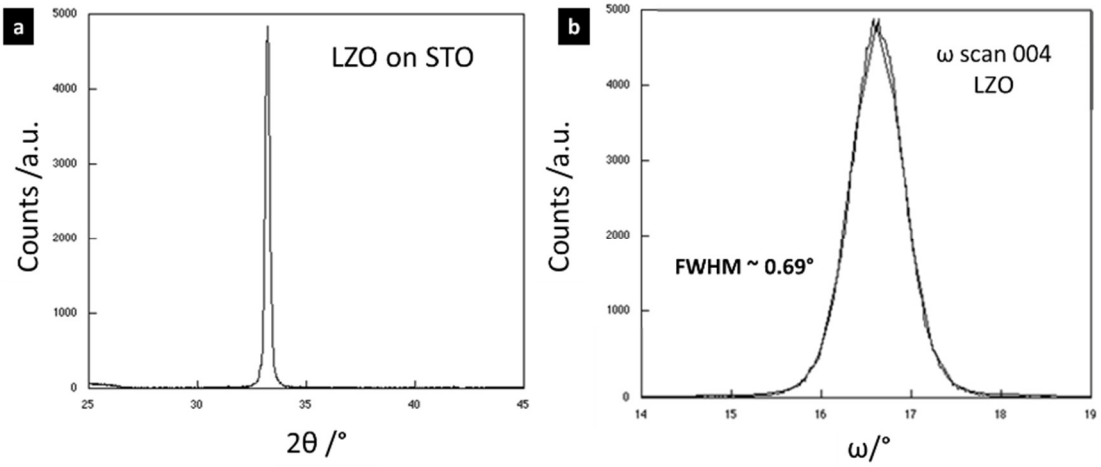

Figure 51: X-ray characterization of LZO buffer layer deposited on (001) STO single crystal substrate. a) θ-2θ scan, b) Rocking curve of the (004) peak of LZO with a FWHM ~ 0.69 °.

Despite the good results obtained with CeO_2 buffered Ni-W substrates, it is possible to further simplify the production of CC using other methods to deposit the buffer layer. Chemical methods like Chemical Solution Deposition (CSD) and Metal Organic Deposition (MOD) are more scalable and cost effective than the PLD. For this reason, a parallel activity on the development of this type of buffer layers started in collaboration with ENEA, detailed information about the preparation of these buffer layers can be found in [58]. The best results were obtained using NiW 5% substrate with a buffer layer of about 50 nm of CZO (CeO_2 doped ZrO_2), deposited with CSD, and with a buffer layer of LZO ($La_2Zr_2O_7$), 50 nm thick deposited with MOD. In order to start a more systematic study about this kind of buffer layers, we started to working on CZO and on LZO buffer layers deposited respectively on YSZ (Yttria-stabilized Zirconia) an on Strontium Titanate (STO) single crystal substrates and then the activity moved on using the same buffer layers but deposited on Ni-W. C.2.1 Buffer layers grown by chemical methods on single crystals

Figure 51 shows the X-ray characterization of the LZO buffer layer deposited on STO, the buffer layer is grown epitaxial and shows a rocking curve of about 0.69°. The CZO buffer layer, 20 nm thick, was deposited in Ar/H_2 at 950 °C and shows an epitaxial growth on the substrate with a rocking curve of about 0.73° (Figure 52). These buffer layers were optimized to have the best orientation and the best roughness with a reduce thickness. All the measurements presented in this section was performed at ENEA Frascati.

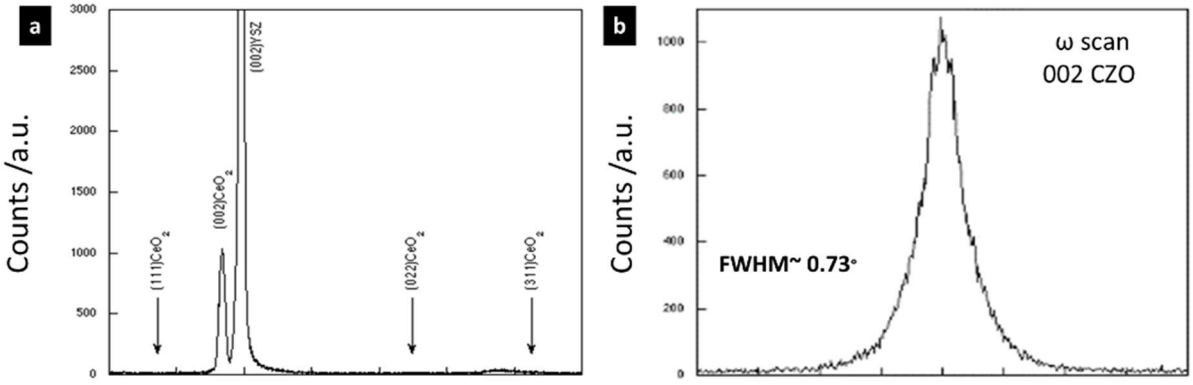

Figure 52: X-ray characterization of CZO buffer layer, 20 nm thick, deposited on YSZ (001) single crystal. a) θ-2θ scan, b) Rocking curve of the (002) peak of CZO with a FWHM ~ 0.73 °.

On CZO and LZO we deposited FST thin films with (grey curves) and without (black curves) seed layer with the procedures largely described in the previous sections. In Figure 53a) and b) the XRD measurements performed on thin films deposited on LZO are shown: θ-2θ scan reveal that the film has an orientation along c axis, all the (00l) peaks of the FST phase are present. Moreover, the film with seed layer shows double peaks the ones at low angle belongs to the seed layer and the others belongs to the superconducting films. Both films also show a rocking curve between 5°-6° Figure 53b) which is very large for a film grown on single crystal.

On the contrary, as can be seen in Figure 54 the films grown on CZO as single layer (Figure 54a) shows the (001) peak of the FST phase, and it has no rocking curve confirming that the films does not have an

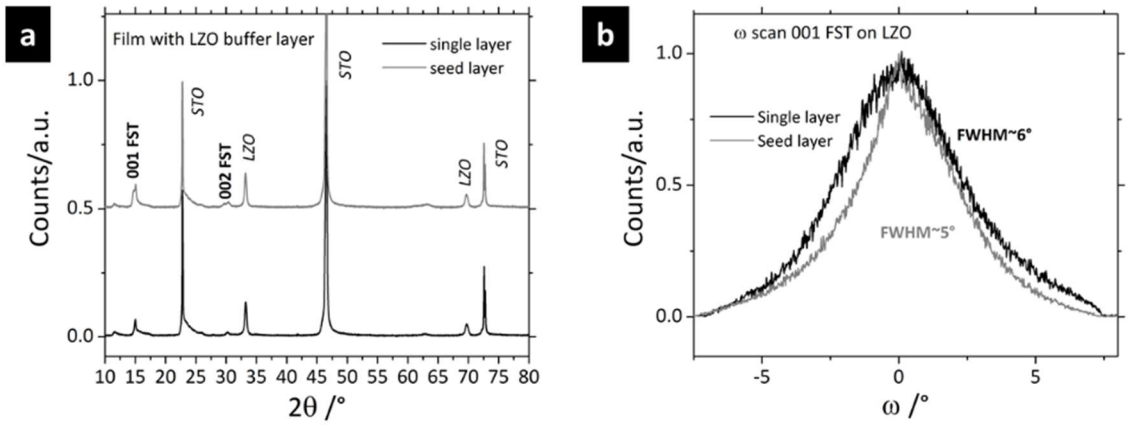

Figure 53: XRD measurements performed on FST thin films deposited on single crystal substrates with LZO buffer layer. The black curves indicate a film without seed layer while the grey curves indicate the film with the seed layer. a) θ-2θ, b) Rocking curves.

out of plane orientation. Meanwhile, the film deposited on CZO with seed layer shows also the others 00l peaks of the FST with Δω~ 0.78° (Figure 54b), and Δϕ~1.27(Figure 54c).

Figure 55 shows the superconducting transition of the films deposited on LZO with and without seed layer and the film with seed layer deposited on CZO. The film deposited on CZO with seed layer Figure 55a) has the highest T_c onset at 18 K and T_{c0} is about 16.7 K. The films deposited on LZO (Figure 55b) show lower T_c but the transitions are good, and the films seems to be monophasic. Moreover, the presence of seed layer increments the T_c of about 2K (Figure 55b). The showed results are very preliminary and seems to be promising for further studies.

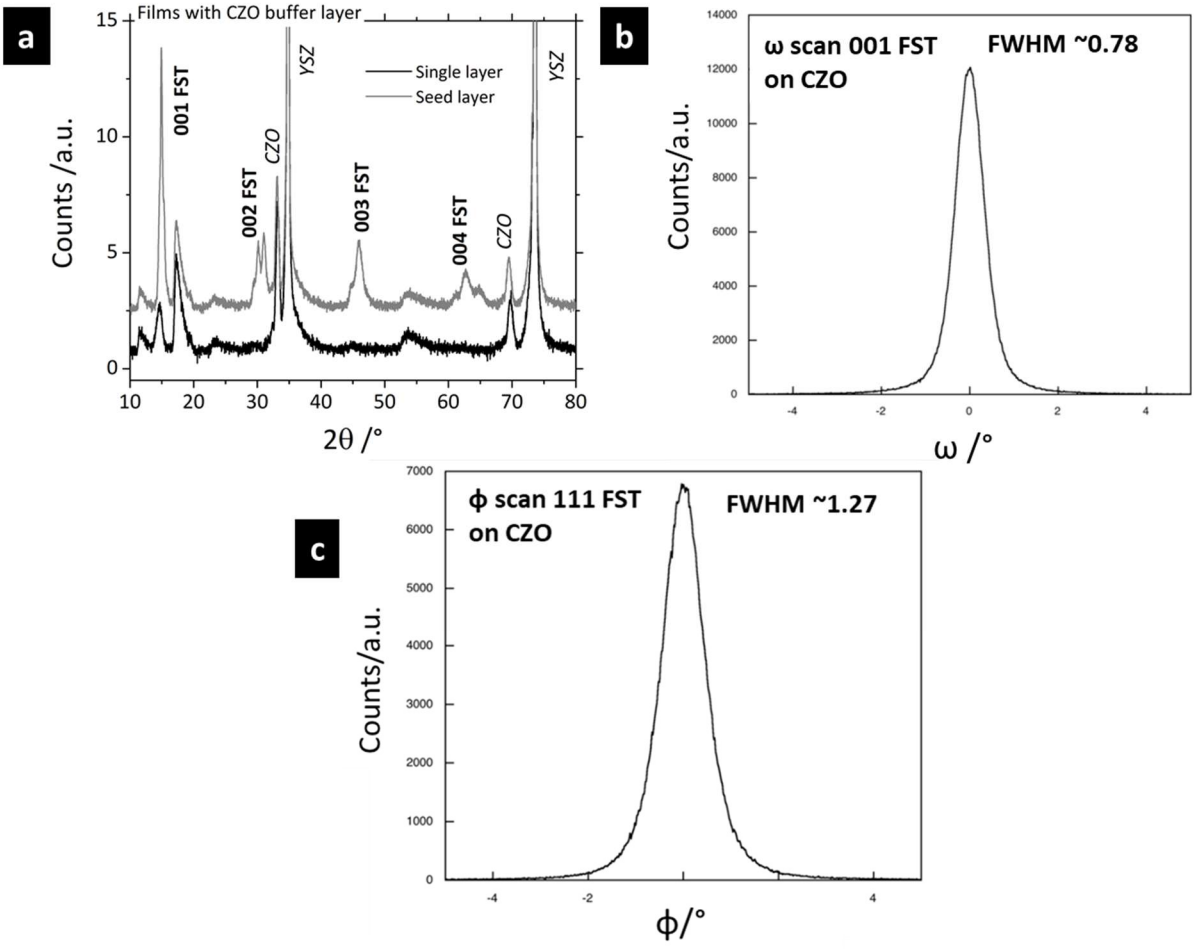

Figure 54: XRD measurements performed on FST thin films deposited on single crystal substrates with CZO buffer layer with seed layer. The black curves indicate a film without seed layer while the grey curves indicate the film with the seed layer. a) θ-2θ, b) ω-scan of the film described in a), c) ϕ-scan of the 111 direction of the film described in a).

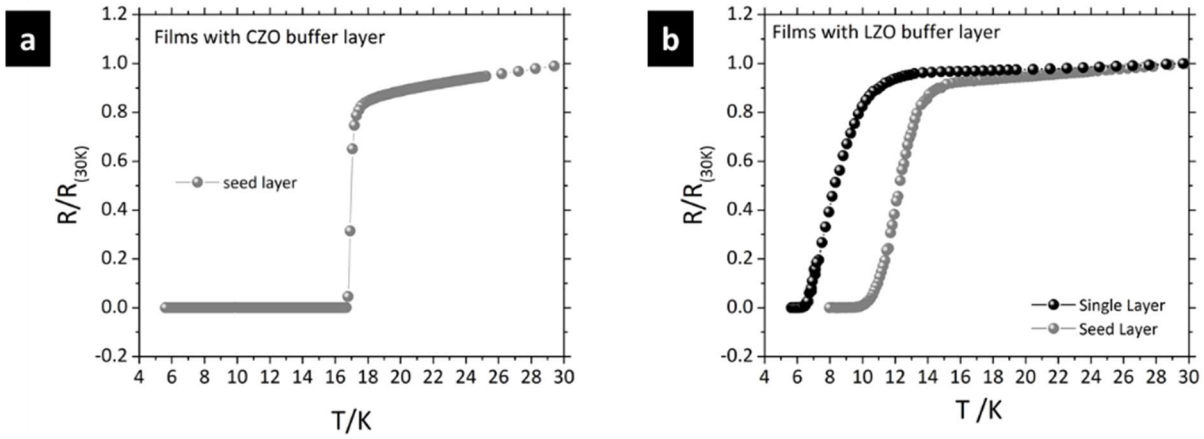

Figure 55: R(T) performed on FST thin films deposited on singe crystals substrates with CZO (a) and LZO(b) buffer layers. The black curves indicate film without seed layer while the grey curves indicate films with seed layer.

C.2.2 Buffer layers grown by chemical methods on Ni-W

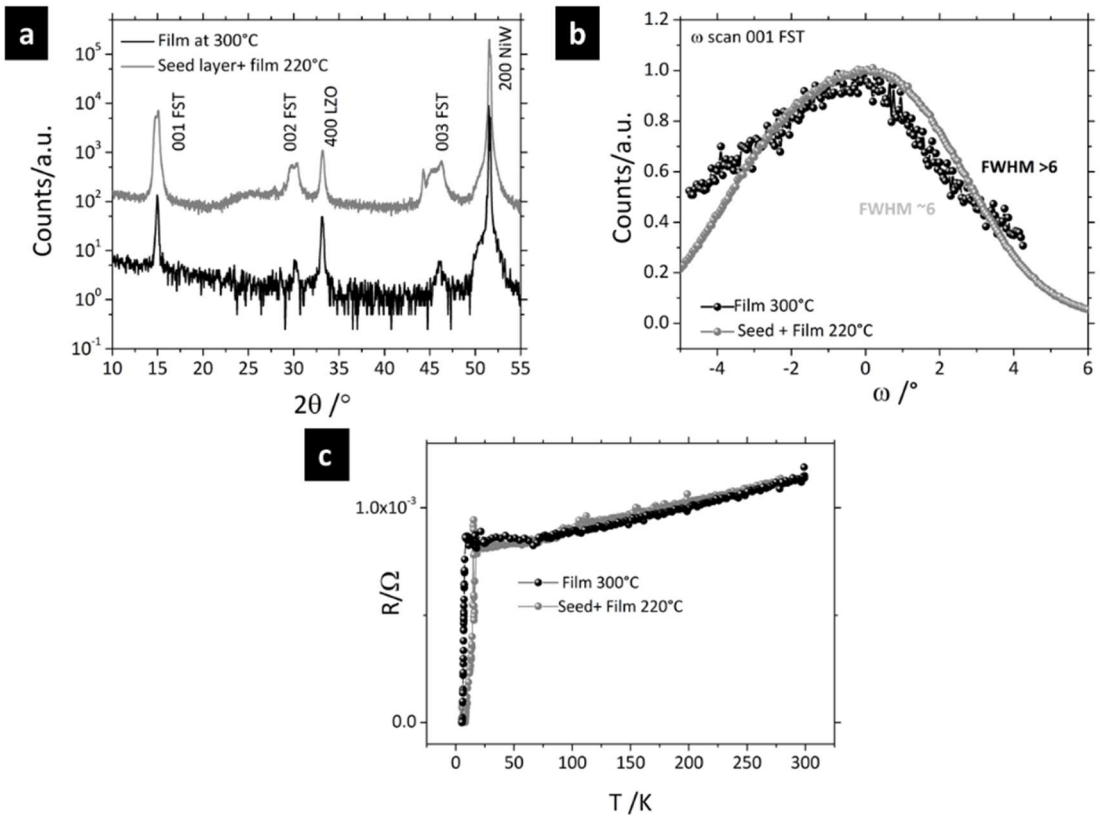

Figure 56: Analysis of two film deposited on Ni-W with LZO buffer layer. The film in grey was deposited at 220°C with a seed layer of FST while the film in black was deposited at 300°C. a) θ-2θ scan, b) ω-scan of 001 peak of FST c) R(T) of the films.

Based on the results obtained with chemical buffer layers on single crystal substrates, we tried to reproduce the results using NiW5% substrates with the same buffer layers. LZO buffer layer, 50 nm thick, was deposited on Ni-W substrate with MOD method and then heat treated in CO_2 atmosphere

at 450°C. Figure 56 show the analysis made on two FST thin film deposited on Ni-W with LZO buffer layer. The first film (black) is without seed layer instead the second film (grey) is with seed layer. As can be seen, in both cases the films were grown epitaxially on the substrate, the film with seed layer shows an improved out of plane orientation and critical temperature. Anyway, the critical temperature is in both cases is very low and this leads to the conclusion that 50 nm of LZO are useful to create a barrier for Ni interdiffusion but probably the interdiffusion is not completely blocked.

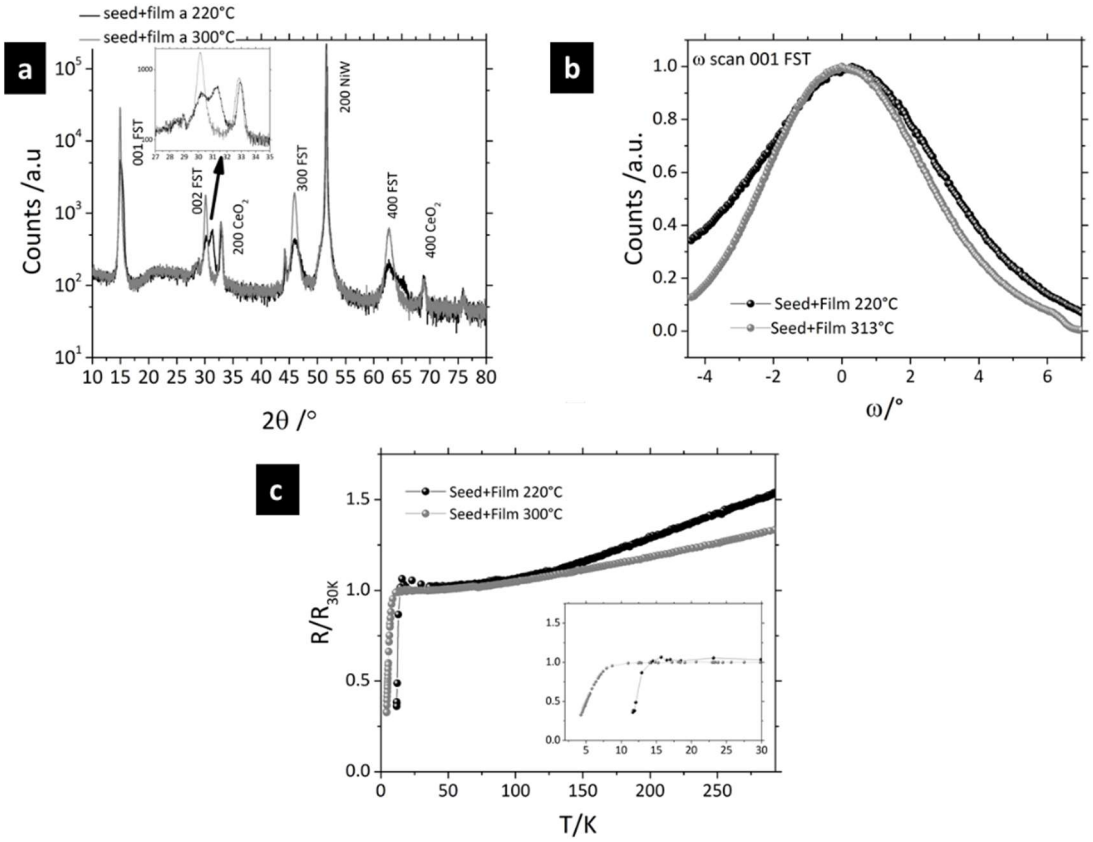

Figure 57: XRD analysis and R(T) of two film deposited on Ni-W with CZO buffer layer. The film in grey was deposited at 300°C with a seed layer of FST while the film in black was deposited at 220°C with seed layer. a) θ-2θ scan, b) ω-scan of 001 peak of FST c) R(T) of the films.

CZO (CeO_2 doped Zr) buffer layer, 50 nm thick, was deposited with CDS method on Ni-W. In Figure 57 XRD and R(T) measurements performed on two FST thin films 240 nm thick with the seed layer are shown. The main difference between these two films is the temperature of deposition of the film itself, the first (black) was deposited at 220°C while the second one (grey) was deposited at 300°C. Both films grow epitaxially with a good orientation along c axis, the film deposited at 220°C shows in θ– 2θ scan double peaks while the film deposited at 300°C shows single peaks, probably because in this case the temperature was closer to the one used for the seed layer deposition so the two layers have a similar structure. Both films show superconducting transition and the film deposited at 220°C has the onset at higher temperature (16 K). However, a complete resistive transition was not observed: this could be probably ascribed to an insufficient thickness of the buffer layer which is not enough to completely block the Ni diffusion from the substrate to the film, as in the case of LZO. The activity on chemically deposited buffer layers is still ongoing, aiming to find the best conditions to completely block the Ni diffusion. However, these results are promising for further studies.

4 EFFECTS OF PROTON IRRADIATION ON 11 THIN FILMS

4.1 IRRADIATION ON SUPERCONDUCTORS FOR HIGH FIELD APPLICATIONS

For high field applications three fundamental parameters of superconductors needs to be considered: T_c, H_{irr} and J_c. The T_c is directly related to the mechanism of superconductivity, and in particular to the interaction between electrons that formed the Cooper pairs, while H_{irr} and J_c are governed by the vortex pinning strength, which is determined by the ability of the defects in superconducting materials to pin the vortices. The defects can be naturally present or artificially grown inside the superconducting materials and can be 1D (columnar defects and dislocations), 2D (grain boundaries) and 3D (particles). In general, thin films contain naturally grown defects, which can also be induced by the presence of the substrate[4]. Further improvements are achievable introducing artificial pinning centres with an appropriate dimension and density: heterogeneities in the superconductors structure can be introduced into the materials by mechanical deformation, inclusion of second phases, voids, and impurities. A common way to introduce defects inside the materials is the irradiation. Irradiation experiments are carried out exposing superconductors to charged particles, ions, and neutron to introduce in a controllable manner, choosing appropriate ion species and energy, different kind of defects to study the effects on the superconducting properties. Moreover, irradiation experiments are reproducible in different types of materials and allow to measure the same sample before and after irradiation avoiding the common variability between different samples. The introduction of defects in the superconductors impedes the formation of the Copper pairs, causing, especially in materials with low coherence length as cuprates and IBS, a strong decrement of T_c. However, if the defects are larger enough, they can act as efficient pinning centre enhancing the J_c. The physical laws that describe the interaction between a nuclear particle incident crystalline material are so complex, that a simple theoretical treatment is not possible. Different heterogeneities landscapes can create completely different effects on J_c and H_{irr}.

In view of high field applications, irradiation is not only meaning to study the pinning mechanisms in each material but can give an estimation of the robustness of the superconductor in harsh environments such as those present in high-energy accelerators or fusion reactors.

As an example, the radiation spectrum in future accelerators HiLumi LHC - which is an upgrade of the already existing LHC - and FCC (Future Circular Collider), comprises several high energy sources: neutrons, protons, pions, electrons and photons [59,60]. Each radiation source has different energies, different fluences and different effects on every part of the magnets. Table 4 reports the main characteristics of the HiLumi LHC, and of the FCC project starting from the FCC/Run 1 to final goal of FCC/Run2. The HiLumi LHC and the FCC project compared to the currently operating LHC will have higher magnetic field, higher luminosity and consequently higher irradiations (indicated in the table with the displacement per atom-*dpa* parameter which is proportional to the fluence).

	HiLumi LHC	FCC/Run 1	FCC/Run 2
Luminosity	3000 fb^{-1}	5000 fb^{-1}	30 000 fb^{-1}
Magnetic field	12 T	16 T	16 T
dpa	2.5 $x10^{-4}$	5 $x10^{-4}$	3 $x10^{-4}$

Table 4: Parameters of the new particle accelerators in study at CERN HiLumi LHC and FCC [61].

The *dpa* estimates the damage induced in the materials caused by the interaction of the incident particles with the nuclei of the target material. This parameter is useful when the effect of different irradiating particles must be considered, since at the same fluence for different particles the physical conditions are very different. *Dpa* contains all the information regarding the type of particle, their energy and the type of target material, becoming a parameter for estimating the damage induced by irradiation. Moreover, an essential property of *dpa* in the presence of various irradiating particles the total *dpa* is given by the sum of all *dpa*:

$$dpa_{tot} = \sum (dpa)_j$$

Equation 1

The *dpa* is estimated by simulation exploiting Monte Carlo methods, and different type of interactions between particles and target can be considered or overlooked depending on the type of experiments. For the calculation of the damage induce by irradiation on the Nb-based superconducting magnets in LHC and FCC usually the *dpa* estimated by the Fluka code is used (http://www.fluka.org), and following Ferrari et al [62] the *dpa* in the Fluka code is defined as:

$$dpa = \frac{A}{V N_A \rho} N_F$$

Equation 2

Where A is the molar mass (g/mol), V the volume (cm^3), N_A the Avogadro number (mol^{-1}), ρ the mass density (g/cm^3), and N_F the number of Frenkel pairs.

According to Equation 2 the *dpa* is directly related to N_F, which is a compound crystallographic defect in which an interstitial lies near a vacancy. A Frenkel defect forms when an atom or ion leaves its place in the lattice creating a vacancy and becomes an interstitial by lodging in a nearby location. For the FCC study, CERN launched a detailed study of the variation of the superconducting properties of Nb_3Sn wires during the entire acceleration lifetime. All the properties as T_c, J_c, H_{c2} and lattice parameters were studied as function of *dpa*. Figure 58 shows the decrement of T_c as function of the fluence (left) and of *dpa* (right).

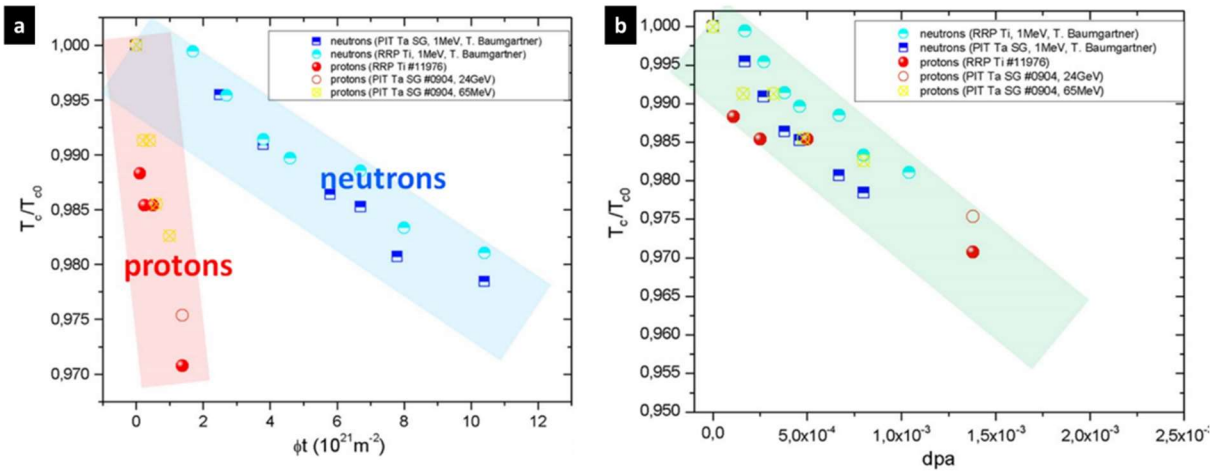

Figure 58: Dependence of T_c of Nb_3Sn cables on fluence(a) and on *dpa* (b)[63].

As can be seen a universal relation between T_c and *dpa* was found, for a given value of *dpa* the decrease of T_c is the same regardless of the type of projectile and the different energy during irradiation [64,65]. A similar relation was also found for the lattice parameters: the increment of *dpa* is directly proportional to increment of the lattice parameters (Figure 59).

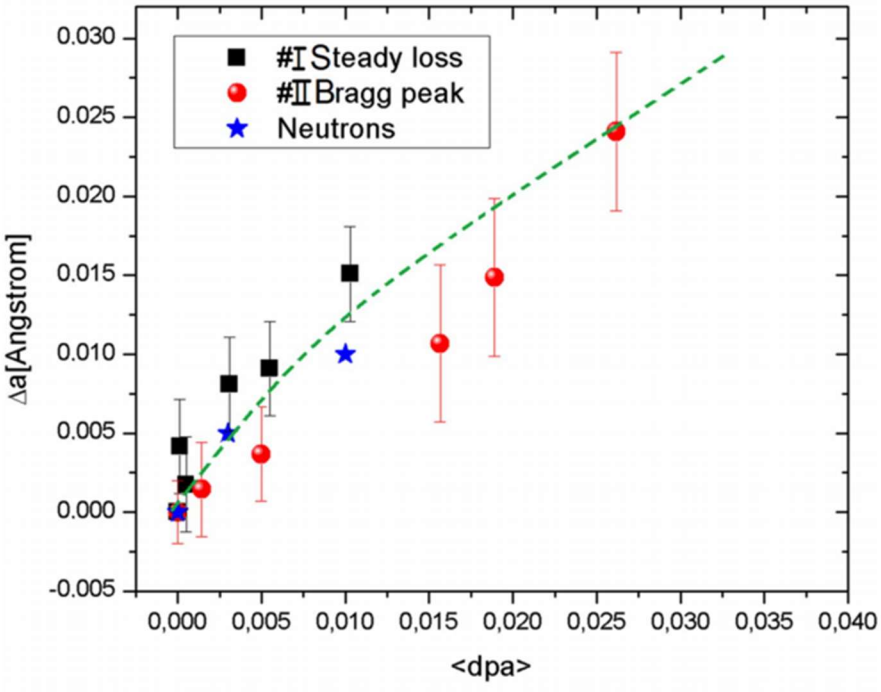

Figure 59: Variation of the lattice parameter as a function of the *dpa* [66]

This confirms the relation of T_c and lattice parameters with the number of Frenkel pairs (see equation 2). Also, for J_c a linear dependence on *dpa* is found (Figure 60): J_c increases increasing the *dpa* up to a certain level, however the mechanism of dependence of J_c from *dpa* is different from the one found for T_c and lattice parameters [64].

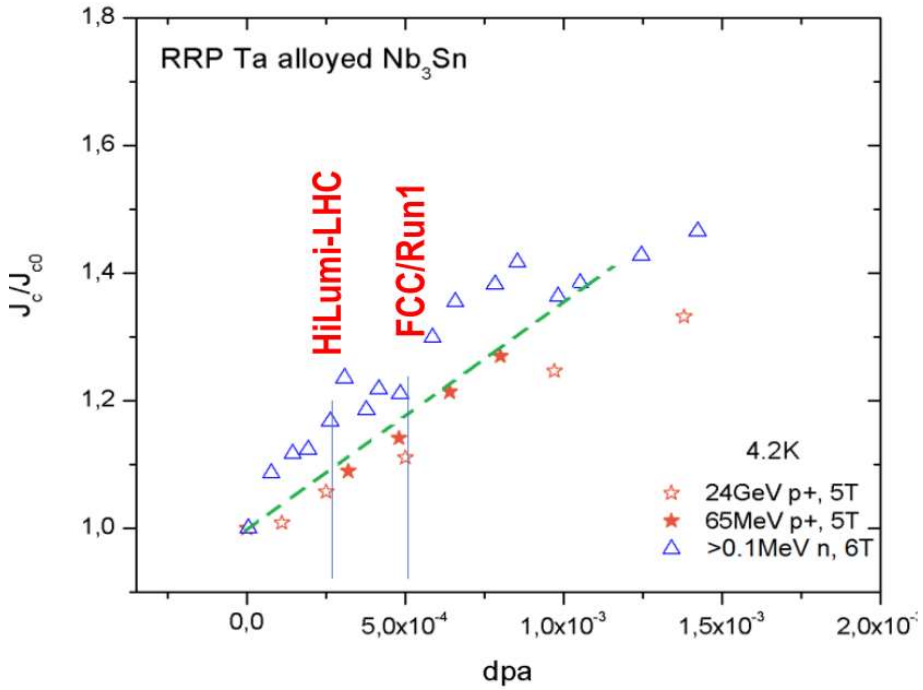

Figure 60: Variation of J_c versus *dpa* for Nb_3Sn cables [61].

4.2 IRRADIATION ON IRON-BASED SUPERCONDUCTORS

In view of future large-scale applications of IBS conductors for high magnetic field, the study of the influence of irradiation on these materials becomes essential both to possibly enhance the pinning properties of the conductors and to evaluate the possible employment in harsh environments. Many studies on the effects of irradiation on IBS single crystal have already been published, but just a few numbers of experiments on irradiated thin films are reported in literature. Very recently, M. Eisterer published a review on the effects of irradiation on IBS thin films focusing particularly on neutron irradiation [67]. Thin films of IBS were irradiated with neutrons, protons at different energies, Au ions and α-particles, the results obtained are very different and strongly related to the type of particles, their energy, the chemical phase of the films but they also depend on other parameters as the substrate and the implantation depth of the irradiating particles. In Table 5 a summary of the variation of T_c obtained in different experiments of irradiation of IBS thin films is reported. As can be seen from the table, the most systematic study was only done for 11. For the 1111 phase, Tarantini et al demonstrated that the irradiation of NdFeAs(O,F) thin films with α-particles causes an increase of both H_{c2} and H_{irr} and an increment of J_c only for H//c, on the contrary for H//ab the defects induced by irradiation competes with intrinsic pinning reducing J_c [68]. For the P-doped Ba-122 thin films fabricated with molecular beam epitaxy (MBE) and irradiated with Au ion, a decrease of T_c of 0.8K was reported for a dose of 7.26 10^{11} cm^{-2}. Moreover, authors considered the role of the substrate supposing that the irradiation causes a heating of the substrate resulting in an additional damage [69]. The effect of proton irradiation on Co-doped Ba-122 thin films was reported both from Maiorov et al. [70] and from Schilling et al [71]. Schilling et. al focused their work on films irradiated with 200 KeV protons, showing that the disorder resulted after irradiation causes transition between s ± and s++ states but they do not report data about H_{c2} and J_c.

Material	Particle	Total or max dose (cm^{-2})	Change in T_c (K)	Reference
FST	Fast neutrons	$10.2x10^{17}$	-0.3	[72]
FST	190 KeV protons	$10.2x10^{17}$	+0.5	[73]
FST	6 MeV Au	$1.0 x10^{12}$	-0.5	[74]
FST	3.5 MeV protons	$5.0 x10^{15}$	-7.0	[75]
Co-doped Ba-122	3 MeV protons	$2.0 x10^{16}$	-1.0	[70]
Co-doped Ba-122	200 KeV protons	$1.8 x10^{15}$	-18	[71]
P-doped Ba-122	250 MeV Au	$7.3 x10^{11}$	-0.8	[69]
NdFeAs(O,F)	2 MeV He	$5.0 x10^{15}$	-3.0	[68]

Table 5: Summary of the results obtained irradiating IBS thin films[23] .

On the other hand, Maiorov et al reported that films irradiated with 3 MeV protons show a decrease in T_c of about 1K, a reduction of J_c at low fields and an increment of J_c at high fields especially for H//ab, thanks to an anisotropic contribution of the point like defects induced by irradiation.

For the 11 family, different results have been reported depending on the phase, the type of particle and its energy. For example, thin films grown on $LaAlO_3$ irradiated with neutrons, duplicated their critical current at 15 K with no change in T_c [72]. Conversely, even an increase of T_c was found after proton [73] irradiation. This remarkable result highlights a mechanism for an increase in transition temperature which can overcompensate the detrimental effect of disorder on T_c. In FST thin films irradiated by low-energy protons, not only J_c (T=4.2K, H=0) was increased by 55% and pinning force was increased in the high-field regime upon irradiation, but remarkably a simultaneous T_c enhancement of 0.5 K was detected [73] . The authors considered possible mechanisms for T_c enhancement in FST films and they interpreted their results in terms of coexistence of nanoscale regions subject to compressive and tensile strain, originated by the irradiation defects. The same group recently reported an enhancement of J_c of around 70% at 9 T//c and 10 K after the irradiation of FST thin films with 6 MeV Au-ions [74]. Moreover, FST thin films grown on CaF_2 were reported to show a decrease in T_c up to 7 K upon irradiation with 3.5 MeV protons [75].

4.3 EFFECTS OF PROTON IRRADIATION ON THE SUPERCONDUCTING PROPERTIES OF 11 THIN FILMS

With the aim to evaluate the possible applications of 11 CC in high field and harsh environments, a systematic study of the effects of proton irradiation on FST thin films deposited on CaF_2 single crystals was carried out. The activity started in 2014 thanks to a collaboration between CNR Spin and Politecnico of Torino within the PRIN project of the Italian Ministry of University and Research "RIDEIRON: Using controlled disorder to investigate the mechanism of iron-based superconductors".

During my PhD thesis I continued a scientific collaboration with the group of Prof. L. Gozzelino at Politecnico of Torino to investigate the effects of irradiation on 11 films. Now this activity and collaboration has been included in the PRIN project 2017 HIBiSCUS (High performance-low cost Iron Based Coated conductors for high field magnets) which has just started. The aim of this project is to develop the methodology for fabricating IBS conductors for high magnetic field application and includes a part of the study of the effects of irradiation on thin films deposited both on single crystals and on technological substrates. The project includes irradiation with protons at different energies and is done in collaboration with Politecnico of Torino and the INFN-LNL (Istituto Nazionale di Fisica Nucleare - Laboratori Nazionali di Legnaro, Italy).

4.3.1 Experimental details

The effects of 3.5 MeV proton and of 0.5 MeV proton irradiation on FST thin films grown on CaF_2 was explored. In particular, an experimental investigation with different irradiation fluences up to $7.30 \cdot 10^{16}$ cm^{-2} and different proton implantation depths was carried out, in order to clarify whether and to what extent the critical current is enhanced or suppressed, what are the effects of irradiation on the critical temperature, the resistivity and the critical magnetic fields, and finally what is the role played by the substrate in this context.

The thin films used for this irradiation experiment were deposited on oriented 001 CaF_2 single crystals with the procedure largely described in chapter 2 (pag. 30). Seven films having a 100 nm thick were prepared for irradiation. Five films were irradiated with 3.5 MeV protons and, three of them, indicated in the following as samples A, B and C, were patterned and designated for transport measurements while samples D and E were analysed with XRD. The samples F and G were irradiated with 0.5 MeV protons and they were patterned and designated for transport measurements. Before irradiation, all the films were analysed with XRD using a four-circle diffractometer. This analysis confirms the phase purity of all films and the optimum epitaxial growth of all the films. Φ scans reveal that films grow rotated by 45° with respect to the a axis due to the good matching with the half of the diagonal of CaF_2 crystalline cell, as already reported [4]. By using the *00l* diffraction peaks, the values of the *c* cell parameter for the different samples were evaluated by means of Rietveld refinement with the program Fullprof. At this scope, the instrumental resolution function and the zero-shift parameters were refined using the CaF_2 substrate as reference; diffraction lines were modelled by a Thompson-Cox-Hastings pseudo-Voigt convoluted with axial divergence asymmetry function. The so obtained values were fixed and, imposing a full c-axis texturing, the parameters pertaining to the $FeSe_{0.5}Te_{0.5}$ thin films were refined, i.e. the lattice parameter c and the Lorentzian strain parameter. Lattice micro-strain along [001] was evaluated by the refined strain parameters and analysing the broadening of diffraction lines by means of the Williamson-Hall plot method [76]. Generally, in the case where size effects are negligible and the micro-strain is isotropic, a straight line passing through all the points in the plot and through the origin has to be observed, where the slope provides the micro-strain: the higher the slope the higher the micro-strain. If the broadening is not isotropic, size and strain effects along crystallographic directions can be obtained by considering different orders of the same reflection. In the present case, all the analysed diffraction lines pertain to the same ab-plane. In order to allow the measurement of critical current, nine Hall bar shaped micro-bridges of 20x50 μm^2 size were realized as previously described in 0 (see Figure 61).

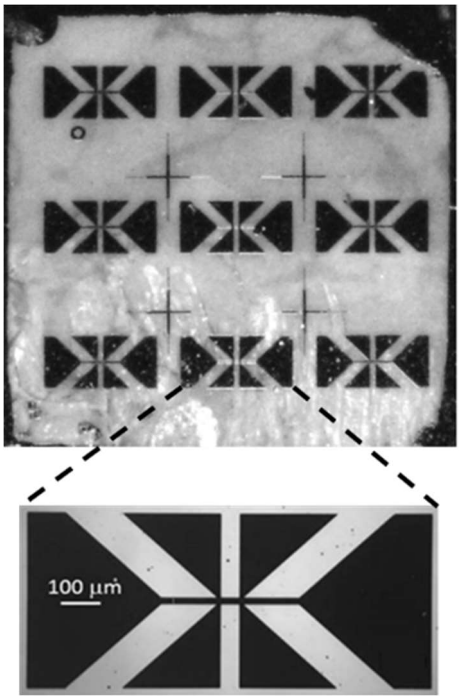

Figure 61: Optical viewgraph of a FST thin film sample showing the nine Hall bar shaped micro bridges and a magnification of a single micro bridge 20 µm wide with voltage taps 50 µm apart.

Single micro-bridge or groups of micro-bridge were then selectively irradiated with different fluence values as detailed in the following. Electrical transport properties of the micro bridges of the samples A, B, D, F and G as a function of temperature and magnetic field were measured in a PPMS by Quantum Design up to 9 T, while micro bridges C have been characterized in a Cryogenic-Free Measurement System (CFM) by Cryogenic Ltd. up to 16 T. Resistivity measurements as function of the applied magnetic field have been performed by a standard four probe current-biased measurement technique. Critical current values at different temperatures and magnetic fields were extracted from voltage versus current characteristics acquired in the PPMS system by sweeping the current from zero with exponentially increasing steps, with the aim to avoid heating problems. CFM current-voltage measurements have been performed by delta mode four probe technique ad-hoc modified in order to minimize possible heating effects. In this configuration, the current bias is pulsed; each pulse is in rectangular shape with a power-on time of 100 ms and an inter-pulse spacing of 2 s. The pulse amplitude is increased linearly. The critical current value was defined with the 10 µV/cm criterion. The films were irradiated with 3.5 MeV protons at the CN Van de Graaf accelerator and with 0.5 MeV beam of protons with AN 2000 accelerator of INFN-LNL (Istituto Nazionale di Fisica Nucleare - Laboratori Nazionali di Legnaro, Italy). Details of the irradiation experiment (e.g. the choice of the Al-foil thickness, the adopted fluences) were guided by previous accurate simulations of the damage induced both in the film and in the substrate, obtained by the Monte Carlo code SRIM [77].

4.3.2 High-energy proton irradiation of 11 thin films

In order to investigate the influence of the proton's implantation depth on the structural and electrical properties of the films, some of the samples were directly irradiated with 3.5 MeV protons while others were irradiated with protons decelerated through the interposition of an 80-µm thick aluminium foil.

This deceleration results in an average energy of the protons impinging on the superconducting film of 1.43 ± 0.07 MeV. The energy distribution of the protons after crossing the 80 µm-thick aluminium foil (and before impinging on the sample) is reported in Figure 62.

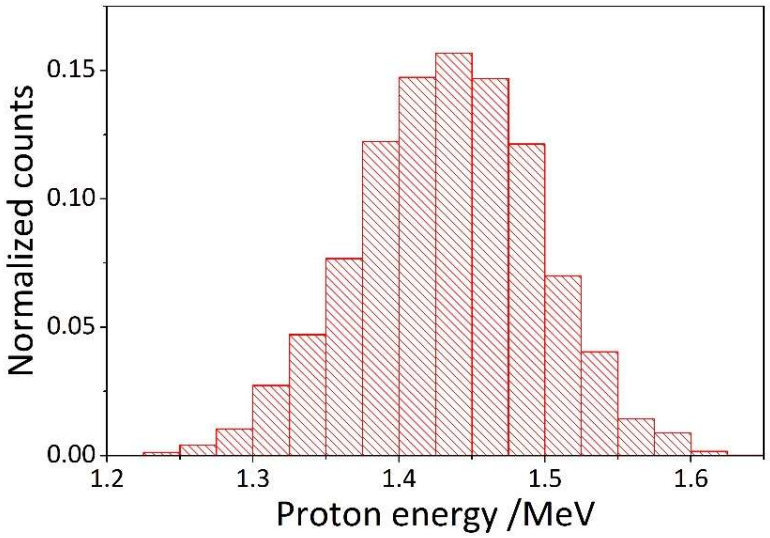

Figure 62: Energy distribution of the protons after crossing the 80 µm-thick aluminium foil (and before impinging on the sample). The counts are normalized to the total number of simulated events

In all cases, protons crossed the films and implanted into the substrate. The implantation depths in the CaF_2 substrate are 86 µm without Al foil and 21 µm with the 80 µm-thick Al foil. The implantation profiles are shown in Figure 63. Protons are expected to produce random point defects and some defect nanoclusters in the film/substrate [78], due to the Coulomb scattering with atomic nuclei. SRIM calculations predict a homogeneous energy release along the superconducting films thickness (100 nm). The Bragg peak is in the substrate, in correspondence of the implantation peak. Following ref. [79], we estimated the expected damage in the film, in terms of *dpa*, using the modified Kinchin Pease approach and assuming the displacement energy of 25 eV for all the atoms of the target [80]. Hall bars, irradiated with different fluences, are indicated by a name composed of a letter, which refers to the sample and a number, which corresponds to the *dpa* induced by irradiation. It is worth noticing that the same fluence can correspond to different *dpa* values depending on the energy of protons impinging on the film. For all samples, there is a pristine reference: for patterned samples there is a pristine Hall bar which is a not irradiated bar while samples used for XRD analysis were also measured before irradiation. It is important to have pristine data as a reference of the properties of the films before irradiation. Indeed, for PLD deposited films, the sample-to-sample variability of transport properties may be comparable to the investigating effects of irradiation.

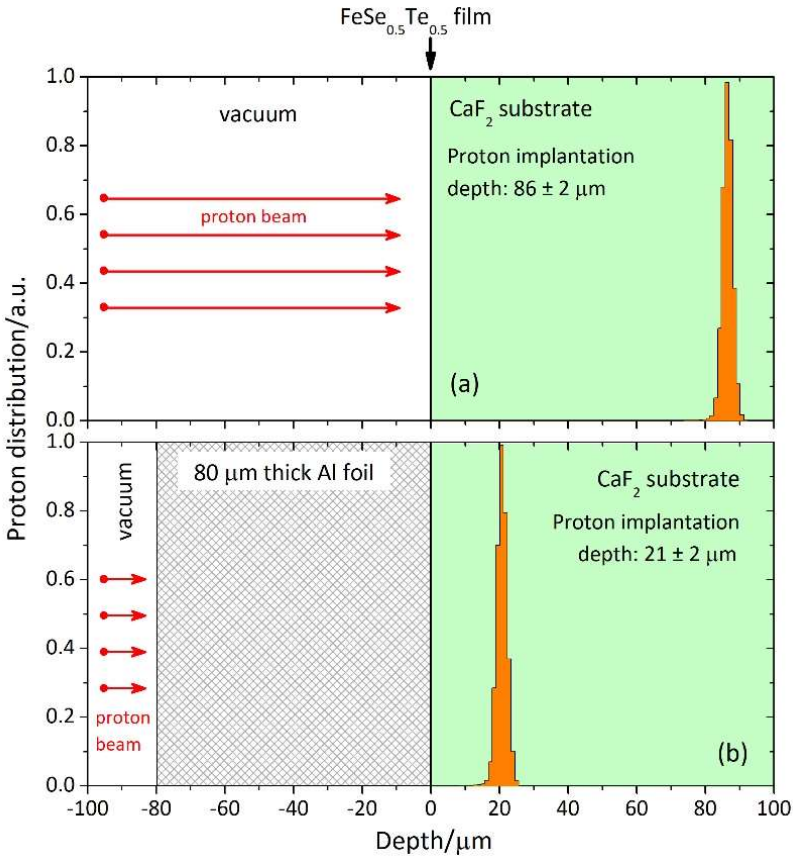

Figure 63: : Spatial distribution of the implanted protons (orange histograms) in the CaF_2 substrate (green region) without (a) and with (b) the interposition of a 80μm-thick Al foil (grey crosshatch region), used to decelerate the protons. The zero depth corresponds to the sample surface. The sample consists of a 100 nm thick $FeSe_{0.5}Te_{0.5}$ film (not shown intentionally for clarity) and its CaF_2 substrate. The interposition of the Al foil results in a shift of the implantation peak closer to the film-substrate interface.

In the forthcoming figures, the following legend is adopted: symbol shapes identify the sample, while grayscale is a qualitative measure of the irradiation dose, from empty symbols for the unirradiated Hall bars to increasingly dark colour for increasing dose. The microstructural parameters describing the lattice strain can be calculated by Rietveld refinement, obtaining the Williamson-Hall plots drawn in Figure 64; in particular, these plots provide a qualitative information about the evolution of the lattice strain along [001] as a function of the irradiation. As expected, the pristine samples D and E are characterized by about the same amount of lattice strain; remarkably, after irradiation they display opposite behaviours. In fact, sample E exhibits a decrease of the lattice strain, whereas, conversely, samples pertaining to the D series undergo a progressive increase of the strain with irradiation. This behaviour is clearly related to the different irradiation treatments experienced by these samples; in particular, decelerated protons (sample D) more effectively produce lattice strain within the thin film; in particular, the decrease of the strain in sample E could be ascribed to a weak annealing process due to a local heating of the substrate during irradiation. In sample D this effect is likely masked by the higher defect density induced by protons directly in the film (greater *dpa* values) and, especially, in the substrate (since protons implant closer to the film-substrate interface), both increasing the film's strain.

Sample	Hall bar	Fluence (10^{16} cm^{-2})	*dpa*	Inter-defect distance (nm)
A	A_0	0	0	---
	A_0.25	0.70	$2.5 \cdot 10^{-4}$	4.3
	A_0.99	2.80	$9.9 \cdot 10^{-4}$	2.7
B	B_0	0	0	---
	B_0.69	1.95	$6.9 \cdot 10^{-4}$	3.1
	B_2.27	6.40	$2.27 \cdot 10^{-3}$	2.1
	B_2.59	7.30	$2.59 \cdot 10^{-3}$	2.0
C (with 80 µm Al foil)	C_0	0	0	---
	C_2.30	2.68	$2.30 \cdot 10^{-3}$	2.1
	C_4.59	5.35	$4.59 \cdot 10^{-3}$	1.6
D_0	**---**	0	0	---
D_2.30 (with 80 µm Al foil)	---	2.68	$2.30 \cdot 10^{-3}$	2.1
D_4.59 (with 80 µm Al foil)	---	5.35	$4.59 \cdot 10^{-3}$	1.6
E_0	---	0	0	---
E_1.90	---	5.35	$1.90 \cdot 10^{-3}$	2.2

Table 6: Summary of the samples with the relative fluences, average displacements per atom (*dpa*) and distance between defects. Samples A, B and E were directly irradiated with 3.5 MeV protons, while samples C and D were irradiated with protons decelerated through the interposition of a 80 µm-thick aluminium foil. The inter-defect distance was evaluated by considering just stable Frenkel pairs defects and neglecting possible clustering and annealing effects. Samples D and E used for X-ray diffraction analysis both before and after irradiation were not patterned.

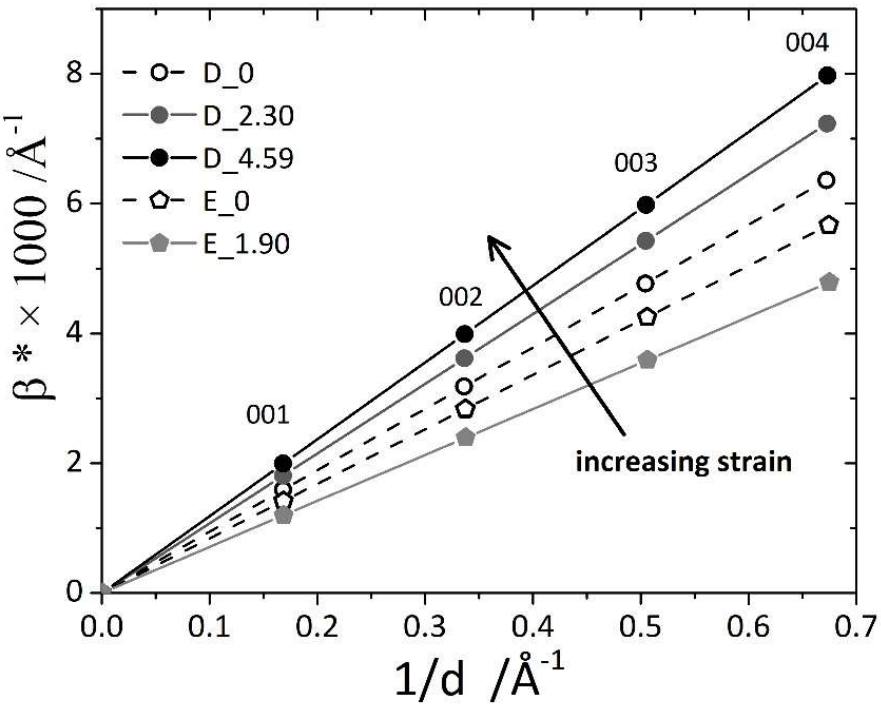

Figure 64: Superposition of the Williamson-Hall plots of the samples D and E before and after irradiation (β*: reciprocal integrated breadth of the diffraction line; d*: reciprocal interplanar spacing).

In Figure 65 we show as a reference the critical current density as a function of magnetic field up to 16 T measured on the pristine sample C_0 at 4.2, 8 and 12 K in PPMS system at CNR-SPIN Salerno. The J_c values for samples A_0 and B_0 are about 20% lower: at 4.2 K and 7 T J_c is ≈ $2 \cdot 10^5$ A/cm^2 for sample C_0 and ≈ $1.6 \cdot 10^5$ A/cm^2 for samples A_0 and B_0. The irradiated samples were always compared with their pristine reference sample, where pristine means a bar measured both before irradiation and after the irradiation process, during which that bar was kept shielded, in order to rule out any spurious or ageing effects. In Figure 66 and Figure 67 we report the J_c values as a function of the field for the patterns irradiated at the different fluences, where J_c has been normalized to the value of the pristine samples A_0, B_0 or C_0. The magnetic field was applied perpendicular to *ab* crystalline plane and the temperature was fixed at 4.2 K and at 12 K. Sample A (squares) and sample B (triangles) were measured up to 9 T, while sample C (circles) was measured up to 16 T. As it can be seen samples A and B show an improvement of J_c with the increasing dose. In particular, the bar B_2.27 shows an improvement of J_c of about 40% at 7 T and 4.2 K as compared to its pristine counterpart.

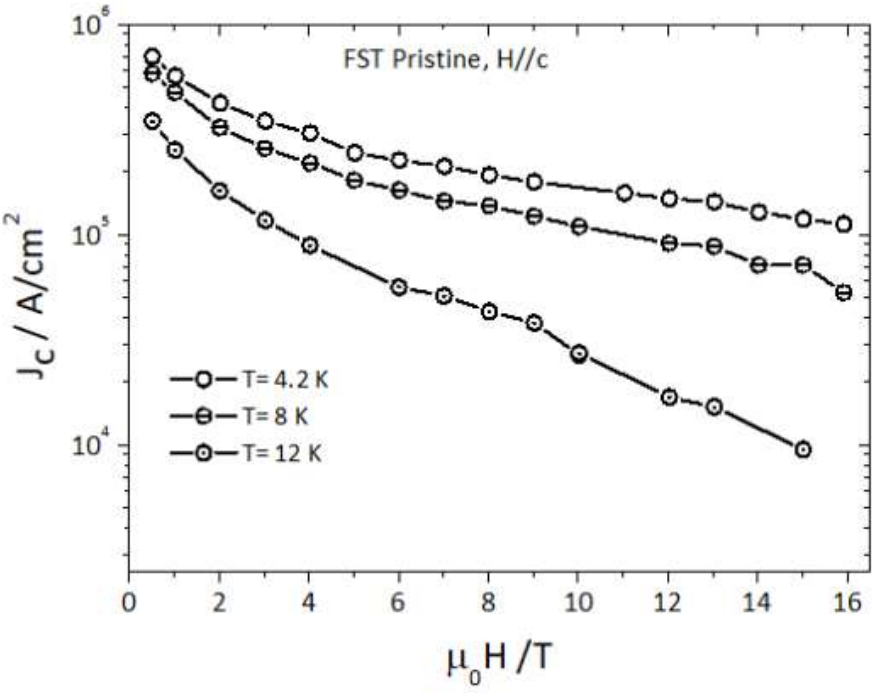

Figure 65: J_c of the pristine sample C vs magnetic field up to 16 T at 4.2, 8 and 12 K.

The most irradiated bar of sample B (B_2.59) is not reported at 4.2 K because J_c was too high to be measured for the current supply of the PPMS system. At 12 K, as shown in Figure 67, the most irradiated bar of sample B (B_2.59) shows an improvement of J_c of about 50% at 7 T. On the contrary, for sample C, an opposite trend is observed, namely the most irradiated bar C_4.59 shows the worst J_c both in self-field and in-field at all the investigated temperatures. The decrease of J_c at 7 T is of about 80% at 4.2 K and almost 90% at 12 K. Hence, from these plots, J_c does not seem to have a monotonic and unique response to irradiation: samples A and B show an enhancement of J_c with increasing dose of irradiation, whereas sample C shows the opposite trend. Moreover, we observe that at 4.2 K the in-field behaviour of J_c ratios can be considered flat for all the three samples in the investigated field range, while at 12 K J_c ratios increases with increasing field for samples A and B (where we observe an improvement of J_c with irradiation) and decreases with increasing field in samples C (where J_c decreases upon irradiation).

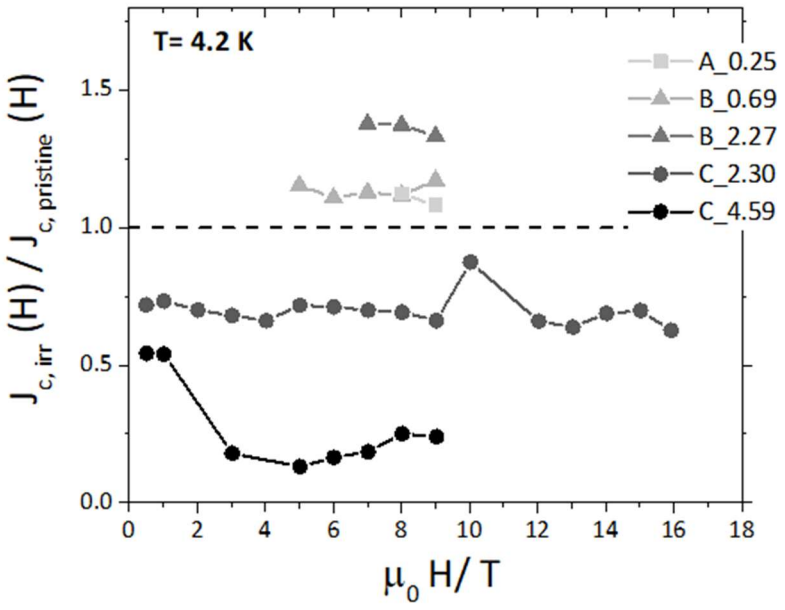

Figure 66: J_c vs magnetic field at 4.2 K for the different irradiated patterns normalized to the values of the relative pristine samples at the same fields.

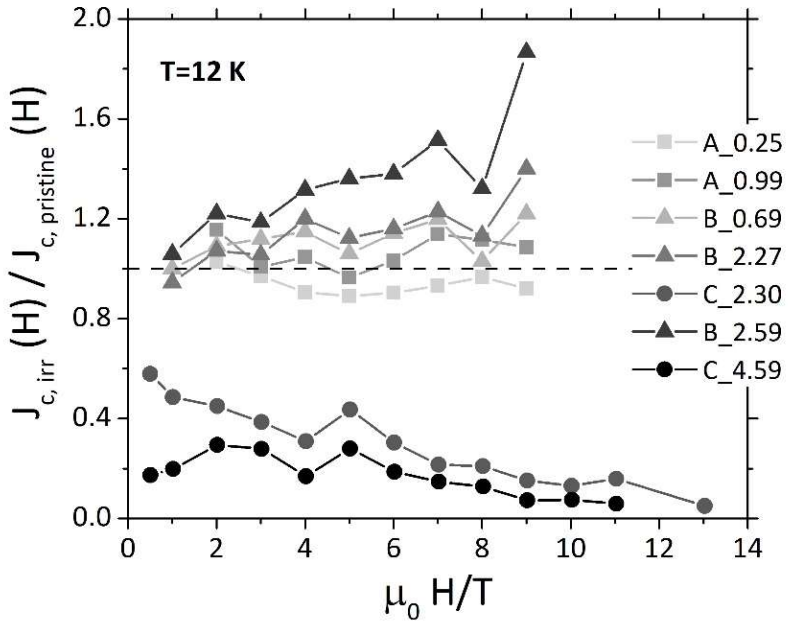

Figure 67: J_c vs magnetic field at 12 K for the different irradiated patterns normalized to the values of the relative pristine samples at the same fields.

For a better evaluation of the effects of proton irradiation on J_c, we analysed J_c values at fixed temperatures and fields as a function of the *dpa*, in order to take into account not only the number of particles that hit the target but also the expected damage they induced in the film in dependence on their energy. Figure 68 and Figure 69 show J_c values, normalized to the value of the corresponding

pristine samples A_0, B_0 or C_0, as function of *dpa* for all the irradiated bars at 4.2 K and 12 K and at 5 and 9 T. From such plots we observe an increase of J_c for *dpa* values up to about 0.002 relative to the bars irradiated on sample B: at 9 T J_c increases of 33% at 4.2 K (bar B_2.27) and 86% at 12 K (bar B_2.59). On the contrary, sample C shows a decrease in J_c for a similar *dpa*. This decrease reaches values of about 75% at 4.2 K and above 90% at 12 K and 9 T, when *dpa* is over 0.004 (bar C_4.59). This difference in the irradiation effects could be ascribed to the influence of the different defect distribution in the substrate, as discussed in the next section.

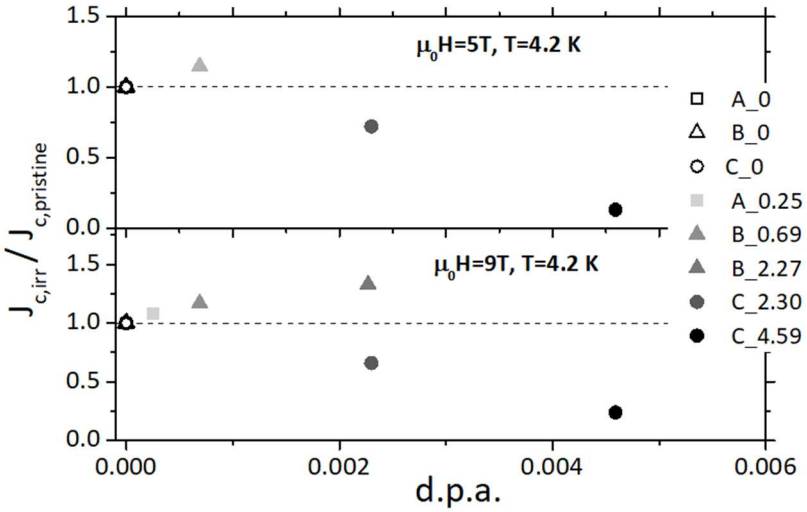

Figure 68: J_c of the irradiated bars normalized to the values of the relative pristine samples at 4.2 K and 5 T (upper panel) and 9 T (lower panel).

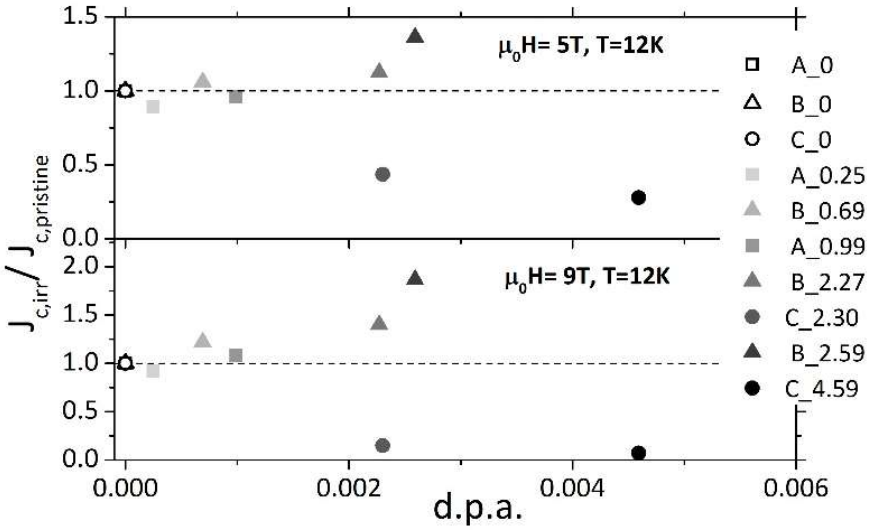

Figure 69: J_c of the irradiated bars normalized to the values of the relative pristine samples at 12 K and 5 T (upper panel) and 9 T (lower panel).

In order to evaluate the effect of irradiation on the critical temperature we performed resistivity measurements. In Figure 70 is shown the resistive transitions for all the bars of the three samples, where the resistivity is normalized to the value of the respective pristine samples at 20 K. The variations are very small for samples A and B. Only sample A shows a very little decrease of ρ(20 K) of about 5% upon irradiation. Sample C, on the contrary, shows a significant increase in the resistivity of about 20%.

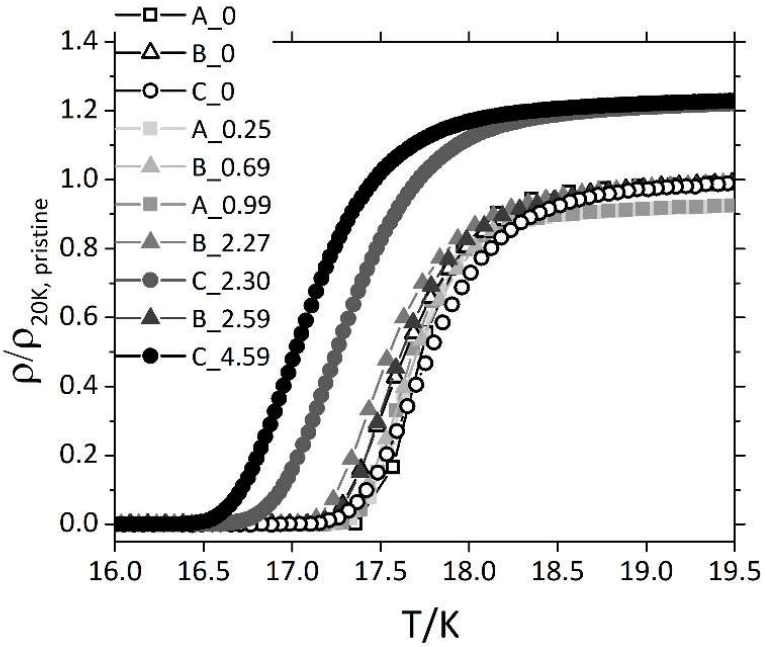

Figure 70: Resistive transitions for all the irradiated bars of samples A, B and C where the resistivity at 20 K for each bar is normalized to the resistivity of the relative pristine sample at 20 K.

In Figure 71 the resistivity in the normal state (20 K), the 90% of the resistive transitions in zero field and the ΔT_c (T_c(90%)-T_c(10%)) for all the irradiated bars is reported, all normalised to the pristine values. As already shown from the resistive transitions, there is no significant variation of the normal state resistivity nor in T_c or in ΔT_c in the irradiated samples A and B with respect to the relative pristine sample. In sample C, T_c decreases by about 0.6 K and, at the same time, the resistivity increases by about 20% upon high *dpa* irradiations.

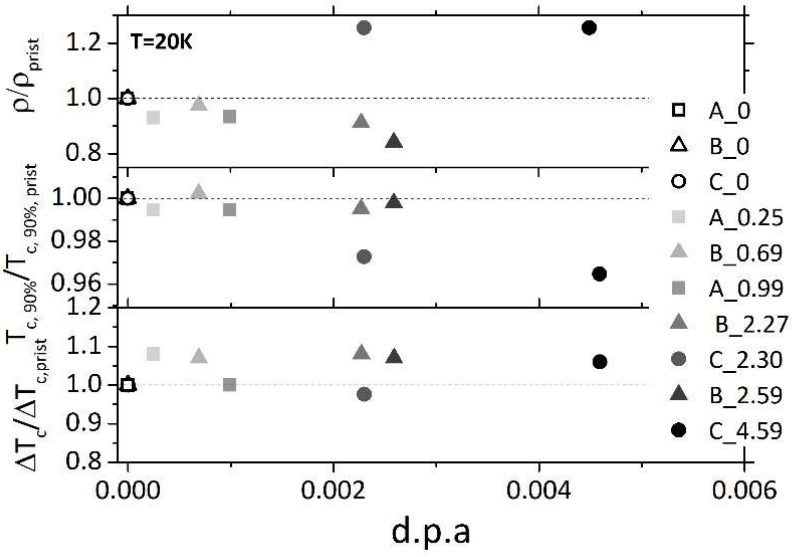

Figure 71: Resistivity at 20K (top panel), critical temperature (intermediate panel) and ΔT_c (bottom panel) as function of *dpa* All the quantities have been normalized to the corresponding value of the pristine sample.

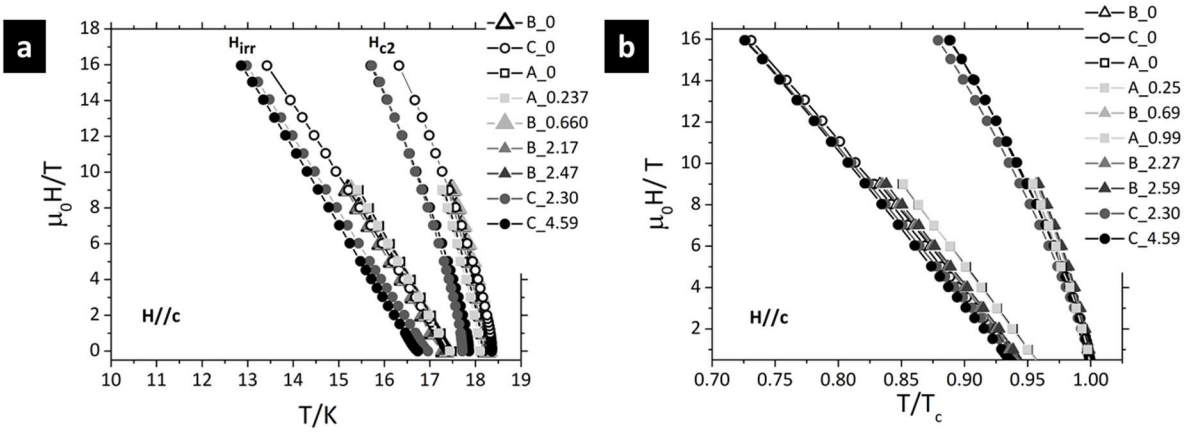

Figure 72: a) Upper critical field and irreversibility field as a function of temperature for all samples. b) Upper critical field and irreversibility field of all the bars as a function of the reduced temperature $t=T/T_c$ of the corresponding pristine sample.

From resistivity measurements in applied field it is possible to evaluate the irreversibility field H_{irr} and upper critical field H_{c2} using the criterion of 10% and 90% of the resistivity value in the normal state above the transition. In Figure 72 H_{c2} and H_{irr} for all the bars, evaluated with H // *c*, are reported. In the inset of Figure 72, H_{c2} and H_{irr} as a function of the reduced temperature of the corresponding pristine sample are reported. All the curves show very high slopes near T_c, as already reported for 11 thin films[36,57]. Irradiation does not change significantly the slope of H_{irr} and H_{c2} curves: indeed, the curves belonging to the same sample are superimposed over each other for samples A and B, while sample C only shows a slight decrease in T_c, as already mentioned above. In conclusion, the critical fields maintain the same slope as a function of the temperature regardless of different fluences and the presence of the aluminium foil. By contrast, the resistivity and the critical temperature stay substantially unaltered for samples irradiated without Aluminium foil, while the slowing down of

protons caused a resistivity increase of about 20% and a suppression in T_c of about 0.6 K. For comparison, a T_c suppression of 2 K has been reported in $Ba(Fe_{0.925}Co_{0.075})_2As_2$ single crystals irradiated with 3 MeV protons and a fluence of $1.2 \cdot 10^{16}$ cm^{-2} [81]and up to 4.3 K in $Ba_xK_{1-x}Fe_2As_2$ single crystals irradiated with 3 MeV protons and a fluence of $9.2 \cdot 10^{16}$ cm^{-2} [82]. Regarding the critical current density, the samples A and B irradiated directly under the 3.5 MeV proton beam, where the protons implant into the substrate several tens microns away from the film-substrate interface, were studied for *dpa* up to 0.0026. In these conditions, an enhancement of J_c upon irradiation was observed. For instance, we measured an improvement of J_c of about 40% at 4.2 K and 7 T and up to 50% at 12 K with respect to the pristine bars (see Figure 66 and Figure 67).

For sample C irradiated with the interposition of an aluminium foil, which was studied only for *dpa* higher than 0.002, J_c decrease after irradiation up to 80% at 4.2 K and of 90% at 12 K and 7 T. In samples irradiated without Al foil, the J_c never reaches a maximum; on the other hand, in samples irradiated with Al foil, J_c monotonically decreases. Hence, the apparent non-monotonic trend of J_c with increasing *dpa*, i.e. first increase and then decrease, appears only by joining data from differently strained samples, also because we did not perform experiment in the whole *dpa* range on a single sample. By comparing these two trends, it is possible to speculate that, not only the *dpa*, but also the position of the defects in the substrate can influence the properties of the film and therefore it is able to tune J_c. Indeed, the different behaviour observed in samples A and B with respect to samples C cannot be interpreted in terms of *dpa* alone. It appears that the interposition of a thin Al foil, which reduces the implantation depth of protons into the substrate, actually modifies the film properties via strain in a different way, depending whether the substrate is mainly damaged close to or far from the substrate-film interface. In other words, for equal *dpa*, the closer to the interface are the irradiation defects in the substrate, the larger is the strain in the film and the stronger is the detrimental effect on its superconducting properties. This scenario is supported by the XRD analysis; from which it appears that the shift of the implantation peak nearer to the interface causes an increase in the strain of the films. Noteworthy, the J_c enhancement upon irradiation is modest as compared to other IBS families. In ref. [67] it was pointed out that this can be ascribed to the lower depairing current in 11 IBS, which sets the magnitude of achievable currents. The moderate J_c enhancement can also be ascribed to the natural presence of pinning centres in FST thin films induced by the growth on the CaF_2 substrates [4], where J_c already reaches 10^6 A/cm^2, in self-field at 4.2 K, which is about 5% of the depairing current density J_d [67].The effect of irradiation in the same conditions (3.5 MeV protons), is modest: as a comparison, after irradiation, YBCO thin films show a suppression of J_c of about 20% for *dpa* as low as $2.04 \cdot 10^{-4}$ [83]. Generally, the low sensitivity of superconducting and normal state properties of this compound to irradiation may result from the balanced competition of positive and detrimental mechanisms. For example, the distribution of irradiation defects may create a coexistence of areas of tensile and compressive stress, having opposite effects on the superconducting properties, thus resulting in an overall net effect that is small. Only at the largest irradiation doses and in presence of a reduced implantation depth in the substrates that can amplify the irradiation-induced effect the detrimental mechanisms tend to prevail. This robustness of FST to irradiation damage is promising for application in magnets for high-energy accelerators.

4.3.3 Study of the anisotropy on Irradiated 11 thin films

Further characterizations were done on the most irradiated sample C to study the anisotropy of the superconducting properties. Anisotropy is a relevant property if the possibility to develop 11 superconducting magnets is considered. Higher is the anisotropy, the more complicate is the design of magnets. The anisotropy measurements were performed at SPIN-Salerno in a Cryogenic cryogen free cryostat equipped with 16 T magnets and a variable temperature insert (VTI) ranging from 1.6 K and 300 K. The sample holder can rotate along two perpendicular axes, one perpendicular to the plane of the sample holder (Φ) and the other parallel to the sample holder (θ) (see Figure 73).

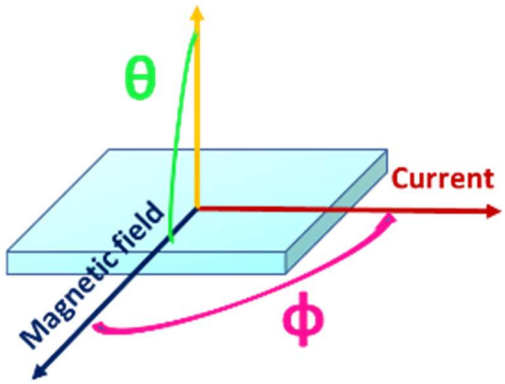

Figure 73: Schematic picture of the experimental geometry.

The measurements of resistance as function of temperature (Figure 74) [84] were done in two different configurations: magnetic field parallel to the c-axis (H//c) and magnetic field parallel to the ab plane (H//ab). As shown in Figure 74 the irradiation process causes an increment of the normal state resistivity as the proton influence increase. Moreover, a depletion of the T_c of about 0.6 K is reported, as previously observed from Figure 70. An enhancement of the anisotropy factor $\gamma_H = H_{c2}^{//ab}/H_{c2}^{//c}$ was also reported after the irradiation (Figure 75). An analysis conducted on the pinning activation energy as function of the applied magnetic field pointed out a progressive shift to higher values of the threshold field between two different pinning regimes as the proton fluence increases [84]. The anisotropy of J_c on sample C was also studied by Leo A et al [85], who measured several current-voltage curves. It was found that proton irradiation does not have effects on the critical current in the case of H//ab, while for H//c was observed a decrement of J_c as temperature increase and at high magnetic field.

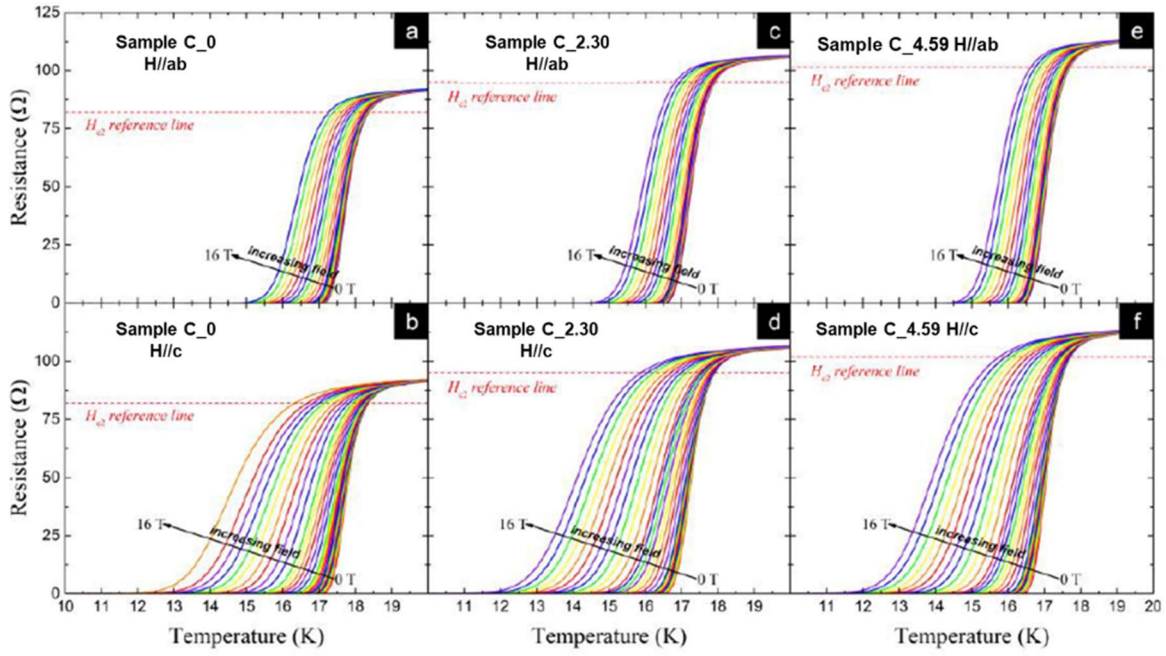

Figure 74: Resistance as a function of temperature in applied magnetic field for the hall bar C_0, C_2.30 and C_4.59 with H//ab (upper panel) and H//c (lower panel). The red dotted line marks the resistance value considered for H_{c2} estimation [84].

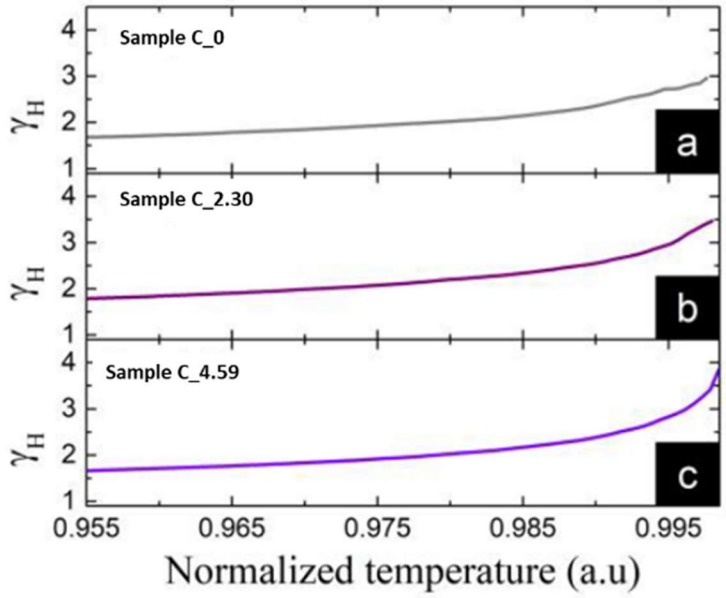

Figure 75: Anisotropy factor of three Hall bar of sample C [84].

Moreover, an higher proton fluence does not reduce further the J_c [85]. Because of the variation of critical current density also the anisotropy of the critical current is modified. Measurements of J_c as a function of the θ angle shows in Figure 76 reveals that both the pristine sample and the most irradiated samples shows a peaks of J_c for θ = 0° which correspond to H//ab, but for θ = 90° (H//c) the most irradiated sample shows a suppression of the J_c. From Figure 76 it is possible to see that the anisotropy factor γ_H

is almost constant for the pristine sample while for the irradiated sample it shows an increasing trend which is higher with the increasing magnetic field and the increasing temperature.

The suppression of J_c for H//c can be ascribed to an effect of the strain induced from irradiation in the film. From previous results it was concluded that the presence of the aluminium foil - and so the decelerated protons - can induce inside the sample an enhancement of strain. The trend of J_c (θ) could confirm the results reported in the Williamson hall plot (Figure 64), where the sample D, irradiated with the Al foil and comparable to sample C here analyse, shows an enhancement of the internal strain after irradiation. However, the suppression of J_c can also be ascribed to a change in the pinning centre as reported in [73] , even if in only one direction.

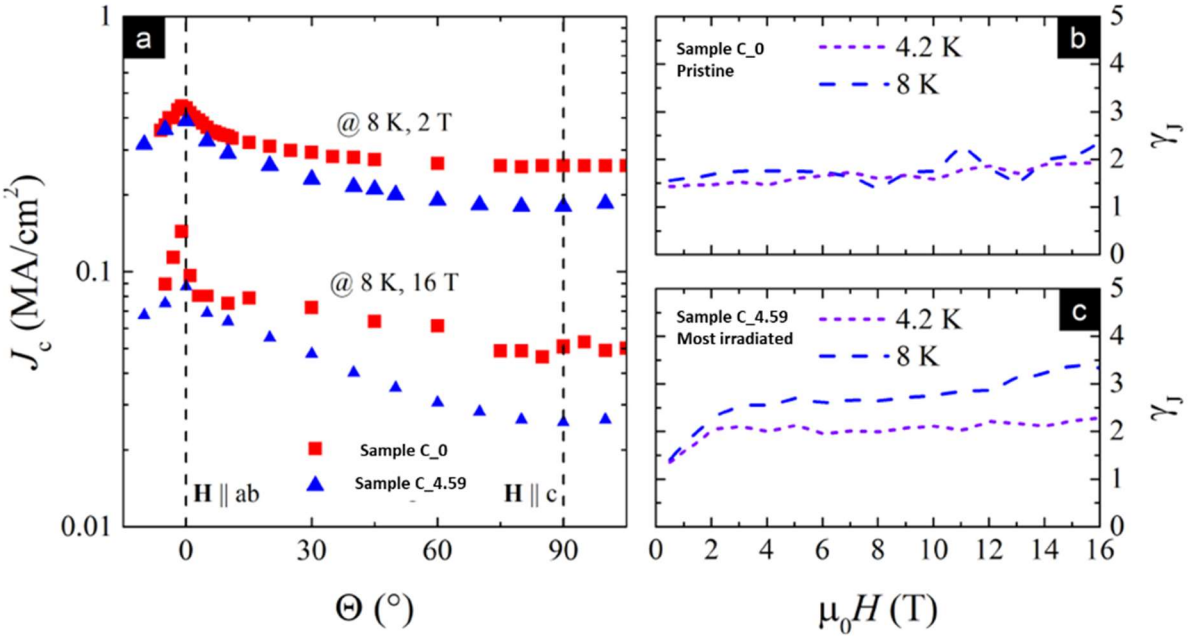

Figure 76: (a) The critical current behaviour as a function of the angle between magnetic field direction and the c-axis of the thin film. (b) Pristine hall bar anisotropy factor dependence on the applied magnetic field at two different temperature values (short-dashed line is for 4.2 K, long dashed line is for 8 K). (c)Sample C_4.59 (most irradiated) at the same two temperature values [85].

The effect of irradiation on pinning can be appreciated by evaluating the pinning force F_p as function of the applied magnetic field. Following the Dew-Hughes model the normalized pinning forced can be defined:

$$f_p = C \times h^p (1-h)^q$$

Equation 3

Where $f_p = {F_p}/{F_{p,max}}$ ($F_{p,max}$ is the maximum of the $F_p(\mu_0 H)$ curve), $h = {H}/{H_{irr}}$ (in the original work of Dew-Hughes H_{c2} was present, this is a modification introduced for the first time to study the pinning in the cuprates) and the values of the constants C, p and q are related to the nature and the dimensions of the pinning centres.

The f_p curves for pristine sample and the most irradiated sample are shown in Figure 77. The detailed parameters of the fit can be found in the reference [85]. As can be seen the irradiation does not change the pinning properties of the samples, this is confirmed from the absence of a differences between the case H//c and the case H//ab.

From this analysis it is possible to conclude that the suppression of J_c for H//c can be completely ascribed to the presence of strain inside the lattice of the irradiated sample.

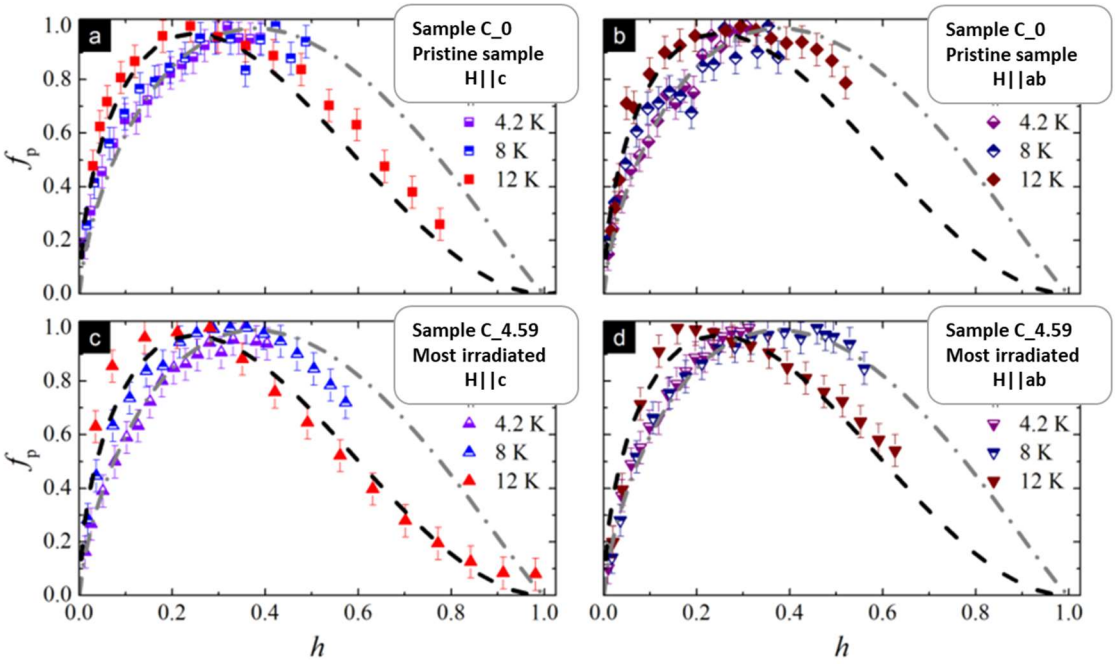

Figure 77: The normalized pinning curve as function of the magnetic field at three different temperature values for: (a)C_0 Pristine sample in field applied along the film c-axis, (b)C_0 Pristine sample in field applied along the film ab-plane, (c) Sample C_4.59, the most irradiated, in field applied along the film c-axis, and Sample C_4.59, the most irradiated in field applied along the film ab-plane. In all four panels, the dashed line is related to the curve resulting from Dew-Hughes fitting procedure with two contributions, while the dot-dashed line is related to the curve resulting from a standard Dew-Hughes fitting procedure [85].

4.3.4 Sub-MeV proton irradiation of 11 thin films

Samples F and G were directly irradiated with 0.5 MeV protons (parallel to the c axis of the film) with AN 2000 accelerator of INFN of Legnaro. As previously described for high energy proton irradiation, single Hall bars or groups of Hall bars were selectively irradiated with different fluences. Table 7 summarises the irradiation fluences of all the different Hall bars of the new samples, and the corresponding calculated *dpa* values. Hall bars, irradiated with different fluences, are indicated by the same convention introduced for the samples irradiated with high energy protons. Also, in this case the details of the irradiation experiment were guided by previous accurate simulations of the damage induced both in the film and in the substrate, obtained by the Monte Carlo code SRIM. Protons with E= 0.5 MeV crossed the films and were implanted into the substrate, at a depth of about 4.5 µm (Figure 78).

Sample	Hall bar	Fluence (10^{16} cm^{-2})	Displacement per atom (*dpa*)
F	F_0	0	0
	F_0.25	0.12	$2.5 \cdot 10^{-4}$
	F_0.69	0.32	$6.9 \cdot 10^{-4}$
	F_0.99	0.46	$9.9 \cdot 10^{-4}$
	F_2.28	1.06	$2.28 \cdot 10^{-3}$
	F_4.58	2.13	$4.58 \cdot 10^{-3}$
G	G_0	0	0
	G_0.99	0.46	$9.9 \cdot 10^{-4}$
	G_11	5.11	$11.0 \cdot 10^{-3}$

Table 7: Summary of the Hall bars of samples F and G with the relative fluences and average *dpa*.

The further reduced energy of the protons allows the implantation of the defects closer to the interface between film and substrate varying from the previous 86 µm for direct irradiation with 3.5 MeV protons and the 21 µm obtained protecting the sample with an aluminium foil during the irradiation with 3.5 MeV, to a depth which is one order of magnitude lower than the previous with 0.5 MeV protons.

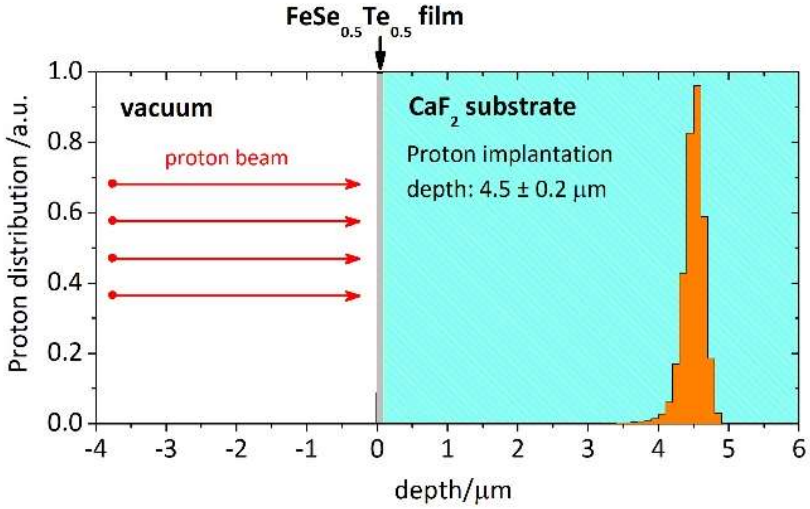

Figure 78: SRIM simulation of the effects of 0.5 MeV proton on the sample. The grey band correspond to FST thin film while the light blue region corresponds to the substrate.

This significant variation of the penetration depth of the protons is expected to create very different effects on the properties of the samples. Furthermore, the fluences used for irradiate samples F and G were calculated in order to obtain the same *dpa* previously explored with high energy protons (Table 7). Figure 79 and Figure 80 show the critical current measurements performed on sample F and G at 4.2 K and 8 K.

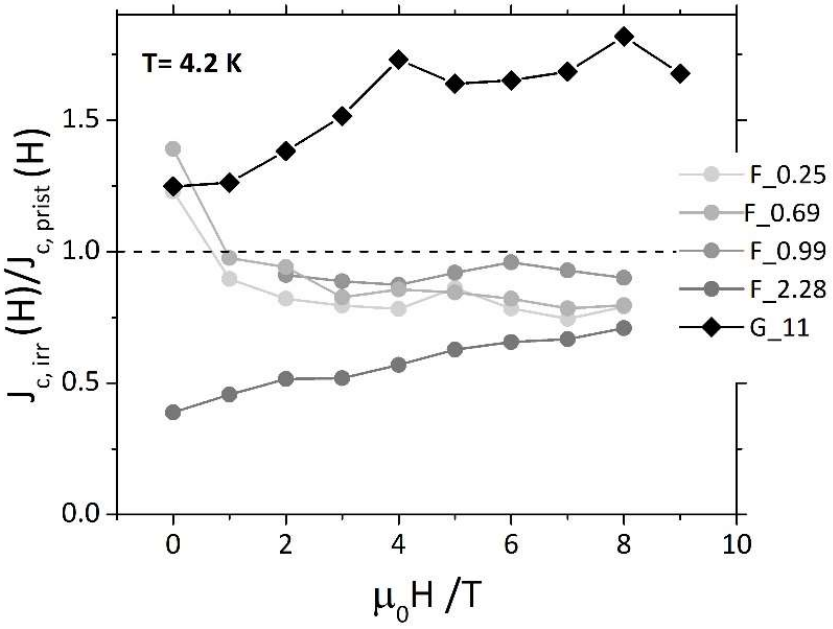

Figure 79: J_c vs magnetic field at 4.2 K for the different irradiated patterns normalized to the values of the relative pristine samples at the same fields.

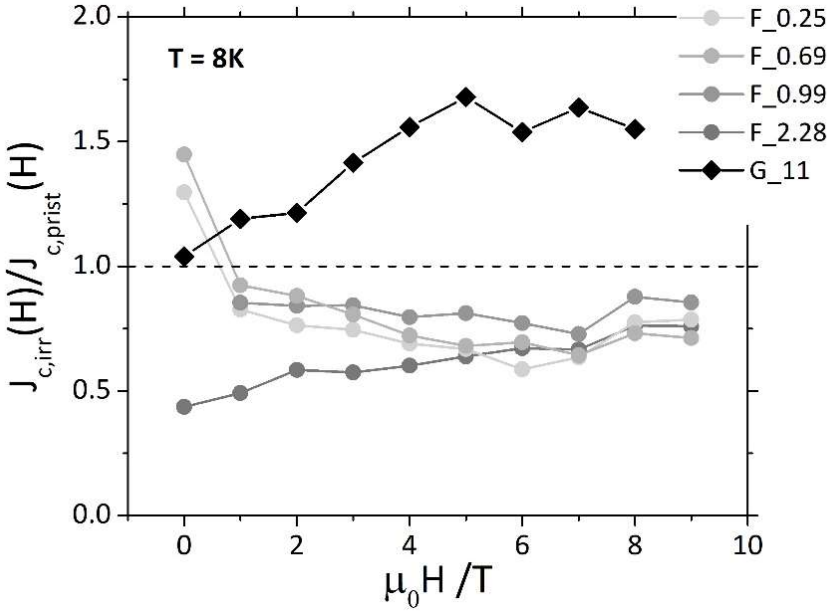

Figure 80: J_c vs magnetic field at 8 K for the different irradiated patterns normalized to the values of the relative pristine samples at the same fields.

To better highlight the effect of the irradiation on samples the J_c curves were normalized to the J_c of the pristine Hall bar (F_0, G_0). As can be seen from Figure 79 and Figure 80, sample F shows a J_c that for low magnetic fields slightly decrease and for higher magnetic field remain stable or even shows a slight increase with increasing field and this effect is more remarkable for high fluence (darkest curve) and high temperature. The increasing of J_c with the magnetic field is strongly evident in sample G, where an increment of J_c of about 60% is reported at 8K and 5T. The growth of J_c with magnetic field is an effect that was never be observed in irradiation with 3.5 MeV, with by Al foil, and which can be considered intermediate between samples irradiated directly with high energy protons and these sample irradiated with sub-MeV protons since the penetration depth in the case of sample C is halfway(see previous chapter and [86]). However, a similar effect was observed in sample B of the previous chapter which was irradiated without the Al foil.

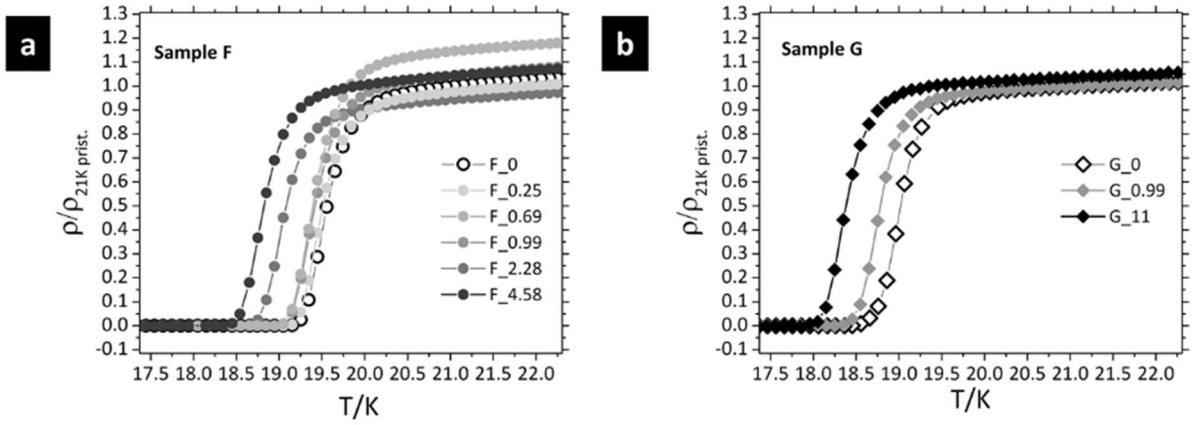

Figure 81: Resistivity curves of sample F(a) and sample G(b) samples normalized to the resistivity of each pristine sample at 21 K.

The increment of J_c can only be ascribed to the presence of pinning centres inside the film which are generated by irradiation. Sub-MeV proton irradiation, probably, causes inside the film the formation of a pinning landscape of defects which is not present in the samples irradiated with 3.5 MeV as previously discussed [84,85]. Figure 81 shows the resistive transition of the irradiated sample normalized to the resistive of the pristine sample at 21 K in order to compare the effect of irradiation not only on the T_c but also on the resistivity of the normal state. For both sample F and sample G a decrement of T_c with the increasing *dpa* (Figure 81 a and b) is reported, probably for the strain induced in the lattice by irradiation that could be higher than the reported for films irradiated with high-energy protons. Moreover from Figure 81 we can observe that the two pristine sample have a slight different T_c, but this difference is inside the normal variability between two different films, furthermore an enhancement of the resistivity in the normal state after irradiation was observed for sample F. H_{c2} and H_{irr} are unaltered after irradiation as already reported for sample C [86], as shown in Figure 82. These results on sub-MeV proton irradiation are very recent, and not complete, further irradiation experiments and further analysis regarding the pinning properties have to be done.

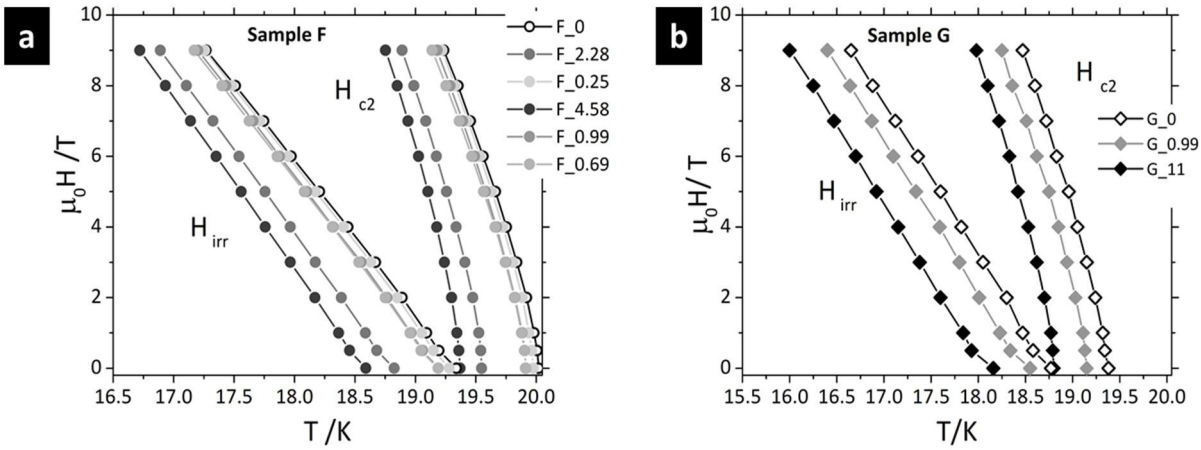

Figure 82: Upper critical field and irreversibility field as a function of temperature for sample F(a) and sample G(b).

From the experiment of proton irradiation on FST thin films we can conclude that non only the fluence and consequently the *dpa* play an important role but a very important parameter is the penetration depth of the protons i.e. the depth at which the protons create the defects. This is a very important aspect to consider for further studies considering that the final goal is to evaluate the applications of the phase FST as coated conductors for the development of high field magnets. It is possible to predict that changing the substrate, the effect of irradiation could completely change even if the superconducting phase is the same. Moreover, also every possible buffer layer will play a role in terms of the effect of irradiation on the superconducting properties of the film. However, even if only proton irradiation is considered so far, FST thin films have proved a significant resistance to irradiation becoming interesting for the applications in harsh environments.

5 CONCLUSIONS

The IBS recently discovered, which exhibit relatively high critical temperature T_c and huge upper critical field H_{c2}, have proved to have great potentiality for high field applications. IBS thin films have been successfully grown on single crystalline substrates and on technical metallic templates made via IBAD and on RABiTS already available for the deposition of YBCO, showing values of critical current densities J_c as high as 10^5 A/cm^2 up to 30 T. The route to the realization of long conductors is still long. In IBS the exponential decay of J_c across misoriented grain boundaries seems to be less severe than for YBCO, the processing temperature is much lower than for YBCO and does not require oxygen: Therefore, thinner and less complicated structures are expected to be suitable, significantly reducing the complexity and the manufacturing cost of IBS CC. Another important aspect, beside the fabrication of a suitable conductor that needs to be considered in view of high-field applications, is the effect of irradiation which is necessary to test the suitability of a conductor for operation in a radiation environment, such as fusion or accelerator magnets.
In this context my thesis aims to study the possibility to employ the 11 phase for applications in high magnetic fields. The work started from the long-lasting experience of the CNR Spin Genova group on the deposition with PLD of 11 thin films and with this thesis the activity moved forward studying the development of suitable FST conductor, employing the CC technology and the proton irradiation of FST thin films deposited on CaF_2 single crystals. These two activities are strongly connected both because they are based on the fabrication of FST thin films with the PLD on different substrates, but also because they are two main aspects that must be addressed in order to evaluate the possibility to use IBS conductors in a high magnetic field and harsh environment such as particle accelerators. The thesis is divided in two main sections:

- The first part aiming to develop a scalable method to produce 11 CC in a simple a cost-effective way, employing RABiTS substrates with simple architecture.
- The second part is focused on the study of the effect proton irradiation on 11 thin films deposited on CaF_2 single crystals.

In the first part of the thesis, the deposition technique of 11 thin film is present. Starting from the deposition of 11 thin films on CaF_2 single crystalline substrates with optimized parameters, the evolution from thin films on single crystal substrate to thin films on metallic templates is not obvious and requires preliminary studies to prove the possibility to obtain high quality thin films even if the substrate is not optimal as is a single crystal. In particular, problems related to film thickness, thermal expansion of the substrate and crystalline match between substrate and film were successfully addressed starting from the optimization of the process on single crystal and then transferring the process to the templates. After the optimization of the thin film deposition, the feasibility of producing cost effective 11 CC was demonstrated, using in-house manufactured substrates and substrates produced at ENEA Frascati Centre. In-house manufactured substrates were produced starting from commercially available Ni-alloy rods: the first one was a biaxially textured Invar 36 tape with an out-of-plane and an in-plane orientation smaller than 10°. Despite the good orientation of the films deposited on Invar, they do not show a superconducting transition. STEM analysis performed on a cross-sectional lamella prepared by FIB revealed local oxidation of the substrate at the interface with

the film and significant Ni diffusion from the substrate to the film. Therefore, the necessity of a buffer layer which can act as a chemical barrier between film and metal came up. Many different buffer layers were deposited on the Invar 36 substrate, and in parallel the possibility to employ a native passivating chromium oxide layer as chemical barrier was demonstrated developing Hastelloy C-276 substrates. Moreover, thanks to a collaboration with ENEA centre of Frascati 11 CC were developed employing NiW5% substrates from EVICO with different oxides buffer layers deposited at ENEA's laboratory obtaining a J_c of 1.7 10^5 A/cm^2 (at 0T and 4.2K) with a CeO_2 buffer layer.

In parallel, in collaboration with Politecnico of Torino, the effects of 3.5 and 0.5 MeV proton irradiation on FST thin films grown on CaF_2 were explored. The performed study showed that the effect of proton irradiation on superconducting properties of the 11 thin film is generally small compared to the case of other IBS. The irradiation effect is more evident on the critical current density J_c, while it is minor on the transition temperature T_c, normal state resistivity ρ, and on the upper critical field H_{c2} up to the highest fluences explored in this work. Moreover, it was discovered that the influence of proton irradiation on the superconducting properties is not only proportional to the fluence of irradiation but it is also strongly correlated to the implantation depth of the defects inside the film (i.e. the depth at which the protons create the defects) which can be tuned by changing the energy of the impinging protons. This result evidences that possible modifications induced by irradiation in the substrate may affect the superconducting properties of the film via lattice strain. From the conducted experiments, is therefore, possible to conclude, that the substrate plays an important role as well as the fluence. Future experiments of irradiation on CC require therefore, an extensive study of the role of every single part of the CC (i.e. metal, buffer layers, and film), on the final properties of the tape.

The results obtained in this thesis, seem to very promising. The possibility to produce 11 CC with simple and scalable method was demonstrate as well as the robustness of the 11 phase to irradiation-induced damage, making 11 phase a promising compound for the fabrication of magnets for high-energy accelerators.

APPENDIX - DEVELOPMENT OF 122 EX-SITU PIT WIRES FOR HIGH FIELD APPLICATIONS

In this section the work performed during my thesis on the development of 122 ex-situ PIT wires is presented. In the first section 1A a brief overview of the state of the art is presented while the second section A2, describes the experimental work performed during my thesis. The aim is to develop a PIT ex-situ process scalable to long sizes to realize Ba-122 wires and tapes. Different deformation processes, i.e. groove and flat rolling, swaging and drawing, were combined with the aim of densifying the superconducting core, without any additional pressure. The project started a few months ago and the results showed in this appendix are reported to highlight the possibility to obtain high quality cost-effective IBS conductors with different techniques.

1A. IRON BASED POWDER IN TUBE WIRES AND TAPES

PIT process is more attractive in respect to the CC technology to produce conductors for applications since it is a low-cost process and easy to realize. A typical PIT process is shown in Figure A 1: at first, the powders are packed into a suitable metallic sheath; then the as obtained composite wire is cold worked in order to compact the powders and give to the wire the final shape, finally the wire is subject to heat treatment. The PIT method can be *ex-situ* if the synthesis of the superconducting compound occurs before filling the metallic sheath. In the *in-situ* PIT method, conversely, the powders are composed of precursor of the superconducting phase and in this case the heat treatment does not only sinter the powders but also react them obtaining the superconducting phase.

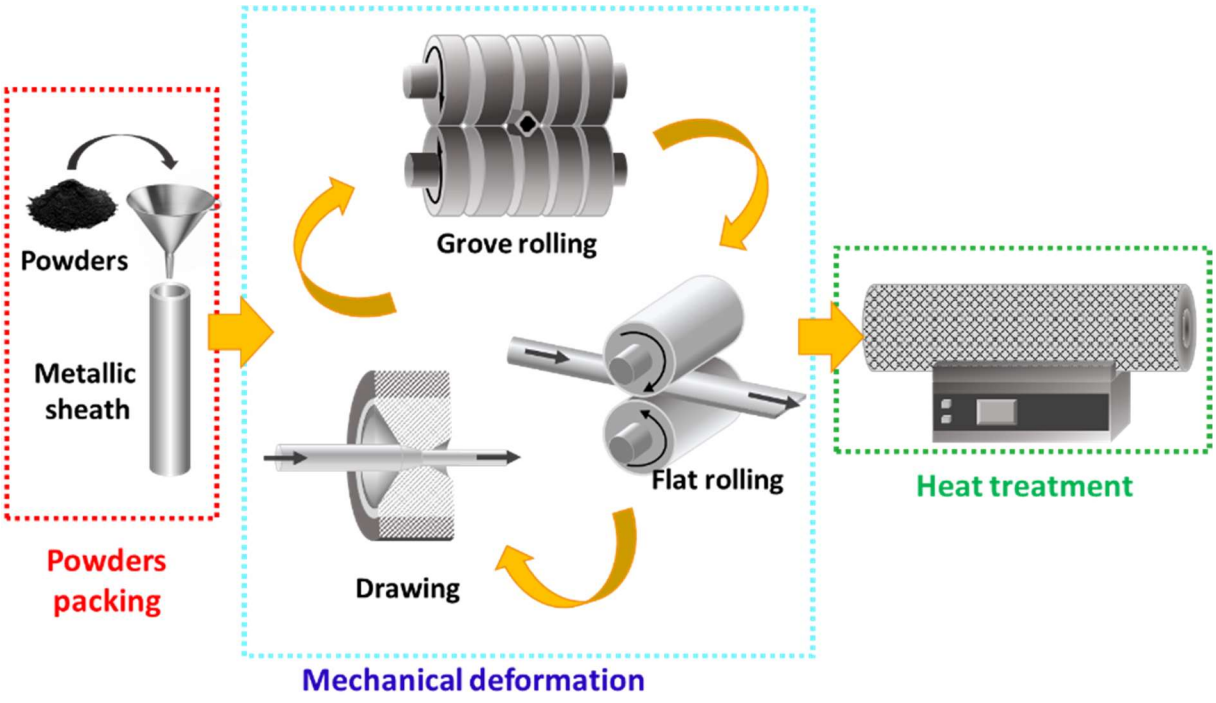

Figure A 1: Schematization of the Powder in Tube process

For high-field applications, not only a high transport current is necessary but is also important to develop wires and tapes with enough length for cable fabrications and coil winding. Compared to the CC technology, the PIT method is technically simpler, with low cost of productions and high production efficiency. The CC technology allows the production of monofilamentary tapes with a maximum length of many hundreds of meters (< 300 m for YBCO) and the junction between the tapes is a complex issue, while the PIT method is used to produce Kilometres of wires but it is also more flexible for making multifilamentary conductors with various architecture.

Soon after the discovery of IBS the first 1111-type IBS wires were made with the *in-situ* PIT method [87,88] and, in 2009, 122-type [89] and 11-type PIT wires [90] were reported. However, the *in- situ* PIT method causes a high phase inhomogeneity and porosity inside the wires because of the presence of volatile elements such as As, F and K that not react properly during the heat treatment, causing a low transport current. Better results were obtained using an *ex-situ* PIT method, with a significant improvement of the homogeneity of the wires and consequently of the transport current [91,92]**.** Another problem related to the fabrications of IBS PIT wires is the selection of the sheath materials. Various sheath materials were employed to fabricate 1111-type and 122-type IBS wires and tapes, including Nb, Ta, Fe, and Ag [93]. However, a chemical reaction between the sheath and the superconducting phase was always observed, causing a non-superconducting layer at the interface between powders and sheath. The only sheath material which does not react with the powders is Ag [94], however, it is now the only material used to produce 122-type PIT wires and tapes. Ag can be also used as internal sheath, with an outer sheath of another material with higher mechanical properties. 122-IBS wires and tapes with composite sheaths including Cu/Ag [95–97], stainless steel (SS)/Ag [98,99]and Ni/Ag [100] were developed. Recently, Cu and Fe have also appeared as strong alternatives when the final heat treatment time is short [101]. Because Cu is less expensive and has better deformation properties than Ag, it remains an interesting alternative for industrial applications [102]. Regarding the 11-type PIT wires the unique material compatible as sheath is Fe, but Fe can diffuse during heat treatment inside the superconducting core and the excess of iron causes the suppression of superconductivity [43]. Fe sheath also allows a PIT based diffusion process, where Fe near the inner surface of the sheath and the Se and Te (for the *in-situ* method) or the $FeSe_xTe_{1-x}$ powders (for the *ex-situ* method) form the 11 phase by chemical reaction during the heat treatment [103]. Most of the work on IBS -PIT wires and tapes was carried out on the 122 family which has an anisotropy comparable to the 11 and it has a T_c up to 38 K.

Figure A 2 shows the improvement of J_c of IBS wires and tapes developed using the PIT method. The critical current density of 122-based superconducting tapes has exceeded 10^5 A/cm^2 at 4.2 K at 14 T [104] which is the threshold J_c value of superconducting wires and tapes for practical application, demonstrating their excellent potential for high-field applications. From Figure A 2 is possible to notice that the in-field J_c values of 1111- and 11-type wires are still too low, e.g., more than 2–3 orders of magnitude lower in the high-field region than those of 122 wires, suggesting the large difficulties in wire fabrication for both 1111 and 11 families. The highest transport J_c above the practical level has been achieved by hot or cold uniaxial pressing combined with a flat-rolling process [105,106]. The flat rolling and the applied external pressure, cause a well coupling of grains, an increment of the Vickers hardness (H_v) which is used as an indication of mass density, and an increment of the texturing of the superconducting grains inside the tape, overcoming the problems of the weak link GB.

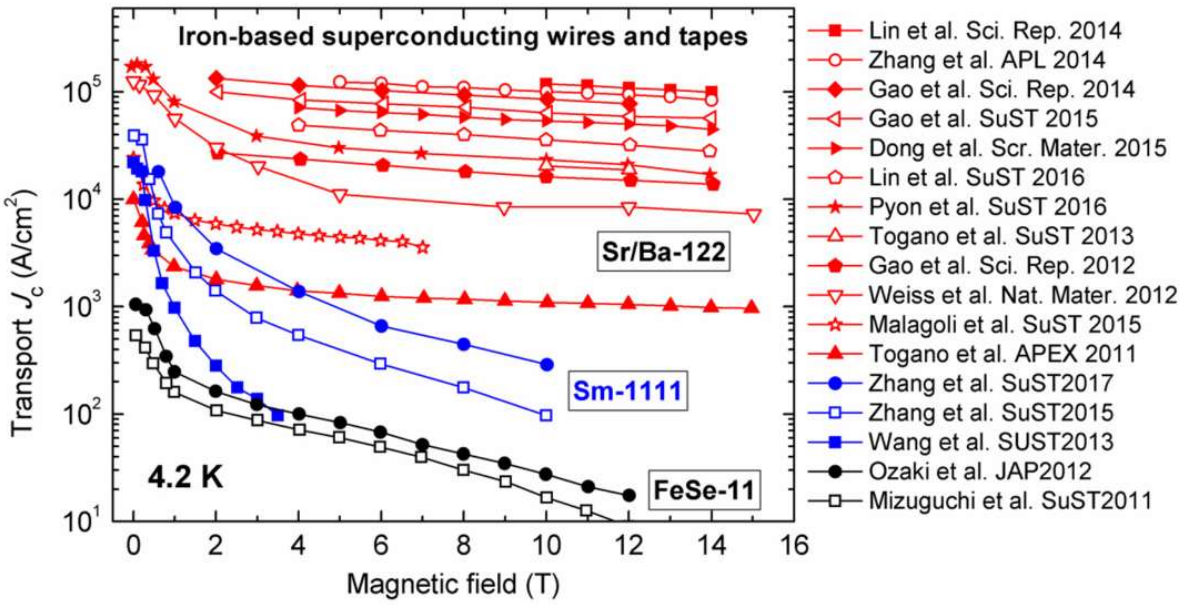

Figure A 2: Transport J_c at 4.2 K as a function of applied magnetic field for PIT-processed 122, 1111, and 11 wires and tapes [16].

By using an optimized hot-pressing process to achieve a higher degree of grain texture, the transport J_c was further increased to 1.5×10^5 A/cm^2 with a small J_c anisotropy of 1.37 at 4.2 K and 10 T in Ba-122 tapes, which exhibit very weak field dependence up to 33 T[107]. However, a scalable process based on drawing and rolling is still a more practical route for the fabrication of long-length wires and tapes. Drawing wires, deformed in flat tapes in the last part of the deformation process shows a transport J_c of about 3.31x10^4 A/cm^2 at 4.2 K and 10 T. For flat-rolled tapes, a multi-pass rolling process is usually employed. The rolling deformation technique was studied systematically with respect to the number of rolling passes. It was found that the transport J_c is not sensitive to the number of rolling passes, while the width of the tapes, the area of the superconducting core and the core density are increased by decreasing the number of rolling passes [108]. Moreover, a series of cold work processes, including groove rolling, drawing, drawing + flat rolling, drawing + groove rolling, and groove rolling + flat rolling was investigated for Ba-122 ex situ PIT wires and tapes [100].

Fe/Ag composite sheathed multifilamentary Sr-122 IBS wires and tapes with up to 114 filaments were also fabricated based on the PIT method [109] (Figure A 3). A high J_c of 3.6×10 ^{4} A/cm^2 (4.2K,10T) was achieved in Monel/Ag composite sheathed seven filament hot-pressed Sr-122 tapes, suggesting the great potential of Monel/Ag composite sheaths for the development of high strength and high J_c performance in IBS wires and tapes for high-field applications [110]. In 2017 the first 100 m of 122-type PIT wires was realized, demonstrating the potential for large-scale application[111]. A 115 m long seven-filament Sr-122/Ag tape showed a uniform J_c distribution along the tape with a minimum J_c of about 1.2x10^4 A/cm^2 at 4.2K and 10 T, which was very recently increased above 2x 10^4 A/cm^2.

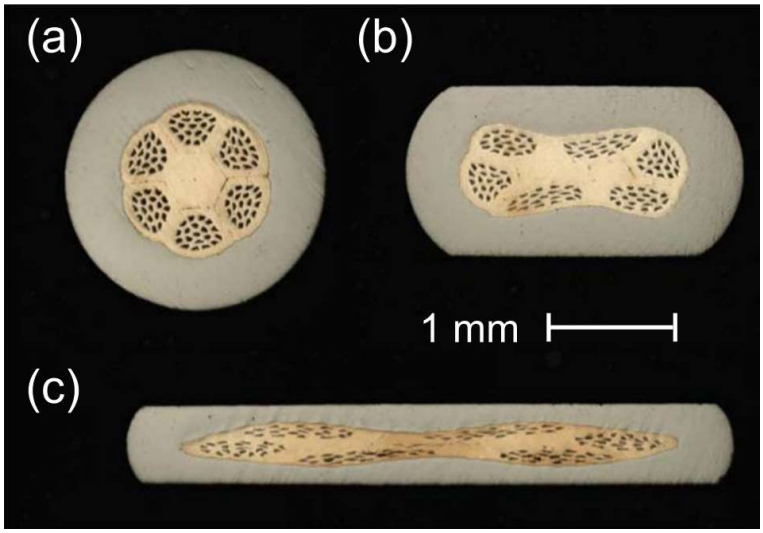

Figure A 3: Optical images of the transverse cross-section of 114-filament Sr-122/Ag/Fe (a) wires of 2.0 mm diameter, and tapes of(b) 1.0 mm and (c) 0.6 mm thicknesses, showing the rearrangement of the Sr-122 filament during flat rolling

2A. DEVELOPMENT OF 122 WIRES AND TAPES

2A.1 Preparation and analysis of the powders

The development of the wires started with in-house synthesized powders developed at SPIN by A. Provino in the framework of the collaboration with CERN (ADDENDUM FCC-GOV-CC-0086 to the Memorandum of Understanding for the FCC Study). The aim of the work was to identify a reliable, reproducible and efficient synthesis route to prepare massive samples (up to 4-5 g) of the superconducting phase $Ba_{1-x}K_xFe_2As_2$, in polycrystalline form and with composition $Ba_{0.5}K_{0.5}Fe_2As_2$. Starting from high purity reagents (Ba 99.5 wt.% purity; K 98.0 or 99.99 wt.% purity; Fe 99.9 wt.% purity on metal basis, equivalent to 99.5 wt.% purity; As 99.99+ wt.% purity), a route has been developed to synthesize polycrystalline samples which requires three steps:

Preparation of the precursor FeAs: The binary precursor FeAs is prepared by vapor-solid reaction between Fe powder and As ground in fine grains at a temperature of 900°C over 3 days cooled down to room temperature without quenching. The product obtained is a stable material almost single phase FeAs (orthorhombic FeAs structure type, *oP*8, *Pnma*). The material is grey in color, slightly sintered, compact and porous; it can be easily ground into fine powder.

Synthesis reaction between Ba, K, FeAs: Ba and K metals in elemental form and in small pieces are placed and slightly pressed to the bottom of an Al_2O_3 crucible. FeAs, in weighed amount to result in a given stoichiometry $Ba_{0.5+x}K_{0.5+x}Fe_2As_2$ (x = over-stoichiometry in both Ba and K) is added on top of Ba and K pieces and set to possibly completely cover these two metals. The system is then placed inside a steel crucible and stored under pure Ar, and then the crucible is welded. The crucible is then sealed under vacuum inside a large quartz tube and transferred into a vertical resistance furnace for the synthesis heat treatment. The reaction needs many steps that comprises a heating up at 150°C above the melting temperature of K, and heating up above the melting temperature of Ba, and a final heating at 850°C which lasts 3-5 days.

Sintering of the (Ba,K)Fe_2As_2 pellet: The above well mixed and homogenized material is converted into pellet by using a stainless-steel die and a hydraulic press. The pellet is then transferred into a new Al_2O_3 crucible and closed in a new stainless-steel container by welding under Ar flux. The steel crucible sealed under vacuum in quartz tube and the whole arrangement was heated up at 850°C and held at this temperature for 3-5 days. The final sample as pellets (Figure A 4) appears dark grey in colour, they are dry, compact, but brittle.

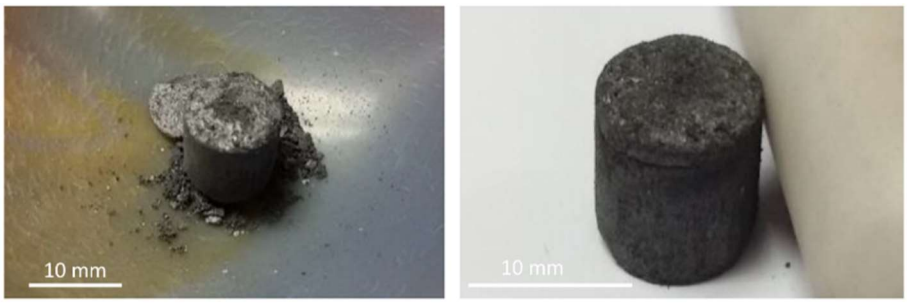

Figure A 4: The final sample of Ba-122 as pellet.

The best samples obtained through this procedure are almost single phase $Ba_{0.6}K_{0.4}Fe_2As_2$, as can be seen from the Rietveld refinement in Figure A 5. Moreover, the narrow shape of the peaks in the XRD is the proof of a homogeneous composition. Magnetic measurements reveal that powders have a T_c as high as 38 K (Figure A 5), which is comparable to other data reported in literature.

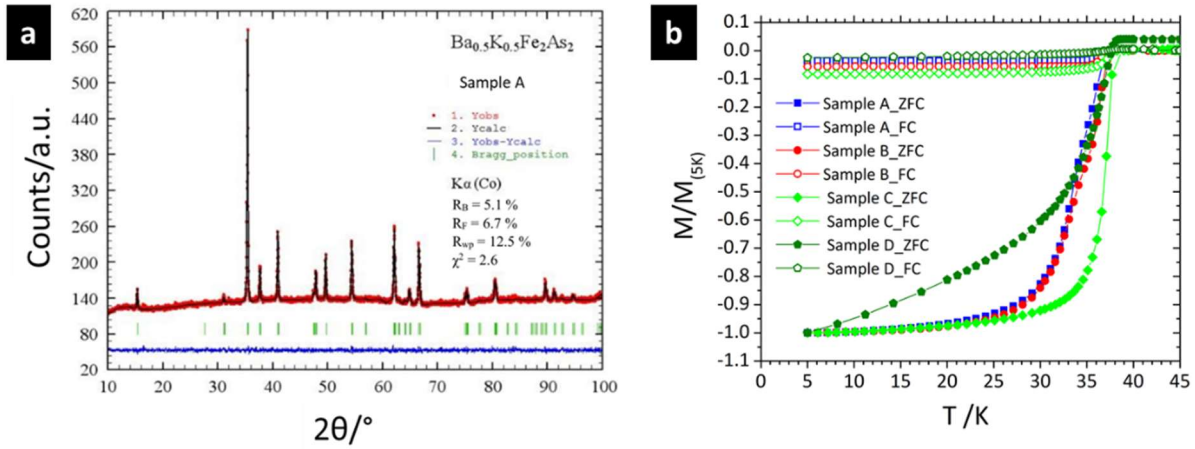

Figure A 5: Rietveld refinement (a) and magnetic measurements (b) made on different batch of the Ba-122 powders obtained with the previous described method.

The powders were analysed with the SEM microscope with punctual analysis and elemental mapping to examine their chemical composition and homogeneity before the production of the wire. The pellets reveal a global composition near to $Ba_{0.6}/K_{0.4}$ and some Ba-oxides restricted in some zones of the pellet (Figure A 6). The Ba-oxide have a significant dimension around 20-30 µm, and the presence of oxygen

could be a problem during the production of the wire. Moreover, the SEM analysis reveal the presence of grains of FeAs (Figure A 7). The presence of FeAs as secondary phase is caused by the utilization of that phase during the first step of the synthesis process, and it is balanced in the global analysis of the pellet from the zones rich in Ba-oxide.

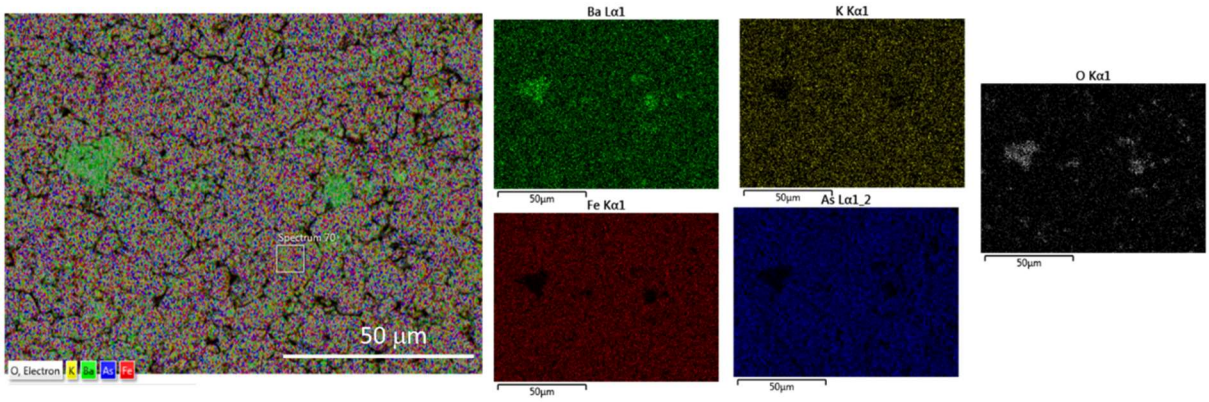

Figure A 6: Elemental mapping performed with SEM on the surface of the pellet. The presence of Ba-oxide is highlighted in green.

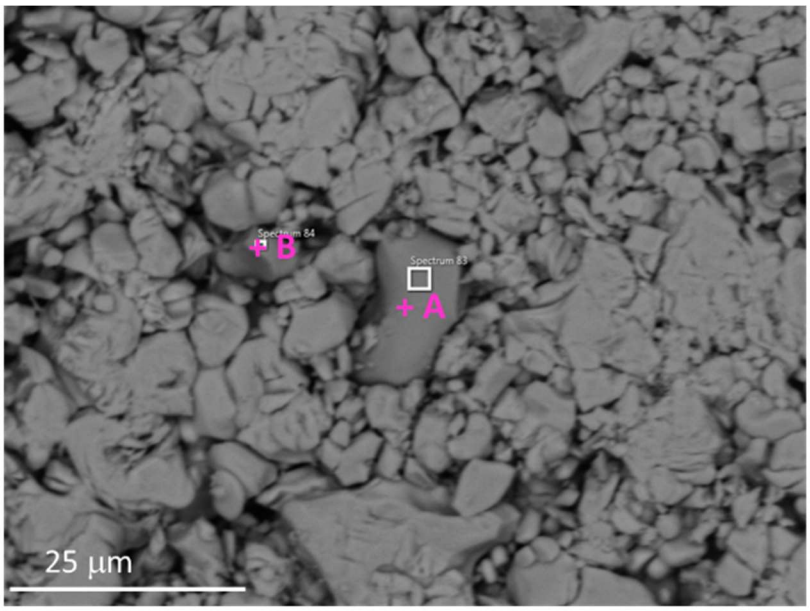

Spectrum	Ba at%	K at%	Fe at%	As at%	Total
A	---	---	50.47	49.53	100.00
B	---	---	50.82	49.18	100.00

Figure A 7: Punctual EDX analysis performed with SEM on the surface of the pellet. Spectra A and B highlight two FeAs grains.

2A.2 Preparation of wires and mechanical deformation

The activity on the production of Ba-122 with the PIT method started at CNR Spin in 2014 within the European project ''SUPERIRON'' [112].

During my thesis the work on Ba-122 PIT wires moving forward in the development of a method to produce wires with a high density of powders at ambient pressure. Based on long lasting experience of the group in producing PIT wires of $Bi_2Sr_2CaCu_2O_{8+x}$ (Bi-2212), and the new in-house synthesized powders, we find a new scalable method to produce Ba-122 wires. The $Ba_{0.5}K_{0.5}Fe_2As_2$ pellets produced as described above were ground in a mortar and then ball milled in order to make them finer and more homogeneous to be packaged in the metal tube. The powders were packed in a silver tube with an inner diameter of 5 mm and an outer diameter of 8 mm. This operation was carried out in a glove box in inert atmosphere to avoid the oxidation of the powders. Finally, the tube was cold worked to obtain the final wire. The first step of the cold working has the aim to produce the best powder packaging and improve the connectivity between grains: for these reasons we use the GDG (grove rolling-drawing-grove rolling) process which was developed for Bi-2212 wires, and which has given very good results.

As shown in Figure A 8 the two techniques are alternated in a suitable way: after the grove-rolling stages compact the powders as much as possible in the transversal direction, the drawing steps make them flow to fill the voids in the longitudinal direction, and so on [113]. In the second part the cold working has the aim of give to the wire the final form, and to induce a texturing of the grains. After the cold working the tapes and the wires were heat treated at 800°C for 30 min and 5h, in 1 bar flowing Ar/H_2 to avoid the oxidation. The heat treatment was performed to sinter the powders and improve the connection between grains. We prepared two couples of samples, wires and tapes: the wires after the GDG process were reduced in section with the drawing down to 1 mm and the tapes after GDG were flat rolled down to 4 mm. After the cold working one tape, and one wires were heat treated for 30 min while the other couples of samples were heat treated for 5h.

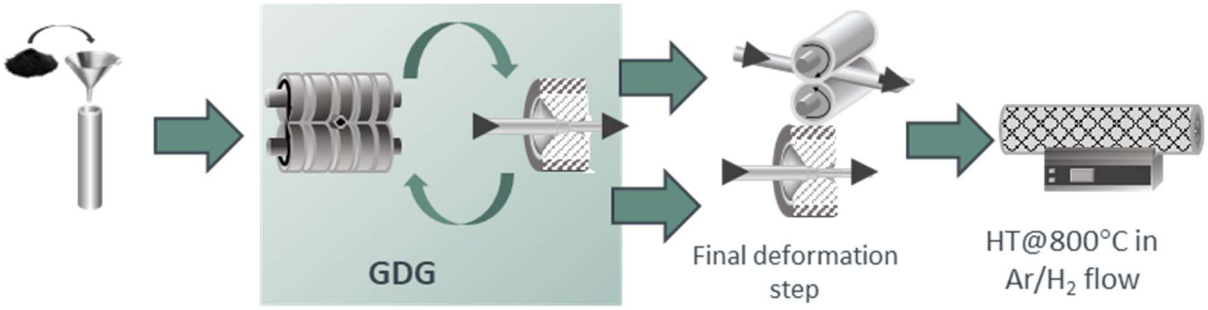

Figure A 8: Schematic illustration of the ex- situ PIT method with the GDG process.

2A.3 SEM characterization of wires and tapes

The transverse sections of the wires were analysed with SEM after the mechanical deformation and the heat treatment.

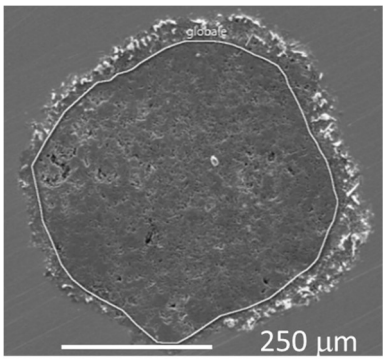

Figure A 9: Cross section of the wire heat treated for 30 min.

In Figure A 9, a picture of the wire heat treated at 800°C for 30 min is shown. As can be seen the wire contained a secondary phase at the interface between the powders and the sheath. The EDX analysis revealed that the brighter phase was K-oxides. Probably the oxygen somehow present in the sheath causes the K oxidation during the heat treatment. Moreover, an elemental mapping of the central part of the same wire (Figure A 10) highlights the presence of the secondary phase FeAs (pink regions) and also the presence of Ba-oxides (green regions). Same results are observed in the tape, which was exposed to the same 30 min heat treatment (Figure A 11:Elemental mapping of the central region of the flat tape heat treated at 800°C for 30 min.).

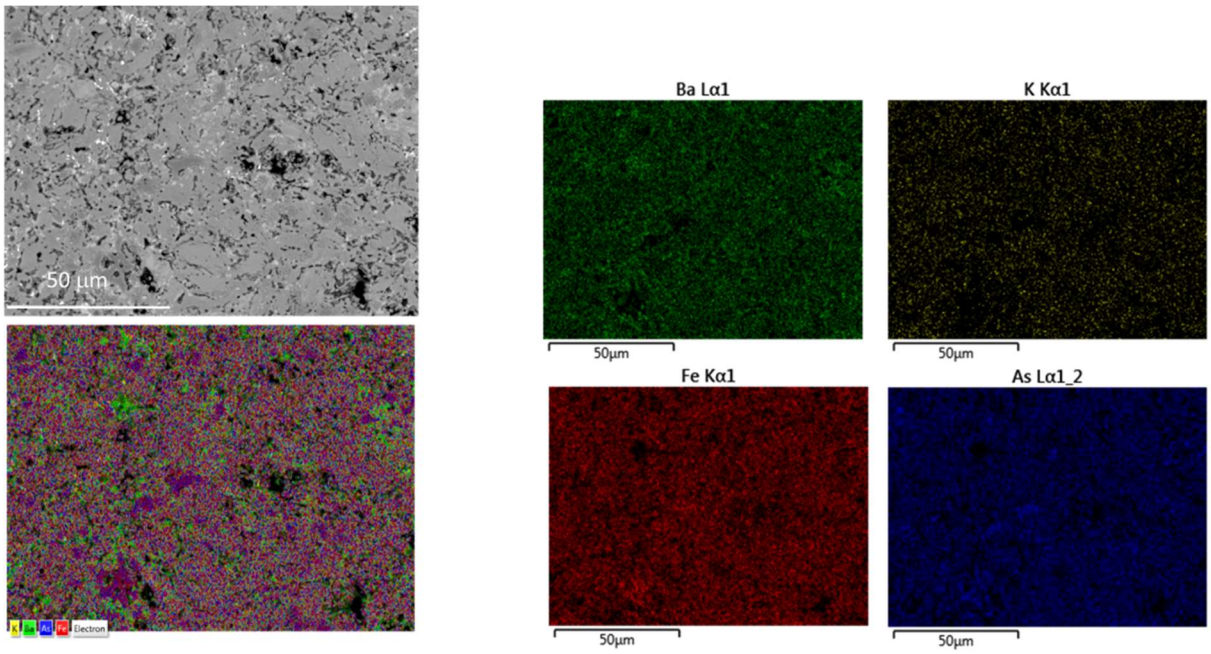

Figure A 10: Elemental mapping of the central region of the round wire heat treated at 800°C for 30 min.

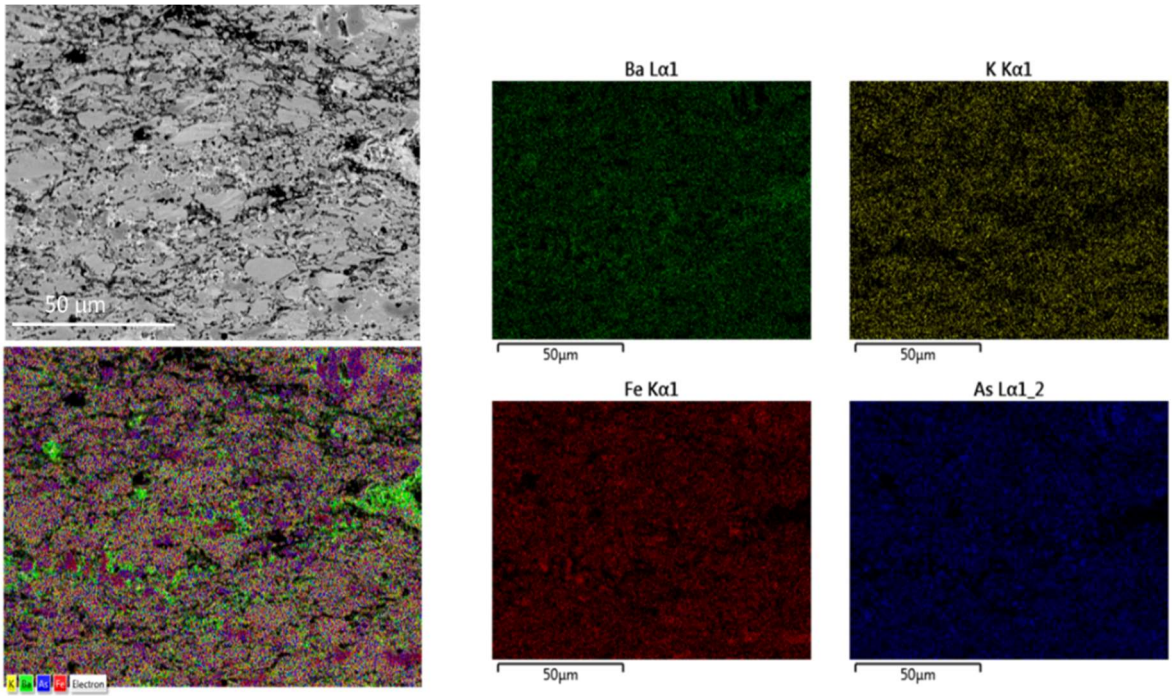

Figure A 11:Elemental mapping of the central region of the flat tape heat treated at 800°C for 30 min.

Further analysis was performed on the samples heat treated for 5h. In this case, both wires and tapes show a more homogenous composition (see elemental mapping in Figure A 12 and Figure A 13) with a smaller amounts of the secondary phase FeAs and without a significant presence of oxides. A largest number of voids seems to be present in this two samples. From these results we can conclude that 5h hours heat treatment is more efficient in homogenized the phase inside the wires. Moreover, the presence of oxides in the samples heat treated for 30 min is explicable considering a strong presence of oxygen in the powders as highlighted in the previous section.

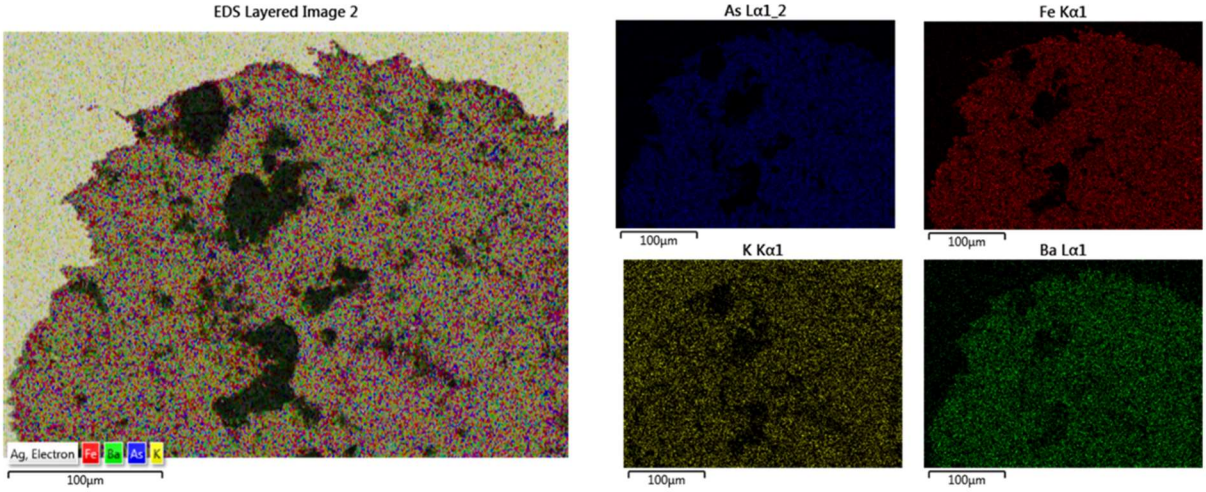

Figure A 12: Elemental mapping of the round wire heat treated at 800°C for 5h.

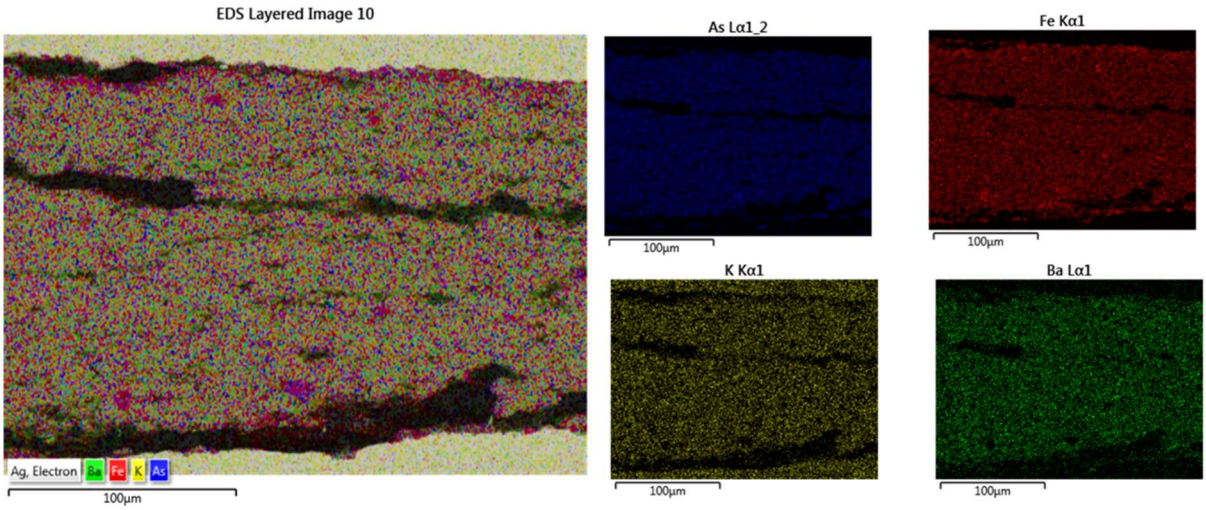

Figure A 13:Elemental mapping of the flat tape heat treated at 800°C for 5h.

2A.4 Transport measurements and texture characterization

In Figure A 14 the resistive transition of the samples and the cross section of samples heat treated for 5 h and 0.5 h are showed. The transitions are better for longer sintering times, with an onset at about 35 K and ΔT_c around 1 K for both wire and tape. The resistivity measurements confirm the SEM analysis, the sample heat treated for 30 min are less homogeneous and it is reflected by the lower T_c and by the presence of different onset in the resistivity curve for the tape.

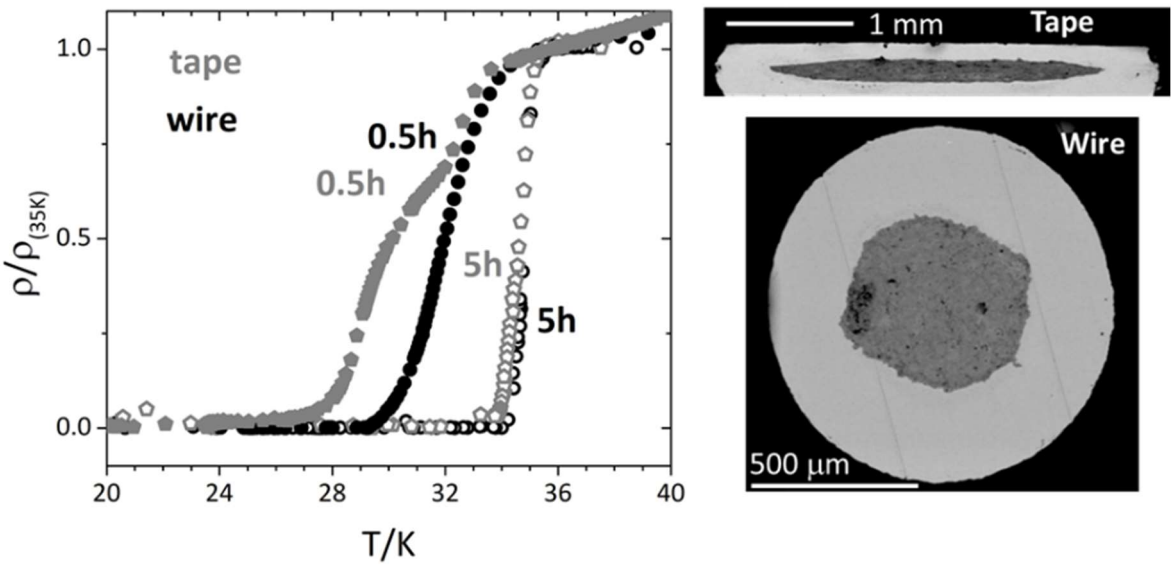

Figure A 14: Resistive transition of wires and tapes heat treated at 800°C for 30 min and 5h and cross sections of the wire and tape heat treated for 5h.

From critical current density measurements performed in DC-four-probe in home-made system in liquid helium bath (4.2K) with a 7 T split coils on 12 cm length sample, emerges that the best results in terms of transport current were obtained with the tape heat treated for 5 h (see Figure A 15 grey empty dot) and the worst results were obtained for the wire heat treated for 30 min which did not show transport current density. Moreover, comparing the wire (black empty dots) and the tapes (grey empty dots) heat treated for 5 h, it is possible to conclude that the flatness induces better results. This could be ascribed to a major compression of the powders inside the tape but also to a possible crystalline orientation of the grains inside the tape.

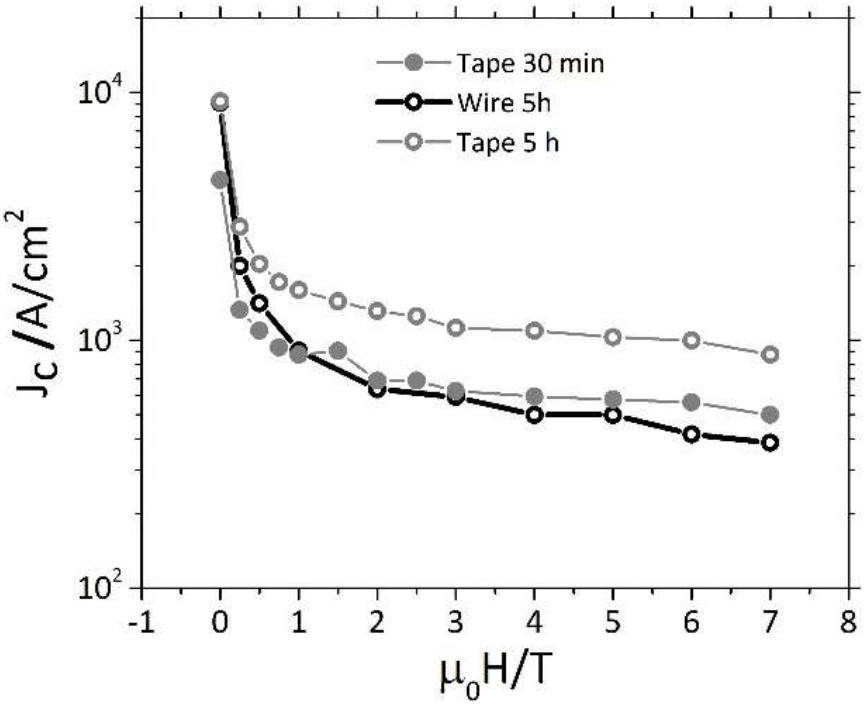

Figure A 15: J_c at 4.2 K of samples heat treated at 800°C for different times. In blue tapes heat treated for 5h (empty symbols) and for 30 min (full dots), in red wires heat treated for 5h.

To confirm the role of the texturing in the performance of the tape we performed XRD texturing measurements. To obtain a orientation factor *f,* proposed by Lotgering[114],the diffraction scan of the powder and the diffraction scan of the tape after peeling one side of the Ag sheath was compared:

$$f = \frac{(\rho - \rho_0)}{(1 - \rho_0)} \quad ; \qquad \rho = \frac{\sum I_{00l}}{\sum I_{hkl}} \rightarrow \text{tape} \; ; \; \rho_0 \rightarrow \text{powders}$$ [114].

The higher the $\boldsymbol{f}$ value, the better the texture of the rolled tapes.

Using the X-ray pattern reported in Figure A 16 $\boldsymbol{f_{\langle 10^\circ - 55^\circ \rangle} = 0.43}$ was obtained, this result confirms that the phase Ba-122 inside the tape shows plate-like grains parallel to the surface and this value is comparable to $\boldsymbol{f}$ reported in literature for the same kind of sample [115,116].

It is well known that the key points to obtain 122 conductors with high J_c values is the misalignment between GB for this reason beside the compaction and the density of the powders also the texturing has to be considered. For the moment the tape reaches higher compaction and has higher texturing than the wire and therefore reaches high J_c values, even if such values need to be improved.

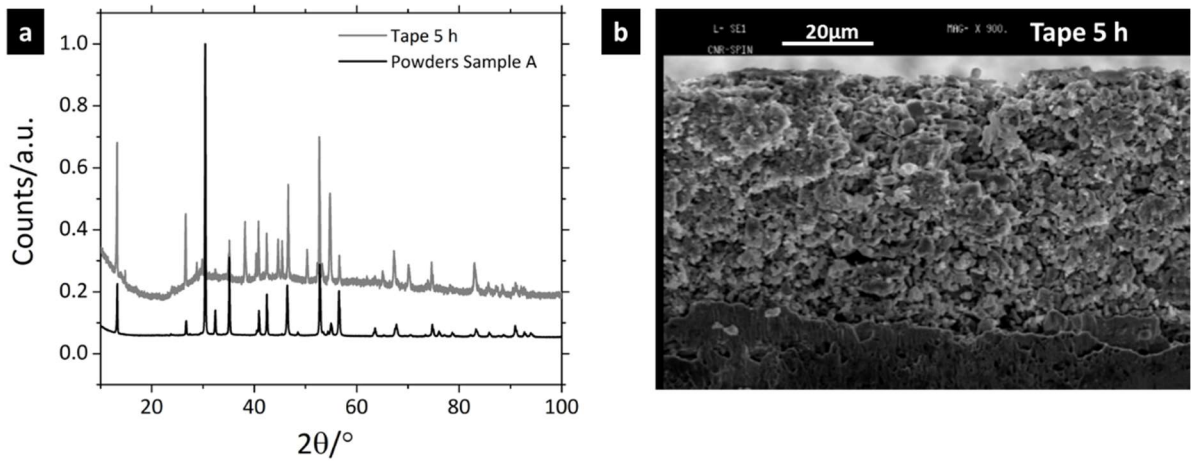

Figure A 16: a) θ-2 θ scan of the powder (sample A) compared with the scan of the tape heat treated for 5 h after a mechanical peeling of the Ag sheath which is shown in SEM images in b).

The results highlight the problem of the weak link GB and validate the necessity to control the orientation of the grains during the process of production of the wire. Based on these results the work was focused only the development of tapes and to obtain better internal compaction of the powders and better texturing we decide to use a strongest mechanical deformation in the final part of the GDG process through flat rolling.

Figure A 17 shows the critical current density of three tapes 0.4mm thick. All the tapes were heat treated for 5h and they differ just for the last part of the mechanical deformation process. The tape with grey empty dots is the one presented in the previous graphs and it was prepared starting from a round wire 1.6 mm thick through flat rolling with a step of reduction of 10% in thickness whereas the tapes in dark grey and black were obtained through flat rolling starting from a round wire of 1.8 mm with step of reduction of 20% in thickness. As can be seen the strongest mechanical deformation have a strong impact on the performance of the wire and this is a good starting point for future attempts. Moreover, the tapes in green in Figure A 17 shows the same J_c performance of the wires produced with the powder from LMU (Munich) in 2014 [100]. These results confirm the possibility to obtain good performance using our in-house synthesized powders and a scalable process which avoid the application of external pressure. These results are very preliminary, further attempts with different metallic sheaths, different deformation process is necessary to better understand the role of texturing and to increment the transport properties of the wires.

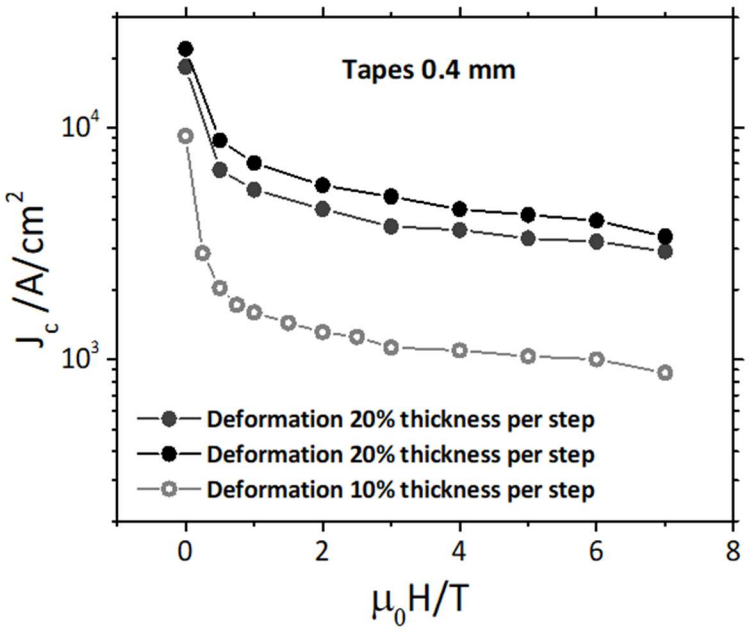

Figure A 17: J_c of tapes 0.4 mm thick heat treated at 800°C for 5 h. The tapes were subjected to different flat rolling deformation process.

3A. CONCLUSIONS OF THE APPENDIX

The Appendix shows the work performed on the development of Ba-122 wires and tapes with the PIT method. The work started with $Ba_{0.5}K_{0.5}Fe_2As_2$ in-house synthesized powders and continued developing Ba-122 wires and tapes using a suitable alternation of the grove rolling and the drawing, in a process called GDG, developed for the Bi-2212 PIT wires. The main purpose of the GDG method is to obtain high compaction of the powders inside the wires and tapes without the application of external pressure. With the experimental work we demonstrate that is possible to obtain a J_c of 2x 10^4 A/cm^2 employing a deformation process which comprises the flat rolling (with a reduction of 20% in section for every step) after GDG. We also found a correlation between the J_c and the texturing of the grain inside the tape, confirming that the tapes have better performance than round wires. These results are promising for future development, and clearly shows the possibility to obtain good quality IBS conductors with PIT method avoiding under pressure heat treatment.

REFERENCES

1. Ballarino, A. *et al.* The CERN FCC Conductor Development Program: A Worldwide Effort for the Future Generation of High-Field Magnets. *IEEE Trans. Appl. Supercond.* **29**, 1–9 (2019).

2. Kamihara, Y., Watanabe, T., Hirano, M. & Hosono, H. Iron-Based Layered Superconductor La[$O_{1-x}F_x$]FeAs (x = 0.05−0.12) with T_c = 26 K. *J. Am. Chem. Soc.* **130**, 3296–3297 (2008).

3. Bellingeri, E. *et al.* T_c=21 K in epitaxial $FeSe_{0.5}Te_{0.5}$ thin films with biaxial compressive strain. *Appl. Phys. Lett.* **96**, 102512 (2010).

4. Braccini, V. *et al.* Highly effective and isotropic pinning in epitaxial Fe(Se,Te) thin films grown on CaF_2 substrates. *Appl. Phys. Lett.* **103**, 172601 (2013).

5. Si, W. *et al.* High current superconductivity in $FeSe_{0.5}Te_{0.5}$-coated conductors at 30 tesla. *Nat. Commun.* **4**, (2013).

6. Sarnelli, E. *et al.* Properties of high-angle Fe(Se,Te) bicrystal grain boundary junctions. *Appl. Phys. Lett.* **104**, 162601 (2014).

7. Sarnelli, E. *et al.* Properties of Fe(Se, Te) Bicrystal Grain Boundary Junctions, SQUIDs, and Nanostrips. *IEEE Trans. Appl. Supercond.* **27**, 1–4 (2017).

8. Hilgenkamp, H. & Mannhart, J. Grain boundaries in high- T c superconductors. *Rev. Mod. Phys.* **74**, 485–549 (2002).

9. Onnes, H. K. The Resistance of Pure Mercury at Helium Temperatures. (1911).

10. Yanwei Ma. Recent progress of iron- -d based wire development for high- field applications. (2019).

11. Bednorz, J. G. & Müller, K. A. Possible high T_c superconductivity in the Ba-La-Cu-O system. *Z. Für Phys. B Condens. Matter* **64**, 189–193 (1986).

12. Wu, M. K. *et al.* Superconductivity at 93 K in a new mixed-phase Y-Ba-Cu-O compound system at ambient pressure. *Phys. Rev. Lett.* **58**, 908–910 (1987).

13. Nagamatsu, J., Nakagawa, N., Muranaka, T., Zenitani, Y. & Akimitsu, J. Superconductivity at 39 K in magnesium diboride. *Nature* **410**, 63–64 (2001).

14. Zhi-An, R. *et al.* Superconductivity at 55 K in Iron-Based F-Doped Layered Quaternary Compound Sm[$O_{1-x}F_x$] FeAs. *Chin. Phys. Lett.* **25**, 2215–2216 (2008).

15. Sakoda, M., Iida, K. & Naito, M. Recent progress in thin-film growth of Fe-based superconductors: superior superconductivity achieved by thin films. *Supercond. Sci. Technol.* **31**, 093001 (2018).

16. Hosono, H., Yamamoto, A., Hiramatsu, H. & Ma, Y. Recent advances in iron-based superconductors toward applications. *Mater. Today* **21**, 278–302 (2018).

17. Gurevich, A. To use or not to use cool superconductors? *Nat. Mater.* **10**, 255–259 (2011).

18. Pallecchi, I. & Putti, M. Iron-based superconductors: Materials Aspect for Applications. in *Applied Superconductivity: Handbook on Devices and Applications*.

19. Putti, M. *et al.* New Fe-based superconductors: properties relevant for applications. *Supercond. Sci. Technol.* **23**, 034003 (2010).

20. Lee, S. *et al.* Weak-link behavior of grain boundaries in superconducting $Ba(Fe_{1-x}Co_x)_2As_2$ bicrystals. *Appl. Phys. Lett.* **95**, 212505 (2009).

21. Katase, T. *et al.* Advantageous grain boundaries in iron pnictide superconductors. *Nat. Commun.* **2**, (2011).

22. Si, W. *et al.* Grain boundary junctions of $FeSe_{0.5}Te_{0.5}$ thin films on $SrTiO_3$ bi-crystal substrates. *Appl. Phys. Lett.* **106**, 032602 (2015).

23. Iida, K., Hänisch, J. & Tarantini, C. Fe-based superconducting thin films on metallic substrates: Growth, characteristics, and relevant properties. *Appl. Phys. Rev.* **5**, 031304 (2018).

24. Kim, K. T. *et al.* Development of cube-textured Ni–W alloy substrates for YBCO-coated conductor. *Phys. C Supercond.* **412–414**, 859–863 (2004).

25. Ijaduola, A. O., Thompson, J. R., Goyal, A., Thieme, C. L. H. & Marken, K. Magnetism and ferromagnetic loss in Ni–W textured substrates for coated conductors. *Phys. C Supercond.* **403**, 163–171 (2004).

26. Iida, K. *et al.* Epitaxial Growth of Superconducting $Ba(Fe_{1-x}Co_x)_2As_2$ Thin Films on Technical Ion Beam Assisted Deposition MgO Substrates. *Appl. Phys. Express* **4**, 013103 (2011).

27. Trommler, S. *et al.* Architecture, microstructure and J_c anisotropy of highly oriented biaxially textured Co-doped $BaFe_2As_2$ on Fe/IBAD-MgO-buffered metal tapes. *Supercond. Sci. Technol.* **25**, 084019 (2012).

28. Katase, T. *et al.* Biaxially textured cobalt-doped $BaFe_2As_2$ films with high critical current density over 1 MA/cm^2 on MgO-buffered metal-tape flexible substrates. *Appl. Phys. Lett.* **98**, 242510 (2011).

29. Xu, Z., Yuan, P., Fan, F., Chen, Y. & Ma, Y. Transport properties and pinning analysis for Co-doped $BaFe_2As_2$ thin films on metal tapes. *Supercond. Sci. Technol.* **31**, 055001 (2018).

30. Iida, K. *et al.* Highly textured oxypnictide superconducting thin films on metal substrates. *Appl. Phys. Lett.* **105**, 172602 (2014).

31. Si, W. *et al.* Iron-chalcogenide $FeSe_{0.5}Te_{0.5}$ coated superconducting tapes for high field applications. *Appl. Phys. Lett.* **98**, 262509 (2011).

32. Sato, H., Hiramatsu, H., Kamiya, T. & Hosono, H. Enhanced critical-current in P-doped $BaFe_2As_2$ thin films on metal substrates arising from poorly aligned grain boundaries. *Sci. Rep.* **6**, (2016).

33. Xu, Z., Yuan, P., Ma, Y. & Cai, C. High-performance $FeSe_{0.5}Te_{0.5}$ thin films fabricated on less-well-textured flexible coated conductor templates. *Supercond. Sci. Technol.* **30**, 035003 (2017).

34. Huang, J. *et al.* A simplified superconducting coated conductor design with Fe-based superconductors on glass and flexible metallic substrates. *J. Alloys Compd.* **647**, 380–385 (2015).

35. Huang, J. *et al.* Superconducting Iron Chalcogenide Thin Films Integrated on Flexible Mica Substrates. *IEEE Trans. Appl. Supercond.* **29**, 1–4 (2019).

36. Bellingeri, E. *et al.* Tuning of the superconducting properties of $FeSe_{0.5}Te_{0.5}$ thin films through the substrate effect. *Supercond. Sci. Technol.* **25**, 084022 (2012).

37. Bellingeri, E. *et al.* High field vortex phase diagram of Fe(Se, Te) thin films. *Supercond. Sci. Technol.* **27**, 044007 (2014).

38. Perasso, A. *et al.* An automatic method for atom identification in scanning tunnelling microscopy images of Fe-chalcogenide superconductors *J. Microsc.* **260**, 302–311 (2015).

39. Palenzona, A. *et al.* A new approach for improving global critical current density in $Fe(Se_{0.5}Te_{0.5})$ polycrystalline materials. *Supercond. Sci. Technol.* **25**, 115018 (2012).

40. Molatta, S. *et al.* Interface control by homoepitaxial growth in pulsed laser deposited iron chalcogenide thin films. *Sci. Rep.* **5**, (2015).

41. The international Nickel company. 36% Nickel Iron alloy for Low Temperature Service.

42. Glowacki, B. A. *et al.* Texture development in long lengths of NiFe tapes for superconducting coated conductor. *J. Mater. Sci.* **37**, 157–168 (2002).

43. Palombo, M. *et al.* Exploring the feasibility of Fe(Se,Te) conductors by *ex-situ* powder-in-tube method. *J. Appl. Phys.* **117**, 213903 (2015).

44. Iida, K. *et al.* Generic Fe buffer layers for Fe-based superconductors: Epitaxial $FeSe_{1-x}Te_x$ thin films. *Appl. Phys. Lett.* **99**, 202503 (2011).

45. Lu, J., Choi, E. S. & Zhou, H. D. Physical properties of Hastelloy® C-276™ at cryogenic temperatures. *J. Appl. Phys.* **103**, 064908 (2008).

46. Mehta, K. K., Mukhopadhyay, P., Mandal, R. K. & Singh, A. K. Mechanical Properties Anisotropy of Cold-Rolled and Solution-Annealed Ni-Based Hastelloy C-276 Alloy. *Metall. Mater. Trans. A* **45**, 3493–3504 (2014).

47. Hashim, A. A., Hammood, A. S. & Hammadi, N. J. Evaluation of High-Temperature Oxidation Behavior of Inconel 600 and Hastelloy C-22. *Arab. J. Sci. Eng.* **40**, 2739–2746 (2015).

48. Sylva G, Malagoli A, Bellingeri E, Putti M, Ferdeghini C, Vannozzi A, Celentano G, Hopkins S.C, Lunt A.J.G, Ballarino A, and Braccini V. Analysis of Fe(Se,Te) Films Deposited on Unbuffered Invar 36.

49. http://www.evico.de/.

50. Sylva, G. *et al.* Fe(Se,Te) coated conductors deposited on simple rolling-assisted biaxially textured substrate templates. *Supercond. Sci. Technol.* **32**, 084006 (2019).

51. Budai, J. D. *et al.* X-ray microdiffraction study of growth modes and crystallographic tilts in oxide films on metal substrates. *Nat. Mater.* **2**, 487–492 (2003).

52. Feldmann, D. M. *et al.* Grain orientations and grain boundary networks of $YBa_2Cu_3O_{7-\delta}$ films deposited by metalorganic and pulsed laser deposition on biaxially textured Ni–W substrates. *J. Mater. Res.* **21**, 923–934 (2006).

53. Celentano, G. *et al.* YBCO films and CeO_2/YSZ/CeO_2 buffer layers grown on Ni-Cr-W RABiTS with a Pd seed layer. *IEEE Trans. Appiled Supercond.* **15**, 2691–2694 (2005).

54. Li, Q., Si, W. & Dimitrov, I. K. Films of iron chalcogenide superconductors. *Rep. Prog. Phys.* **74**, 124510 (2011).

55. Mele, P. Superconducting properties of iron chalcogenide thin films. *Sci. Technol. Adv. Mater.* **13**, 054301 (2012).

56. Vaglio, R., Attanasio, C., Maritato, L. & Ruosi, A. Explanation of the resistance-peak anomaly in nonhomogeneous superconductors. *Phys. Rev. B* **47**, 15302–15303 (1993).

57. Tarantini, C. *et al.* Significant enhancement of upper critical fields by doping and strain in iron-based superconductors. *Phys. Rev. B* **84**, (2011).

58. Simone Prili. Deposizione per via chimica di film di La $_2Zr_2O_2$ e CeO_2 drogato con Zr come buffer layer orientati per la crescita epitassiale di film superconduttori a base di ferro. (Università degli studi di Roma Tor Vergata, 2019).

59. Cerruti F, Lechner A, Mereghetti A & Brugger A. Particle fluence on LHC magnets.

60. Lechner A *et al.* Proc. Workshop Radiation Effects, Supercond. Magnets Mater. Poland 2014.

61. Flükiger R. Impact of the Number of dpa on the Superconducting Properties in HiLumi LHC and FCC Accelerators. (2017).

62. Ferrari A, Sala P, Fasso A & Ranft J. *FLUKA: A multiparticle transport code, CERN-2005-010, 2005*.

63. Spina, T. *et al.* Correlation Between the Number of Displacements Per Atom and After High-Energy Irradiations of Nb_3Sn Wires for the HL-LHC. *IEEE Trans. Appl. Supercond.* **26**, 1–5 (2016).

64. Spina, T. *et al.* Variation of the Critical Properties of Alloyed Nb-Sn Wires After Proton Irradiation at 65 MeV and 24 GeV. *IEEE Trans. Appl. Supercond.* **25**, 1–5 (2015).

65. Baumgartner, T. *et al.* Effects of neutron irradiation on pinning force scaling in state-of-the-art Nb_3Sn wires. *Supercond. Sci. Technol.* **27**, 015005 (2014).

66. Flükiger, R. *et al.* Variation of T_c, lattice parameter and atomic ordering in Nb_3Sn platelets irradiated with 12 MeV protons: correlation with the number of induced Frenkel defects. *Supercond. Sci. Technol.* **30**, 054003 (2017).

67. Eisterer, M. Radiation effects on iron-based superconductors. *Supercond. Sci. Technol.* **31**, 013001 (2018).

68. Tarantini, C. *et al.* Effect of α -particle irradiation on a NdFeAs(O,F) thin film. *Supercond. Sci. Technol.* **31**, 034002 (2018).

69. Daghero, D. *et al.* Effect of ion irradiation on surface morphology and superconductivity of $BaFe_2(As_{1-x}P_x)_2$ films. *Appl. Surf. Sci.* **395**, 9–15 (2017).

70. Maiorov, B. *et al.* Competition and cooperation of pinning by extrinsic point-like defects and intrinsic strong columnar defects in $BaFe_2As_2$ thin films. *Phys. Rev. B* **86**, (2012).

71. Schilling, M. B. *et al.* Tracing the s ± symmetry in iron pnictides by controlled disorder. *Phys. Rev. B* **93**, (2016).

72. Eisterer, M. *et al.* Anisotropic critical currents in $FeSe_{0.5}Te_{0.5}$ films and the influence of neutron irradiation. *Supercond. Sci. Technol.* **24**, 065016 (2011).

73. Ozaki, T. *et al.* A route for a strong increase of critical current in nanostrained iron-based superconductors. *Nat. Commun.* **7**, 13036 (2016).

74. Ozaki, T. *et al.* Enhanced critical current in superconducting $FeSe_{0.5}Te_{0.5}$ films at all magnetic field orientations by scalable gold ion irradiation. *Supercond. Sci. Technol.* **31**, 024002 (2018).

75. Ahmad, D. *et al.* Effect of proton irradiation on the fluctuation-induced magnetoconductivity of $FeSe_{1-x}Te_x$ thin films. *New J. Phys.* **19**, 093004 (2017).

76. Langford, J. I., Louër, D., Sonneveld, E. J. & Visser, J. W. Applications of Total Pattern Fitting to a Study of Crystallite Size and Strain in Zinc Oxide Powder. *Powder Diffr.* **1**, 211–221 (1986).

77. Ziegler, J. F., Ziegler, M. D. & Biersack, J. P. SRIM – The stopping and range of ions in matter *Nucl. Instrum. Methods Phys. Res. Sect. B Beam Interact. Mater. At.* **268**, 1818–1823 (2010).

78. Haberkorn, N. *et al.* Influence of random point defects introduced by proton irradiation on critical current density and vortex dynamics of $Ba(Fe_{0.925}Co_{0.075})_2As_2$ single crystals. *Phys. Rev. B* **85**, (2012).

79. Stoller, R. E. *et al.* On the use of SRIM for computing radiation damage exposure. *Nucl. Instrum. Methods Phys. Res. Sect. B Beam Interact. Mater. At.* **310**, 75–80 (2013).

80. Norgett, M. J., Robinson, M. T. & Torrens, I. M. A proposed method of calculating displacement dose rates. *Nucl. Eng. Des.* **33**, 50–54 (1975).

81. Nakajima, Y. *et al.* Suppression of the critical temperature of superconducting $Ba(Fe_{1-x}Co_x)_2As_2$ by point defects from proton irradiation. *Phys Rev B* **82**, 220504 (2010).

82. Taen, T. *et al.* Pair-breaking effects induced by 3-MeV proton irradiation in (Ba, K) Fe_2As_2. *Phys Rev B* **88**, 224514 (2013).

83. Gozzelino, L. *et al.* Temperature dependence of the critical current density in proton irradiated YBCO films by magneto-optical analysis. *Eur. Phys. J. B* **40**, 3–9 (2004).

84. Leo, A. *et al.* Anisotropic Effect of Proton Irradiation on Pinning Properties of Fe(Se,Te) Thin Films. *IEEE Trans. Appl. Supercond.* **29**, 1–5 (2019).

85. Leo, A. *et al.* Critical current anisotropy in Fe(Se,Te) film irradiated by high-energy protons. *To be published* (2019).

86. Sylva, G. *et al.* Effects of high-energy proton irradiation on the superconducting properties of Fe(Se,Te) thin films. *Supercond. Sci. Technol.* **31**, 054001 (2018).

87. Gao, Z. *et al.* Preparation of $LaFeAsO_{0.9}F_{0.1}$ wires by the powder-in-tube method. *Supercond. Sci. Technol.* **21**, 105024 (2008).

88. Gao, Z. *et al.* Superconducting properties of $SmO_{1-x}F_xFeAs$ wires with T_c = 52 K prepared by the powder-in-tube method. *Supercond. Sci. Technol.* **21**, 112001 (2008).

89. Qi, Y. *et al.* Superconductivity of powder-in-tube $Sr_{0.6}K_{0.4}Fe_2As_2$ wires. *Phys. C Supercond.* **469**, 717–720 (2009).

90. Mizuguchi, Y. *et al.* Fabrication of the Iron-Based Superconducting Wire Using Fe(Se,Te). *Appl. Phys. Express* **2**, 083004 (2009).

91. Fujioka, M. *et al.* Effective *Ex-situ* Fabrication of F-Doped SmFeAsO Wire for High Transport Critical Current Density. *Appl. Phys. Express* **4**, 063102 (2011).

92. Qi, Y. *et al.* Transport critical currents in the iron pnictide superconducting wires prepared by the *ex situ* PIT method. *Supercond. Sci. Technol.* **23**, 055009 (2010).

93. Ma, Y. *et al.* Fabrication and characterization of iron pnictide wires and bulk materials through the powder-in-tube method. *Phys. C Supercond.* **469**, 651–656 (2009).

94. Wang, L. *et al.* Large transport critical currents of powder-in-tube $Sr_{0.6}K_{0.4}Fe_2As_2$/Ag superconducting wires and tapes. *Phys. C Supercond.* **470**, 183–186 (2010).

95. Weiss, J. D. *et al.* High intergrain critical current density in fine-grain $(Ba_{0.6}K_{0.4})Fe_2As_2$ wires and bulks. *Nat. Mater.* **11**, 682 (2012).

96. Pyon, S. *et al.* Improvements of fabrication processes and enhancement of critical current densities in (Ba,K)Fe $_2$ As $_2$ HIP wires and tapes. *Supercond. Sci. Technol.* **31**, 055016 (2018).

97. Liu, S. *et al.* Transport current density at temperatures up to 25 K of Cu/Ag composite sheathed 122-type tapes and wires. *Supercond. Sci. Technol.* **30**, 115007 (2017).

98. Gao, Z. *et al.* High transport J_c in stainless steel/Ag-Sn double sheathed Ba122 tapes. *Supercond. Sci. Technol.* **30**, 095012 (2017).

99. Gao, Z., Togano, K., Matsumoto, A. & Kumakura, H. High transport J_c in magnetic fields up to 28 T of stainless steel/Ag double sheathed Ba122 tapes fabricated by scalable rolling process. *Supercond. Sci. Technol.* **28**, 012001 (2015).

100. Malagoli, A. *et al.* Role of heat and mechanical treatments in the fabrication of superconducting Ba $_{0.6}$ K $_{0.4}$ Fe $_2$ As $_2$ *ex situ* powder-in-tube tapes. *Supercond. Sci. Technol.* **28**, 095015 (2015).

101. Ma, Y. Development of high-performance iron-based superconducting wires and tapes. *Phys. C Supercond. Its Appl.* **516**, 17–26 (2015).

102. Lin, H. *et al.* Large transport Jc in Cu-sheathed $Sr_{0.6}K_{0.4}Fe_2As_2$ superconducting tape conductors. *Sci. Rep.* **5**, 11506 (2015).

103. Mizuguchi, Y., Izawa, H., Ozaki, T., Takano, Y. & Miura, O. Transport properties of single- and three-core FeSe wires fabricated by a novel chemical-transformation PIT process. *Supercond. Sci. Technol.* **24**, 125003 (2011).

104. Lin, H. *et al.* Hot pressing to enhance the transport Jc of $Sr_{0.6}K_{0.4}Fe_2As_2$ superconducting tapes. *Sci. Rep.* **4**, 6944 (2014).

105. Huang, H. *et al.* High transport current superconductivity in powder-in-tube $Ba_{0.6}K_{0.4}Fe_2As_2$ tapes at 27 T. *Supercond. Sci. Technol.* **31**, 015017 (2018).

106. Zhang, X. *et al.* Realization of practical level current densities in $Sr_{0.6}K_{0.4}Fe_2As_2$ tape conductors for high-field applications. *Appl. Phys. Lett.* **104**, 202601 (2014).

107. Yao, C. & Ma, Y. Recent breakthrough development in iron-based superconducting wires for practical applications. *Supercond. Sci. Technol.* **32**, 023002 (2019).

108. Huang, H. *et al.* Effects of rolling deformation processes on the properties of Ag-sheathed $Sr_{1-x}K_xFe_2As_2$ superconducting tapes. *Phys. C Supercond. Its Appl.* **525–526**, 94–99 (2016).

109. Yao, C. *et al.* Critical current density and microstructure of iron sheathed multifilamentary $Sr_{1-x}K_xFe_2As_2$/Ag composite conductors. *J. Appl. Phys.* **118**, 203909 (2015).

110. Yao, C. *et al.* Transport critical current density of high-strength $Sr_{1-x}K_xFe_2As_2$ /Ag/Monel composite conductors. *Supercond. Sci. Technol.* **30**, 075010 (2017).

111. Zhang, X. *et al.* Superconducting Properties of 100-m Class $Sr_{0.6}K_{0.4}Fe_2As_2$ Tape and Pancake Coils. *IEEE Trans. Appl. Supercond.* **27**, 1–5 (2017).

112. Malagoli, A. *et al.* Role of heat and mechanical treatments in the fabrication of superconducting $Ba_{0.6}K_{0.4}Fe_2As_2$ *ex situ* powder-in-tube tapes. *Supercond. Sci. Technol.* **28**, 095015 (2015).

113. Leveratto, A., Braccini, V., Contarino, D., Ferdeghini, C. & Malagoli, A. New concept for the development of Bi-2212 wires for high-field applications. *Supercond. Sci. Technol.* **29**, 045005 (2016).

114. Lotgering, F. K. Topotactical reactions with ferrimagnetic oxides having hexagonal crystal structures—I. *J. Inorg. Nucl. Chem.* **9**, 113–123 (1959).

115. Huang, H. *et al.* Effects of heat treatment temperature on the superconducting properties of $Ba_{1-x}K_x Fe_2 As_2$ tapes. *Supercond. Sci. Technol.* **32**, 025007 (2019).

116. Cheng, Z. *et al.* Effect of Wire Diameter on the Microstructure and J_c Properties of $Ba_{0.6} K_{0.4} Fe_2 As_2$ Tapes. *IEEE Trans. Appl. Supercond.* **28**, 1–5 (2018).